Structure and function of the photoreceptor protein and photosynthetic reaction center investigated by electron paramagnetic resonance

EPR 法を用いた光受容タンパク質および光合成反応中心の構造と機能の解析

Doctoral dissertation

Toru Kondo

May 2011

Division of Material Science (Physics), Graduate School of Science

Nagoya University

Contents

General introduction

Inexhaustible energy of sunlight is converted into chemical energy by photosynthesis, which is essential for all of the organisms on the earth. Photosynthetic organisms utilize the solar energy efficiently, and grow all over the world and make huge influences on the global environment. Electron transfer is the most important reaction to drive the photosynthetic system. Electron paramagnetic resonance (EPR) spectroscopy is able to trace the electron reaction and analyze the reaction kinetics. It is also possible to analyze the electronic structure of the electron carrier or the protein structure. In this thesis, I studied three systems relevant to photosynthesis: the first is a phototactic system for adaptation to photoenvironment (Chapter I), the second is a biosynthesis system of chlorophyll molecule that is essential for the photoreaction in photosynthetic organisms (Chapter II), and the third is an energy conversion system of light energy into electrochemical energy in photosynthetic protein complex (Chapter III). The contents of each Chapter in this chapter are summarized below.

Chapter I: Phototactic reaction regulated by a blue light sensory photoreceptor protein PixD

Sunlight is indispensable for photosynthesis, while excess light is harmful to a living system. Therefore, photosynthetic organisms have evolved a response capability to the environment light for environmental adaptation, and growth control. It is important not only to sense the light intensity, but also to distinguish the quality of light (wavelength) for adaptation to environmental light conditions. Cyanobacteria have various photoreceptors for different color, such as the blue, green, red, and far-red light photoreceptors. A sensor of blue light using flavin (BLUF) domain is a newly discovered blue light sensory photoreceptor protein. In this chapter, I studied PixD, one of BLUF proteins, regulating pili-dependent cell motility in response to blue light.

PixD contains a flavin pigment, flavin adenine dinucleotide (FAD), as a chromophore. The blue light excitation of FAD induces charge separation reaction and produces a radical pair between FAD and adjacent amino acid residue. The photo-induced radical pair formation seems to be essential to trigger the conformational changes of the protein complex, which eventually leads to the signal transduction process through a cascade of information exchanges carried by other protein and enzyme systems to regulate the cellular movement of anoxygenic photosynthetic bacteria and cyanobacteria. I determined quantitatively the exchange interaction J inside the photo-induced radical pair by analyzing the temperature dependence of spin-lattice relaxation rate by pulsed EPR spectroscopy. The quantity of J was ferromagnetic and much larger than ever before in a biological system. The spin property indicated the formation of complete triplet spin state, and seems to affect stability of the radical pair. I also observed the long-range magnetic dipole interaction between the

radical pairs in a PixD olygomer by pulsed electron-electron double resonance (PELDOR) method, and resolved the complex structure of the water-soluble sensory protein PixD.

Chapter II: Biosynthesis of chlorophyllide *a, precursor molecule of chlorophyll and bacteriochlorophyll, in DPOR enzymatic system*

Chlorophyll (Chl) and Bacteriochlorophyll (Bchl) molecules have key roles as a light absorber and an energy/electron mediator in photosynthetic reaction. The spectroscopic and physicochemical properties of the pigments changed according to the function of the photosynthetic reaction center (RC) and native habitat. Bchl, used mainly in anoxygenic photosynthesis, is replaced by Chl in oxygenic photosynthesis. Chl generally exhibits absorption peak at shorter wavelength than that of Bchl, and the higher light energy is used in the oxidation of a water molecule (i.e. oxygen evolution reaction). Thus, the difference of major pigment characterizes anoxygenic and oxygenic photosynthesis. However, both Bchl and Chl are synthesized from the same precursor chlorophyllide *a* (Chlide) through diverse enzymatic reactions. Chlide is also synthesized from protochlorophyllide (Pchlide), in which two different enzymes operate independently for reduction of Pchlide; the one is light-dependent Pchlide oxidoreductase (LPOR) which utilizes light energy to promote the reduction, and the other is light-independent (dark-operative) Pchlide oxidoreductase (DPOR) which catalyzes Pchlide reduction irrespective of light. DPOR exhibits no sequence similarity to LPOR, and rather homology with the nitrogenase catalyzing the reduction of N_2 to NH_3. The molecular mechanism of the enzymatic reaction without light energy in DPOR remains to be clarified. In this chapter, I studied the enzymatic reduction system of DPOR by EPR spectroscopy.

In the DPOR system, Chlide is synthesized by the double-reduction/protonation of Pchlide substrate that is linked to an enzyme protein complex (NB-protein). Single electron, provided by another protein complex (L-protein) that works as an electron mediator, is transferred to a 4Fe-4S type iron sulfur cluster in NB-protein (NB-cluster) and subsequently employed to the reduction reaction. The NB-cluster has a special and unique ligand by aspartic acid (Asp) residue in addition to three cysteine (Cys) lignads, in contrast to four Cys ligands of the conventional 4Fe-4S cluster. An EPR signal of the native NB-cluster indicated the high spin state of $S = 3/2$. On the other hand, a mutant NB-protein, in which the Asp ligand was replaced by a Cys ligand, exhibited an $S = 1/2$ EPR signal of NB-cluster and lost its catalytic activity. The results suggest that the unique Asp ligand contributes to the electronic structure of the cluster and produces the low redox potential necessary for the reduction of Pchlide.

Chapter III: Electron transfer reaction in photosynthetic reaction center complex

In the oxygenic photosynthesis, two photosynthetic proteins, called photosystem II (PS II) and I (PS I), have different crucial roles: PS II RC produces the high redox potential enough to dissolve a water molecule, and PS I RC produces the low redox potential to reduce a $NADP^+$. The PS II and PS I RCs operate in series and generate the light-driven electron transfer. The efficient system is achieved in the course of evolution. Phylogenetic tree based on the 16S rRNA sequence suggests that the primitive photosynthetic system had evolved in eubacteria and then diverged into type I and type II RCs (Fig.G1). Anoxygenic heliobacteria and green sulfur bacteria contain type I RCs (hRC and gRC, respectively) like PS I RC, and the hRC (and gRC) seem to be the ancestral form of photosynthetic RC. The protein structure of the hRC and gRC and their electron transfer mechanism have been unclear. In particular, electron mediators F_X (iron sulfur cluster) and A_1 (quinone molecule), which are known in PS I RC, remain to be identified in the hRC and gRC. In this chapter, I identified F_X and A_1 in the oldest type of photosynthetic RC complex of heliobacteria. and discussed the electron transfer mechanism.

I detected angular dependent EPR spectrum of iron sulfur clusters in the orientated membrane of heliobacteria, and determined orientations of the g-tensors of iron sulfur clusters in hRC. A light-induced $S = 1/2$ EPR signal was assigned to F_X because of similarity of the orientation to that of F_X in PS I. The structure of F_X was more symmetrical than that in PS I, seems to reflect the specific high-symmetric structure of hRC. The ultra-fast photo-induced charge separation reaction and sequential multistep electron transfer processes in RC produce a radical pair in a unique spin state, called electron spin polarization (ESP) state. I detected transiently photo-induced radical pairs in hRC by time-resolved EPR spectroscopy. The electron transfer rate in hRC was obviously different from that in PS I. The analysis of ESP spectral patterns indicated that the molecular plane of A_1 tilts compared to that in PS I. I discussed the electron transfer mechanism in hRC.

Method

Method I; electron paramagnetic resonance (EPR), used in chapter I, II, and III.

Energy levels of unpaired electron spin split in the external magnetic field, called Zeeman splitting. The resonance condition for EPR is given as the following equation:

$$\Delta E = g\mu_e H_0 = h\nu \quad , \tag{1}$$

where g is the g-factor, μ_e is the Bohr magneton, H_0 is the static magnetic field, h is the Planck constant, and the ν is the microwave frequency. The EPR has been employed to study on the electron reaction in biological systems, in which organic molecule, metal cluster, and/or metal complex serve as the electron mediator. The EPR signal provides much information on spin properties such as g-factor, fine structure mainly due to the electron-electron interaction and ligand field, and hyperfine structure mainly due to the electron-nuclear interaction and nuclear quadrupole interaction. The spin Hamiltonian was expressed as the following equation:

$$\mathcal{H} = \mu_e \boldsymbol{H} \cdot \boldsymbol{g}_e \cdot \boldsymbol{S} + \mu_n \boldsymbol{H} \cdot \boldsymbol{g}_n \cdot \boldsymbol{I} + \boldsymbol{S} \cdot \boldsymbol{D} \cdot \boldsymbol{S} + \boldsymbol{S} \cdot \boldsymbol{A} \cdot \boldsymbol{I} + \boldsymbol{I} \cdot \boldsymbol{Q} \cdot \boldsymbol{I} \quad , \tag{2}$$

where μ_n is the nuclear magneton, $\boldsymbol{H}$ is the external magnetic field vector, $\boldsymbol{g_e}$ and $\boldsymbol{g_n}$ are g-tensors for electron and nuclear, respectively, $\boldsymbol{S}$ and $\boldsymbol{I}$ are spin operators for electron and nuclear, respectively, $\boldsymbol{D}$ is the fine-structure tensor, $\boldsymbol{A}$ is the hyperfine tensor, and $\boldsymbol{Q}$ is the nuclear quadrupole interaction tensor. The g-tensor reflects the molecular structure. An EPR spectral shape changes significantly according to the symmetry of the g-tensor (Fig.G2). Conventional contentious-wave (CW) EPR spectrum is usually detected with the field modulation as a first-derivative signal.

Method II; Pulsed electron-electron double resonance (PELDOR), used in chapter I.

Magnetic substance embedded in biological systems interacts magnetically with some electron/nuclear spins in protein. The magnetic interaction gives insights into protein environment around the magnetic substance and protein structure in solution. However, the magnetic interaction is too weak to be detected by conventional contentious-wave (CW) EPR, i.e. the peak splitting due to the interaction is buried in the spectral line width caused by the magnetic inhomogeneity. In order to extract information of the weak interaction from the inhomogeneity, pulse EPR spectroscopy has been developed. A standard Hahn echo occurs after 90^o and 180^o microwave pulses with interval time τ (Fig.G3). The time evolution of the spin system during successive steps can be described with the density matrix formalism. The unitary operates for the time evolution during nutation induced by a

microwave pulse and free precession without microwave pulse (defined as $\boldsymbol{R_{tp}}$ and $\boldsymbol{R_{tn}}$, respectively) are expressed by the following equations:

$$R_{tp} = \exp\left[-i\mathscr{H}_p t_p/\hbar\right] , \tag{3}$$

$$R_{tn} = \exp\left[-i\mathscr{H}_n t_n/\hbar\right] , \tag{4}$$

where $\mathscr{H}_p$ and $\mathscr{H}_n$ are the spin Hamiltonians during and without the microwave pulse, respectively, t_p is the pulse duration, t_n is the time without the microwave pulse, and $\hbar$ is the planck constant. The pulse durations inducing 90° and 180° spin flip-flop are defined as t_{90} and t_{180}, respectively. The density operator σ at the time of $t_{90}+\tau+t_{180}+t$ is expressed by the following equation:

$$\sigma(t_{90}+\tau+t_{180}+t) = R_{t_{90}+\tau+t_{180}+t}\cdot\sigma_0\cdot R^*_{t_{90}+\tau+t_{180}+t} , \tag{5}$$

$$\text{where,}\quad R_{t_{90}+\tau+t_{180}+t} = R_t\cdot R_{t_{180}}\cdot R_\tau\cdot R_{t_{90}} . \tag{6}$$

where σ_0 is a density operator in the initial spin state. Based on the high magnetic field approximation and the rotating wave approximation, when the external magnetic field is parallel to z-axis and the oscillating field of microwave pulse to x-axis, the density operator σ is described as below:

$$\sigma(t_{90}+\tau+t_{180}+t) = \cos(\Delta\omega\tau)S_z - \sin(\Delta\omega\tau)\cos(\Delta\omega t)S_x - \sin(\Delta\omega\tau)\cos(\Delta\omega t)S_y , \tag{7}$$

where $\Delta\omega$ is a shift of the spin precession frequency from the Zeeman frequency, corresponding to the magnetic inhomogeneity. The shift is caused by magnetic interactions including the electron-electron dipole interaction and the hyperfine interaction. The magnetization along y-axis (M_y) is described as the following equation:

$$M_y(t_{90}+\tau+t_{180}+t) \propto Tr\left\{\sigma(t_{90}+\tau+t_{180}+t)\cdot S_y\right\} \tag{8}$$

$$\propto \cos\left(\Delta\omega(\tau+t)\right) - \cos\left(\Delta\omega(\tau-t)\right) . \tag{9}$$

When t=τ, the second term in Eq.(9) is independent on $\Delta\omega$, indicating that all spins are in the same phase (parallel to the y-axis) and M_y reaches a maximum. The signal is referred to as electron spin echo (ESE).

In the standard Hahn echo stated as above, the magnetic inhomogeneity due to various interactions is cleverly eliminated. On the other hand, the eliminated magnetic interaction between

electron and electron/nuclear spins provides valuable information. Pulsed electron-nuclear double resonance (PENDOR) is developed to observe the electron-nuclear dipole (hyperfine) interaction, and pulsed electron-electron double resonance (PELDOR) to observe the electron-electron dipole interaction. Two electron spins in proximity are mutually related through the magnetic dipole interaction. The magnetic dipole interaction D_R is expressed by the following equation:

$$D_R = \frac{g_1 g_2 \beta^2}{R^3}\left(1 - 3\cos^2\theta_H\right) , \tag{10}$$

where g_1 and g_2 are the g-factors for each spin, R is the distance between the spins, and θ_H is an angle between the external magnetic field $\boldsymbol{H}$ and the vector $\boldsymbol{R}$ connecting the spins. In the PELDOR measurement, a second microwave pulse is irradiated between 90° and 180° pulses in Hahn echo sequence (Fig.G4). The second pump pulse induces a flip-flop of one spin in the interacting spins and leads to a change of the local magnetic field at the position of its partner spin via the magnetic dipole interaction D_R. As a result, the ESE signal observed with the Hahn echo sequence is perturbed, and its amplitude oscillates with the pump pulse as it scans between the 90° and 180° pulses. The oscillation of the echo amplitude $V(\tau,\tau')$ is characterized by the following equation:

$$V(\tau,\tau') \propto 1 - p\left[1 - \cos\left(D_R\tau'\right)\right] , \tag{11}$$

where p is the excitation probability for the pump pulse and τ' is a time interval between the first 90° probe and the second pump pulses. Therefore, the D_R can be estimated accurately based on the oscillation in the PELDOR signal, i.e. the distance R can be determined.

Method III; Time-resolved EPR (TR-EPR), used in chapter III.

In photosynthetic RC complex, the unpaired electron is transiently photo-induced and transferred through successive electron mediators, and the radical pair of the cation and anion radicals is formed. The transient radical pair state can be detected by time-resolved EPR spectroscopy. The spin system including two spins is described by the spin Hamiltonian as stated below:

$$\mathcal{H} = \mu_e H \cdot g_{e1} \cdot S_1 + \mu_e H \cdot g_{e2} \cdot S_2 + S_1 \cdot D_{SS} \cdot S_2 + S_1 \cdot J_{SS} \cdot S_2 , \tag{12}$$

where $\boldsymbol{g_{ei}}$ and $\boldsymbol{S_i}$ are the g-tensor and the spin operator for each i-th spin in the radical pair, respectively, and $\boldsymbol{D_{SS}}$ and $\boldsymbol{J_{SS}}$ are tensors for the magnetic dipole interaction and the exchange interaction between the two spins, respectively. The exchange interaction is usually assumed to be isotropic in the first

approximation. The dipole interaction is also assumed to be axially symmetric under the sufficiently long distance R compared to the molecular size. Based on these assumptions and the high magnetic field approximation, the spin Hamiltonian is redescribed as below:

$$\mathcal{H} = g_{e1}^{iso}\mu_e H_Z S_{1Z} + g_{e2}^{iso}\mu_e H_Z S_{2Z} + \frac{1}{2}D(\cos^2\theta - \frac{1}{3})(3S_Z^2 - S^2) - 2JS_1 \cdot S_2 \quad , \tag{13}$$

where g_{ei}^{iso} is the isotropic g-factor, H_Z is the external magnetic field along z-axis, S_{iZ} is the z-component of the spin operator, D is the strength of the perpendicular component of the dipole interaction, θ is an angle between the magnetic field direction and the vector connecting the two spins, and J is the isotropic exchange interaction. After diagonalization of the spin Hamiltonian, four eigenstates and eigenenergies are derived:

$$\begin{aligned} |1\rangle &= |T_{+1}\rangle & E_1 &= w - J + 1/2\, D_{ZZ} \\ |2\rangle &= \cos\psi|S\rangle + \sin\psi|T_0\rangle & E_2 &= \Omega - 1/2\, D_{ZZ} \\ |3\rangle &= -\sin\psi|S\rangle + \cos\psi|T_0\rangle & E_3 &= -\Omega - 1/2\, D_{ZZ} \\ |4\rangle &= |T_{-1}\rangle & E_4 &= -w - J + 1/2\, D_{ZZ} \end{aligned} \quad , \tag{14}$$

where

$$\begin{aligned} D_{ZZ} &= D(\cos^2\theta - \frac{1}{3}) \\ w &= \frac{1}{2}\left(g_{e1}^{iso} + g_{e2}^{iso}\right)\mu_e H_Z \\ \Omega &= \sqrt{\left(J + \frac{1}{2}D_{ZZ}\right)^2 + \left(\frac{1}{2}\left(g_{e1}^{iso} - g_{e2}^{iso}\right)\mu_e H_Z\right)^2} \\ \cos 2\psi &= \frac{J + 1/2 D_{ZZ}}{\Omega} \end{aligned} \quad , \tag{15}$$

where $|T_i\rangle$ and $|S\rangle$ are triplet and singlet ground states, respectively.

Figure G5-A shows the energy diagram for the spin system. In the electron transfer process, initial singlet state (S-state) becomes mixed with spin-triplet state (T_0-state), called the S-T_0 mixing (step B). The S-T_0 mixing results in the electron spin-polarized (ESP) state which exhibits aberrant energetic distribution distinct from Boltzmann distribution. The ESP state immediately decays to thermal equilibrium state (step C), followed by the charge recombination (step D). In the spin system with initial singlet pair, there are four transitions. The intensities I_{ij} and energy differences E_{ij}, corresponding to a transition between states i and j, are described as the following equations:

$$
\begin{aligned}
I_{12} &= 1/2(\sin^2\psi)(\cos^2\psi) & \Delta E_{12} &= w - \Omega - J + D_{ZZ} \\
I_{34} &= 1/2(\sin^2\psi)(\cos^2\psi) & \Delta E_{34} &= w - \Omega + J - D_{ZZ} \\
I_{13} &= 1/2(\sin^2\psi)(\cos^2\psi) & \Delta E_{13} &= w + \Omega - J + D_{ZZ} \\
I_{24} &= 1/2(\sin^2\psi)(\cos^2\psi) & \Delta E_{24} &= w + \Omega + J - D_{ZZ}
\end{aligned}
\quad . \qquad (16)
$$

Figure G5-B shows schematic ESP spectrum of an initial singlet radical pair with no hyperfine interactions. The ESP spectrum exhibits typical features as below; two pairs of emission (E) and absorption (A) peak were involved, in contrast to a conventional EPR signal in thermal equilibrium state including no emission peaks. The distribution of the E and A peaks depends strongly on the exchange (J) and dipolar interactions (D_{ZZ}) and g-factors (g_{ei}^{iso}). The J and D_{ZZ} reflect the relative arrangement of radicals forming a pair, and the g-tensor is associated with molecular orientation of the radical. Therefore, based on the ESP-EPR spectral shape, we can obtain structural information of the radical pair.

Figures

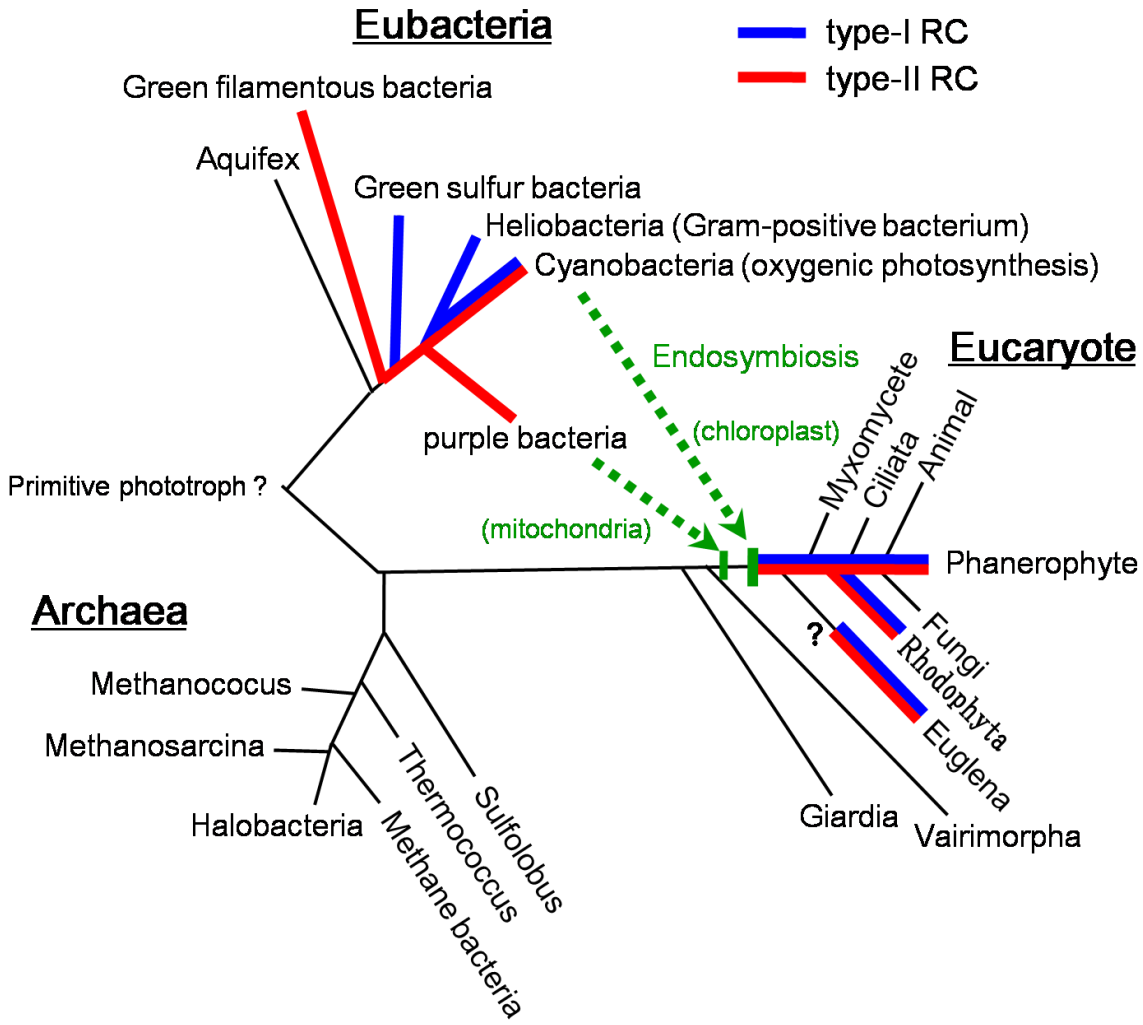

Figure G1: Phylogenetic tree based on the 16S rRNA sequence.

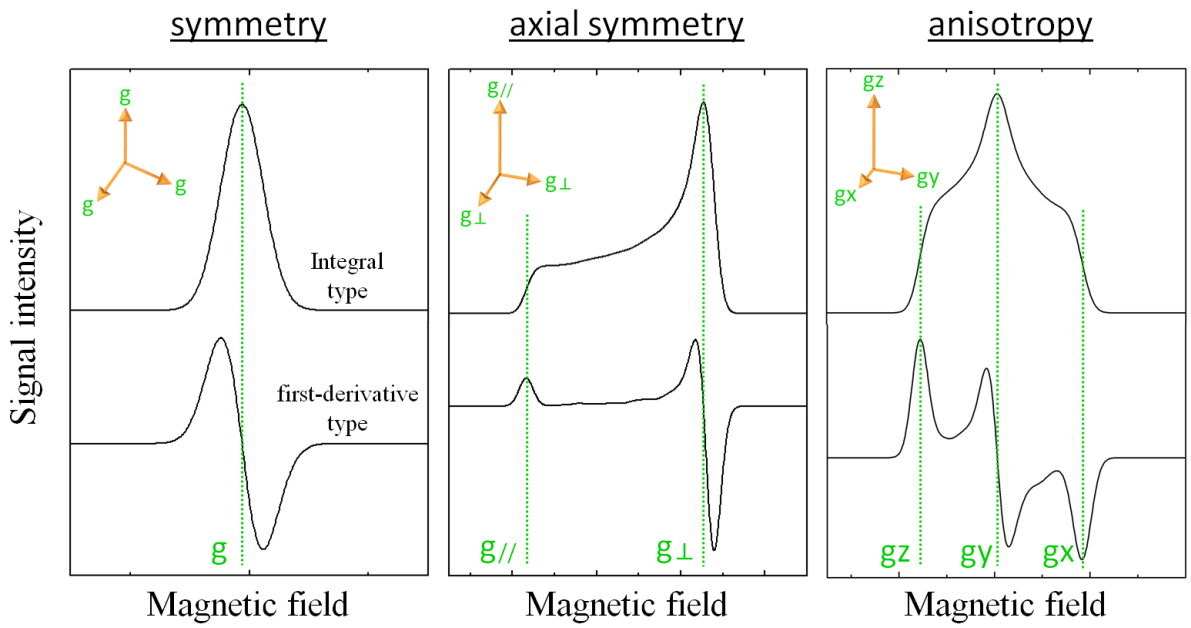

Figure G2: Typical CW EPR spectra associated with symmetry of the g-tensor. Upper spectra are shown as integral type, and lower are shown as first-derivative type.

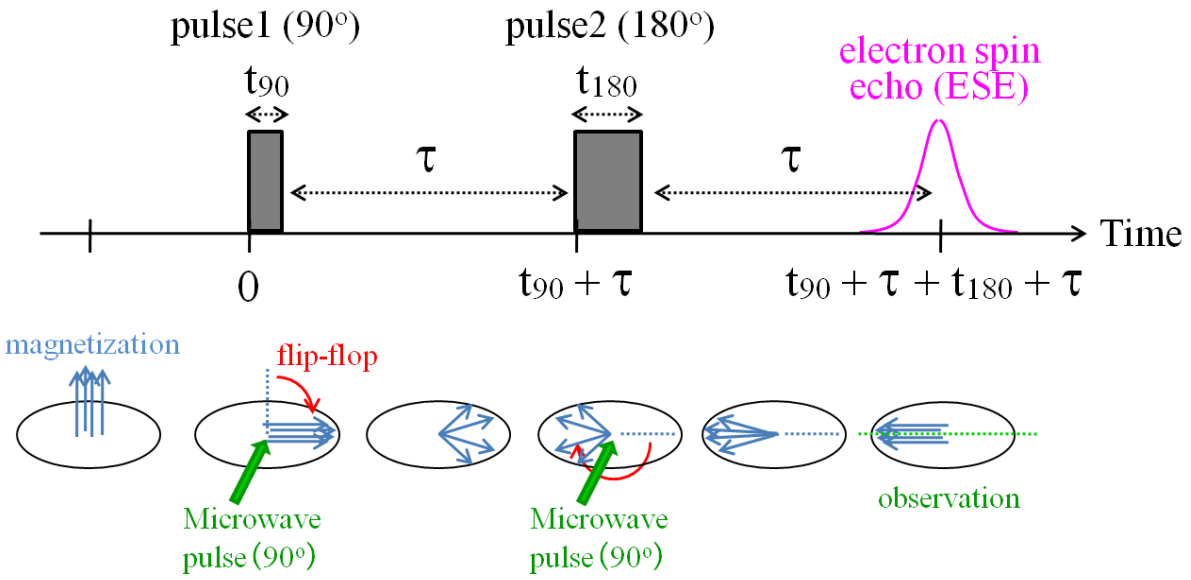

Figure G3: Pulse sequence for Hahn echo measurement (upper) and the magnetization vector model during the sequence (lower).

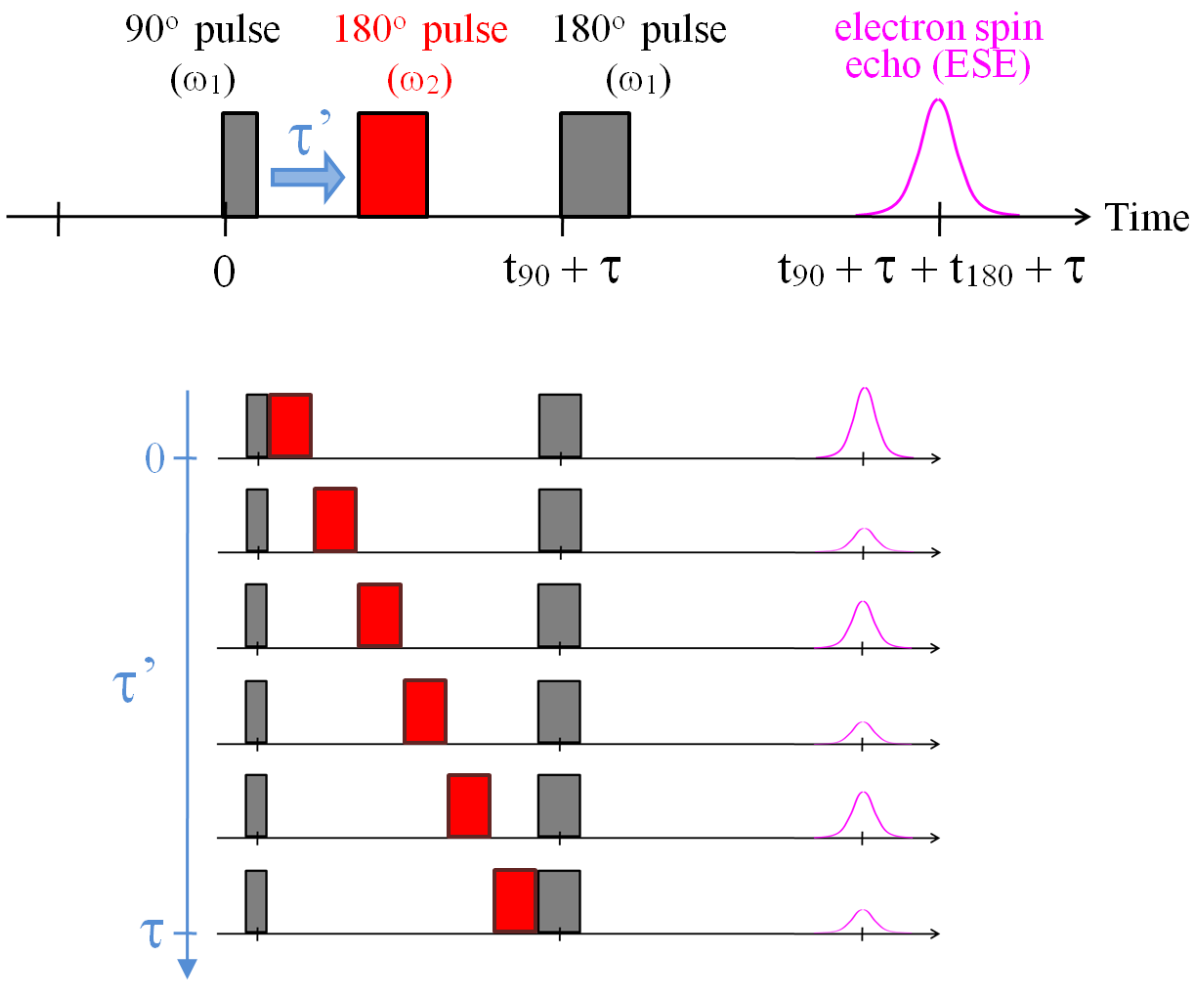

Figure G4: Pulse sequence for PELDOR measurement. The 90° and 180° pulses, which are represented in black squares, are employed to detect ESE. The another 180° pulse with different microwave frequency, which is represented in a red square, is added between the two pulses as a pump pulse to perturb the electron-electron dipole interaction between two spins. PELDOR spectrum is a plot of the ESE amplitude against time τ' that is an interval between first and second pulses.

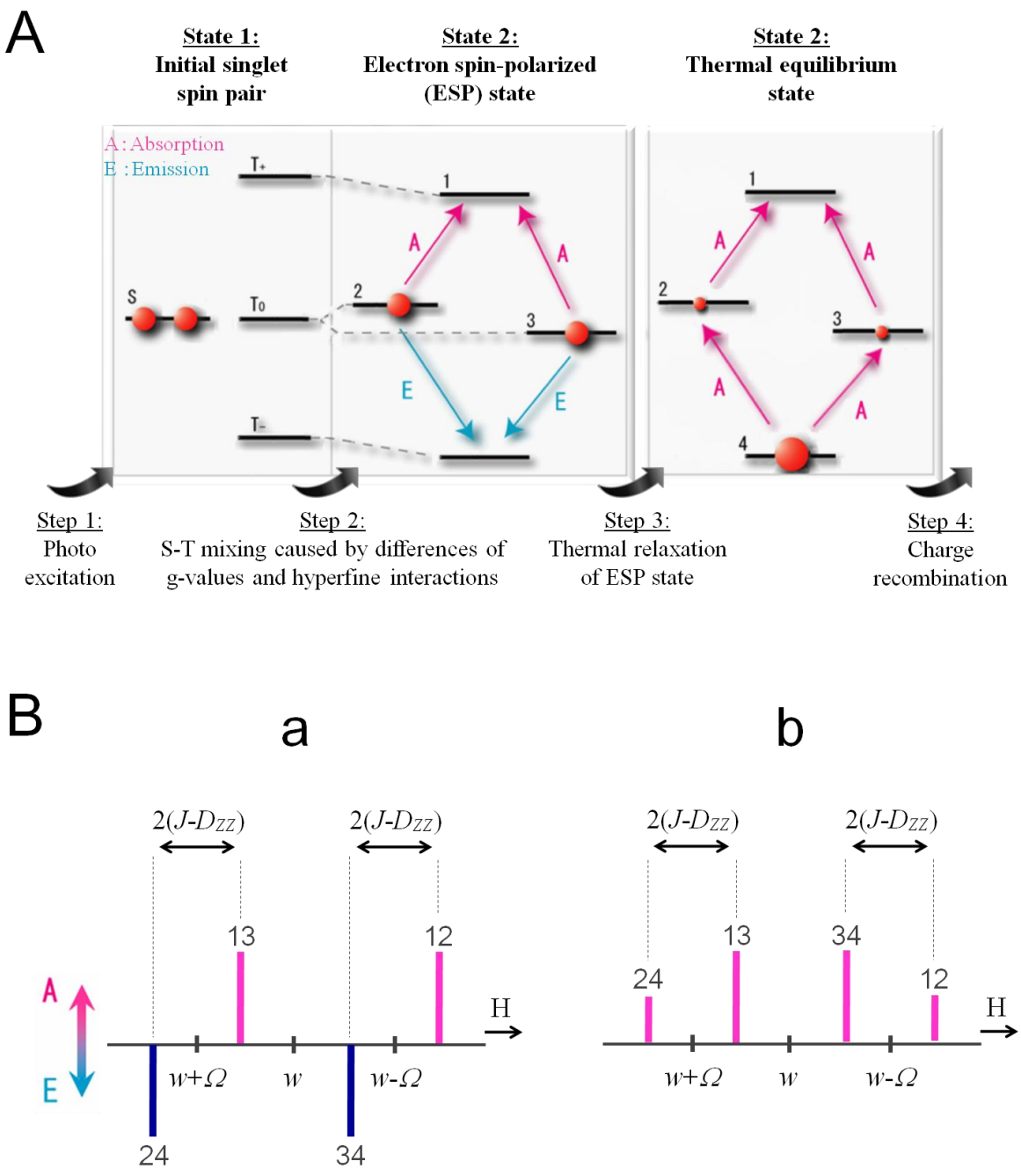

Figure G5: (A). Energy level diagram for the photo-induced radical pair. The size of red circles indicates the populations of the states and the arrows the directions of the transitions. The initial singlet radical pair is assumed in the spin system. (B). Schematic EPR spectra corresponding to (a) the ESP state and (b) the thermal equilibrium state, in which the hyperfine interaction is neglected. The stick spectrum corresponding to the transition between states *i* and *j* is indicated by '*ij*'.

Chapter I

Photo-induced radical pair in blue light sensory BLUF FAD protein, PixD

Chapter introduction

Photoreceptor proteins

Solar energy is essential to all of the living organisms on the earth, while sunlight is sometimes harmful to the biological body. Photoreceptor proteins developed in adaptation to the photoenvironment are also important for the efficient utilization of solar energy. The photoreceptors absorb specific light energies and induce various physiological responses. Six photoreceptor families which mediate light-induced signal transduction have been characterized [1]: phytochromes, rhodopsins, xanthopsins, cryptochromes, phototropins, and BLUF proteins (Fig.I-1). The former three protein families contain phytochromobilin, retinal, and coumaric acid as chromophores, respectively, that undergo light-induced cis-trans isomerization. The latter three contain flavin type chromophores: flavin mono nucleotide (FMN) in phototropins, and flavin adenine dinucleotide (FAD) in cryptochromes and BLUF proteins (Fig.I-2). The cryptochrome family functions as a blue/green light photoreceptor exhibiting high homology to DNA photolyase, and participates in various physiological processes such as synchronization of the circadian clock in animals, hypocotyls elongation, seed germination, and pigment accumulation [2]. It is proposed that a light-induced radical pair in cryptochrome of retinal functions as a chemical compass in animals such as migrant birds [3,4]. The phototropin family also has a blue light sensitive domain, referred to as light-oxygen-voltage (LOV) domain, and induces several light responses in plants such as phototropism, chloroplast movement, stomatal opening, and the rapid inhibition of hypocotyl growth [5].

The BLUF domain is a newly discovered blue light sensory photoreceptor protein that combines a FAD chromophore [6]. Five groups of the BLUF domain are physiologically characterized at present: PixD (SyPixD and TePixD in cyanobacteria *Synechocystis* sp. PCC6803 and *Thermosynechococcus elongatus,* respectively), AppA and BlrB in a purple photosynthetic bacterium *Rhodobacter sphaeroides* [6-8], PAC in *Euglena gracilis* [9], YcgF in *Escherichia coli* [10], and PapB in *Rhodopseudomonas palustris* [11]. The protein structures of TePixD, SyPixD, AppA, and BlrB were determined by X-ray crystallography [8,12-15]. PAC regulates the photophobic reaction [9,16] and YcgF and PapB control the biofilm formation [11,17], while PixD functions in the regulation of phototaxis in cyanobacteria.

Phototactic motility of cyanobacteria

Many cyanobacteria can move by gliding, twitching, or swimming without flagella that function as a molecular motor for cellular motility in algae or sperms of plants and animals. Type Ⅳ pilus radiating from a cell (Fig.I-3) seem to be utilized for twitching or gliding motility. Molecular

mechanism of the type Ⅳ pili-dependent motility has been unclear, unlike the well-known swimming motility associated with flagella. Since the entire genome sequence of cyanobacterium *Synechocystis* sp. PCC 6803, that exhibits twitching motility and positive phototaxis (i.e. movement toward a light source), was determined in 1996, genome analysis has revealed several essential genes for cell mobility [18].

The *pilG* (pilus assembly gene G) cluster was found to be regulatory genes controlling thick pilus biogenesis and resulting in cell motility (Fig.I-4A) [19]. The *Synechocystis* disruptants of *pix* genes in the *pixG* (positive phototaxis gene G) cluster lost the positive phototaxis faculty and move away from the light source (negative phototaxis) (Fig.I-4B), in which the phytochrome-like *pixJ1* gene is involved in the photochemical reaction [20]. Moreover, *slr1694* gene, including the BLUF domain, was found to be another bule light photoreceptor for the phototaxis reaction in *Synechocystis* [21]. Its gene product was defined as SyPixD (Synechocystis positive phototaxis D). The disruptions of the *slr1694* gene resulted in a phenotype of negative phototaxis (Fig.I-4C).

Figure I-4C shows that *Synechocystis* cells can sense light, and exhibits positive phototaxis response to 660 nm light but not to 460 nm light. An action spectrum of phototaxis indicated that yellow to red (560 to 720 nm) visible light induced positive phototactic behavior and UV light at shorter wavelength (360 nm) led to the negative phototaxis [22,23]. On the other hand, when high-intensity light was used, negative phototaxis was induced in response to both blue (470 nm) and red (600 to 700 nm) wavelength regions [23]. Thus, *Synechocystis* cells can sense the light intensity as well as the wavelength. Light energy is vital to photosynthetic organisms, while light at a short wavelength in a UV to blue region or excess light could induce photoinhibition in cyanobacterial cells even though the light is available to photosynthesis [24]. Therefore, cyanobacteria must respond to the photoenvironments (i.e. light intensity or quality). Two blue light photoreceptors PixJ1 and PixD seem to have the essential roles as switches between the positive and negative phototaxis. However, it is still unknown how the photoreceptors regulate the phototactic behavior of cells.

Photoreaction of FAD chromophore and following photo-degradation of SyPixD decamer

The structure of SyPixD was determined by X-ray crystallography (Fig.I-5) [12]. SyPixD oligomer shows a decameric structure formed of a pair of pentameric SyPixD rings (Fig.I-5A). Each SyPixD monomer contains one FAD as a chromophore in BLUF domain (Fig.I-5B). Figure I-5C shows the protein structure around the FAD. The Gln and Asn residues around the FAD are highly conserved in the BLUF proteins, and FAD is ligated to the adjacent residues through hydrogen-bonds (H-bonds). The excitation of FAD molecule with blue light induces multistep red-shifts of the FAD absorption band (Fig.I-6A) [25]. The spectral change seems to be due to the alteration of the H-bond network around FAD chromophore. Figure I-6B shows a photocycle scheme proposed in SyPixD.

The dark-adapted state (*D*-state) transforms to the first intermediate state exhibiting a 9 nm red-shift (I_9) below 150 K after illumination, followed by the formation of the second intermediate state (J_{14}) above 200 K. The J_{14}-state is also formed directly from *D*-state at 150~200 K. Subsequently, the J_{14}-state transforms to *F*-state above 240 K. The reaction temperatures correspond to the activation energies for each conformational change of the H-bond network. EPR studies showed the characteristic signal induced by illumination at 5-200 K in homologous TePixD [26]. The EPR signal was assigned to a radical pair of the flavin neutral radical ($FADH^{\bullet}$) and the adjacent tyrosine radical ($Y8^{\bullet}$) based on electron-nuclear double resonance (ENDOR) measurements [26].

Initial reaction immediately after the FAD photo-excitation was still unclear in PixD, while optical studies using ultrafast time-resolved spectroscopy suggested an initial reaction scheme in AppA, which is a blue light photoreceptor homologous with PixD (Fig. I-7A) [27]. It shows that charge separation associated with proton transfer between FAD and surrounding Tyr or Trp residue is induced after laser excitation. SyPixD also exhibited transient EPR signals due to a radical pair induced by illumination in both *D*- and *F*-states (Fig.I-7B) [28]. The spectrum is entirely similar to the light-induced EPR signal of the $FADH^{\bullet}$-$Y8^{\bullet}$ radical pair in TePixD [26]. Therefore, the $FADH^{\bullet}$-$Y8^{\bullet}$ radical pair would also be formed in SyPixD and seems to be associated with the following transformation of the H-bond network.

It is significant how the photo-induced local transformations around FAD lead to the signal transduction and to the eventual physiological reactions such as the phototactic movement of cells. Recently, Yuan and Bauer showed that PixD forms a large oligomeric structure in the presence of another protein denoted as PixE [29]. They revealed that PixE promotes the oligomerization of PixD from dimers into a stable decamer of a $PixD_{10}$-$PixE_5$ complex under dark conditions, and that the photo excitation of FAD induces disruption of the complex into PixD dimers and PixE monomers. The photo-degradation was proposed to be due to the photo-induced alternation of H-bonds, causing the flip of the Gln50 side chain and the position switch between Trp91 and Met93 (Fig.I-8A). FTIR studies indicated that the Trp91 and Met93 residues undergo major conformational changes in response to light [30,31]. The conformational changes in the vicinity of Trp91, composing the loop region located at the PixD dimer-dimer interface, were proposed to cause the degradation of a $PixD_{10}$-$PixE_5$ oligomer (Fig.I-8B). Figure I-9 shows a schematic model of the time-dependent conformational change of PixD oligomer based on Transient grating (TG) measurements [32]. Following the formation of *F*-state after FAD excitation, the photo-excited monomer changes the conformation with a time constant of 40 μs, and then the decameric structure undergoes conformational change with a time constant of 4 ms. The photo-induced protein dynamics is regarded as a significant process connecting local changes around FAD and signaling reactions.

Outline of this chapter

The FADH$^{\bullet}$-Y8$^{\bullet}$ radical pair induced in the initial photoreaction of PixD is suggested to be essential to the following H-bond rearrangement and the photo-degradation of PixD oligomer. I observed an electron spin echo (ESE) signal of the photo-induced radical pair in SyPixD by pulsed EPR spectroscopy. A calculated signal based on the crystal structure suggested that the signal arises from the FADH$^{\bullet}$-Y8$^{\bullet}$ radical pair. The dependency of the ESE signal on the microwave pulse strength indicated that the radical pair forms a complete triplet spin state ($\boldsymbol{S}$ = 1). The temperature dependence of the FADH$^{\bullet}$-Y8$^{\bullet}$ signal also indicated the ferromagnetic exchange coupling J of the radical pair. I estimated quantitatively the exchange coupling J to be 3~4 cm^{-1} by analysis of the temperature dependence of the spin-lattice relaxation rate. The value is much larger than even before in a biological system. The significantly large J indicates overlap of molecular orbitals of FADH$^{\bullet}$ and Y8$^{\bullet}$, seems to be due to the strong H-bond network between these cofactors. The exchange coupling J is known to affect an electron transfer rate [33], and thus might regulate the charge recombination rate of the FADH$^{\bullet}$-Y8$^{\bullet}$ radical pair that is expected to assist the efficient photoreaction in PixD.

The photo-degradation of PixD decamer, following the initial photoreaction, is expected to be important process for signal transduction of PixD. However, it is still unclear how the PixD oligomer is degraded in solution and how the PixD dimers and PixE monomer that are produced in the process lead to the regulation of phototactic behavior of cells. In this chapter, I utilized the FADH$^{\bullet}$-Y8$^{\bullet}$ radical pair as a spin label attached in each PixD monomer, and detected the magnetic dipole interaction between the spin labels of different monomers in one oligomer by PELDOR spectroscopy. Thereby, the protein-protein distance and relative orientation of proteins in SyPixD oligomer were determined. I established an analytical method to elucidate the photo-degradation process of PixD decamer in the signaling reaction.

Figures

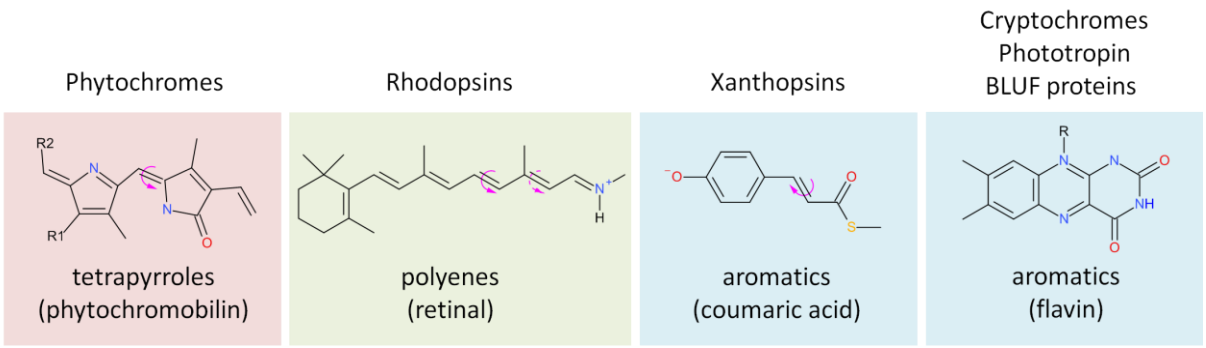

Figure I-1: Well-characterized classes of chromophores in six photoreceptor families [1]. Pink arrows indicate bonds that undergo the light-induced cis-trans isomerization.

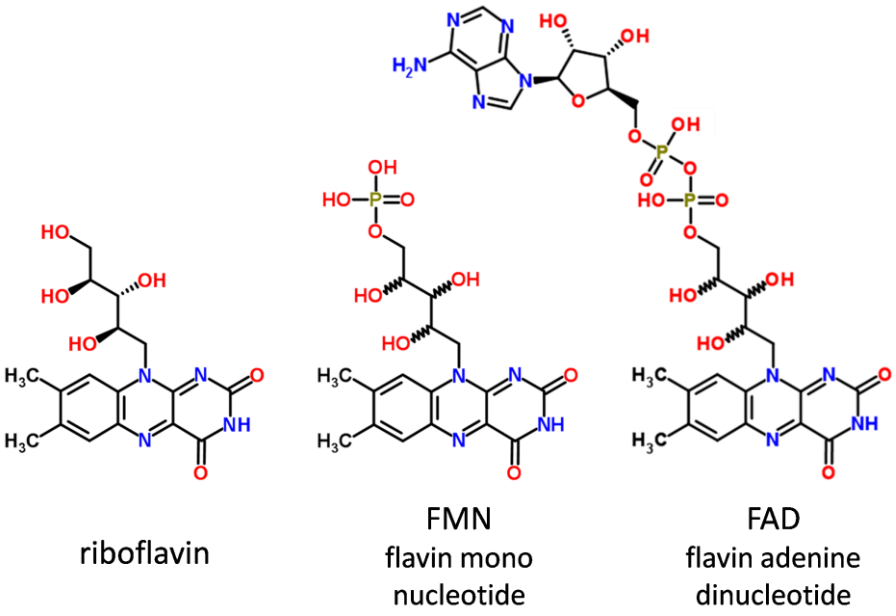

Figure I-2: Molecular structures of three flavin compounds associated with the photoreceptor.

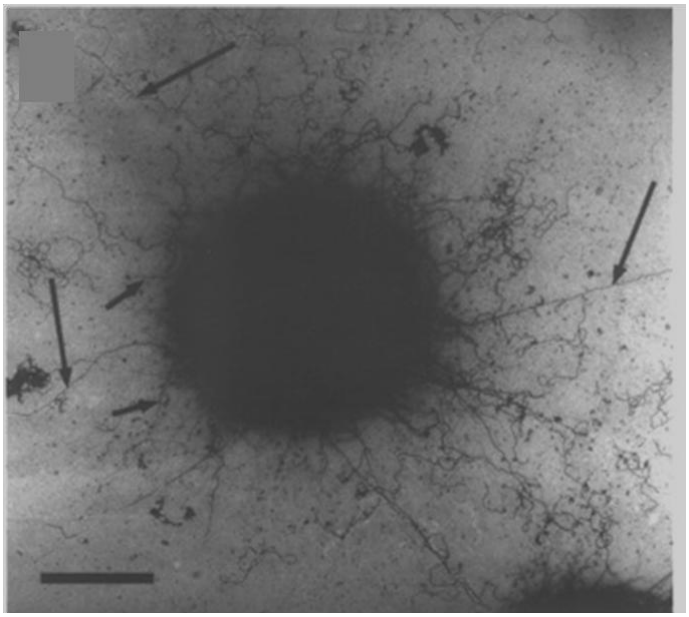

Figure I-3: Pilus structure on the cell surface of cyanobaterium *Synechocystis* sp. PCC 6803, observed by electron micrograph after negative staining. Long and short arrows indicate the thick and the thin pili, respectively. Scale bar indicates 1 μm. (The figure was quoted from [19])

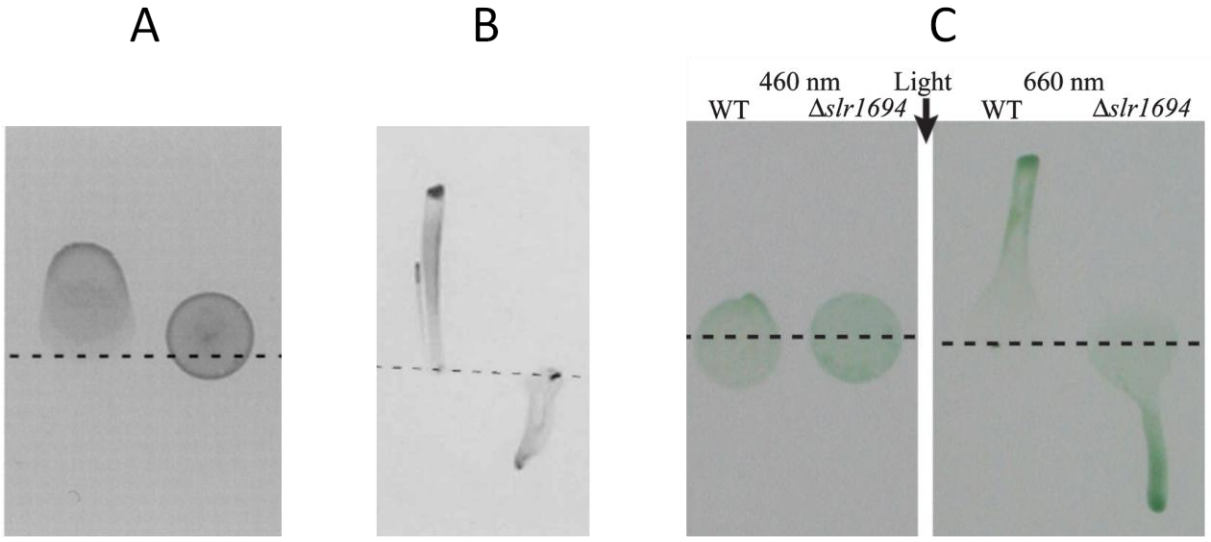

Figure I-4: Phototactic movements of colonies of the wild type cell (left lanes) and the gene-disrupted mutants (right lanes), in which (A) *slr1044* (*pilJ*) gene in *pilG* cluster, (B) *sll0044* (*pixJ1*) gene in *pixG* cluster, and (C) *slr1694* (*pixD*) gene were disrupted. Each cell was grown under lateral illumination from above (in the figure) with (A and B) a white fluorescent lamp and (C) monochromatic light at 460 (left panel) and 660 nm (right panel). Dotted lines show the initial position before the illumination. ((A), (B), and (C) were quoted from [19], [20], and [21], respectively)

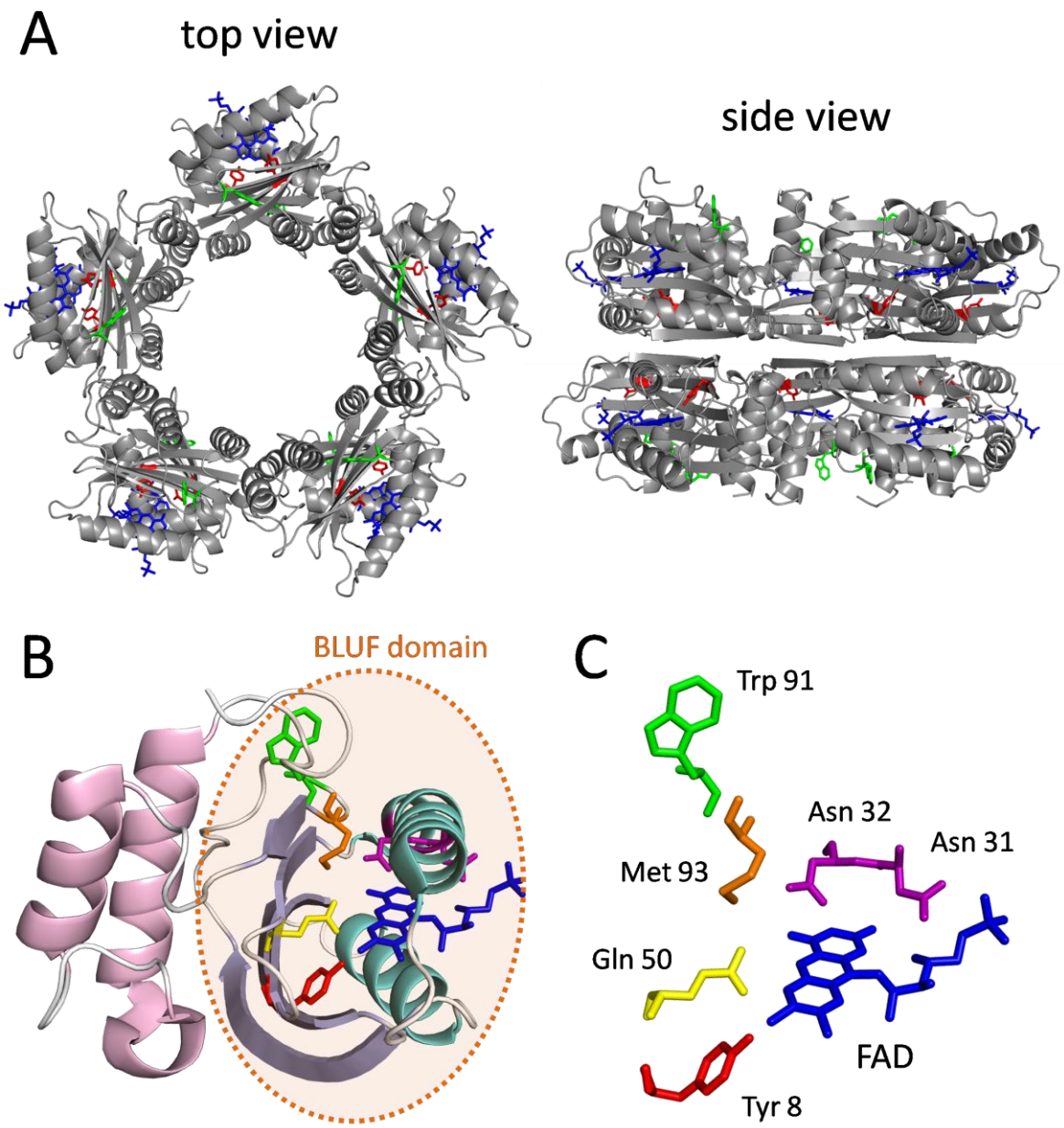

Figure I-5: X-ray crystal structure of SyPixD decamer from *Synechocystis* sp. PCC 6803 (PDB entry 2HFO) [12]. (A). Top view (left) and side view (right) of SyPixD decamer. (B). Structure of SyPixD monomer. BLUF domain is composed of several α-helices (in aqua) and β-strands (in light purple), which are formed of around 100 residues in N-terminal side. The other α-helices (in pink) seem to form the signal transduction domain, which are formed of around 50 residues in C-terminal side. (C). Local structure of FAD and surrounding residues in SyPixD. FAD, Tyr8, Trp91, Gln50, Met93, and Asn31 and 32 are represented in blue, red, green, yellow, orange, and purple, respectively.

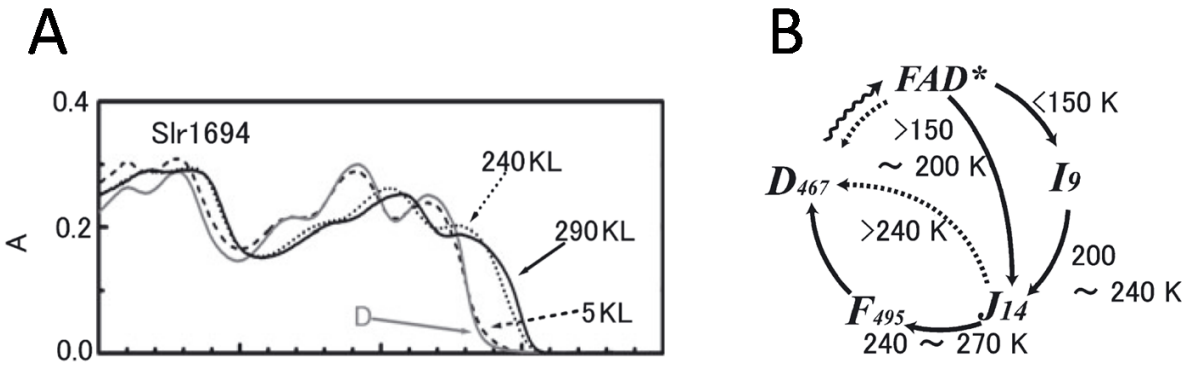

Figure I-6: (A). Absorption spectra of FAD chromophore in several intermediate states stably trapped at low temperatures in SyPixD. (B). Photocycle model of SyPixD, in which dark-adapted state is denoted as *D*-state, two intermediate states as *I*- and *J*-states, and red-shifted signaling state as *F*-state. (The figures were quoted from [25])

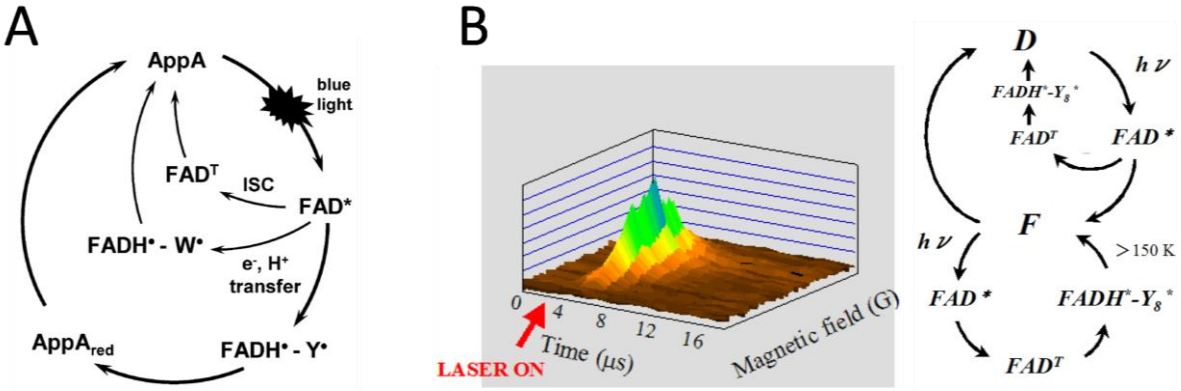

Figure I-7: (A). Photoreaction scheme immediately after FAD excitation in AppA, which shares homology with PixD. It was suggested based on ultrafast absorption and fluorescence experiments. (The figure was quoted from [27]) (B). Time-resolved EPR spectrum in SyPixD (left panel) and assumed photoreaction scheme immediately after FAD excitation in SyPixD (right panel). (The figures were quoted from [28])

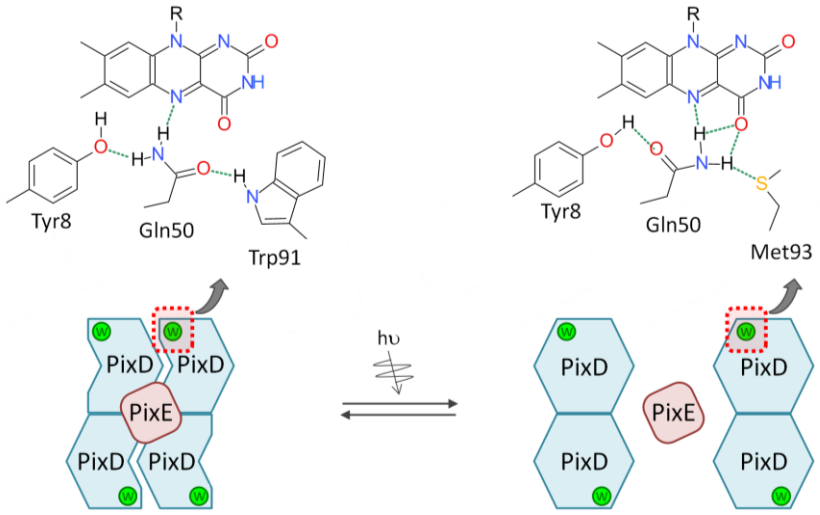

Figure I-8: Photo-degradation model of PixD decamer based on [29], in which four adjacent PixD monomers within a PixD decamer and a PixE monomer are represented. Green circle labeled by 'W' indicates the Trp91 residue around FAD, which is also shown in green in Fig.I-5. Photo-excitation induces alterations in the H-bond network around FAD chromophore (indicated by dotted red squares) as shown in the upper figures. The H-bond rearrangement sequentially induces conformational change around Trp91 in the loop region located at the PixD dimer-dimer interface, and results in photo-degradation of the decamer.

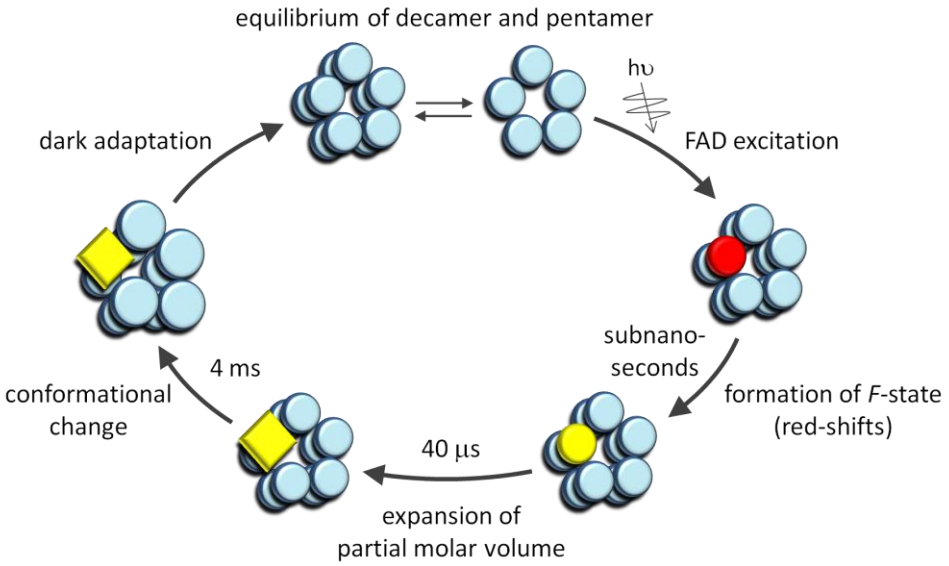

Figure I-9: Schematic model of the time-dependent conformational change of PixD oligomer based on TG measurements [32]. PixD monomers in *D*-state (grand state), FAD excited-state, and *F*-state (signaling state) are represented in right blue, red, and yellow, respectively. Small circles indicate ground state conformation of PixD monomer, while large circles and squares indicate altered conformations. The symbol shapes distinguish different conformations of PixD. The decamer and the pentamer are in equilibrium in the dark.

References

[1] Van der Horst, M.A. and Hellingwerf, K.J. (2004) Photoreceptor proteins, "star actors of modern times": A review of the functional dynamics in the structure of representative members of six different photoreceptor families, Acc. Chem. Res. 37, 13-20.

[2] 和田正三，徳富哲，長谷あきら，長谷部光泰，植物の光センシング；光情報の受容とシグナル伝達 （秀潤社，東京都, 2001）

[3] Gegear, R.J., Casselman, A., Waddell, S. and Reppert, S.M. (2008) Cryptochrome mediates light-dependent magnetosensitivity in *Drosophila*, Nature 454, 1014-1018.

[4] Maeda, K., Henbest, K.B., Cintolesi, F., Kuprov I., Rodgers, C.T., Liddell, P.A., Gust, D., Timmel, C.R. and Hore, P.J. (2008) Chemical compass model of avian magnetoreception, Nature 453, 387-390.

[5] Christie, J.M., Swartz, T.E., Bogomolni, R.A. and Briggs, W.R. (2002) Phototropin LOV domains exhibit distinct roles in regulating photoreceptor function, Plant J. 32, 205-219.

[6] Gomelsky, M. and Klug, G. (2002) BLUF: a novel FAD-binding domain involved in sensory transduction in microorganisms, Trends Biochem. Sci. 27, 497-500.

[7] Masuda, S. and Bauer, C.E. (2002) AppA is a blue light photoreceptor that antirepresses photosynthesis gene expression in *Rhodobacter sphaeroides*, Cell 110, 613-623.

[8] Jung, A., Domratcheva, T., Tarutina, M., Wu, Q., Ko, W.H., Shoeman R.L., Gomelsky M,, Gardner K.H., Schlichting I. (2005) Structure of a bacterial BLUF photoreceptor: Insights into blue light-mediated signal transduction, Proc. Natl. Acad. Sci. U. S. A. 102, 12350-12355.

[9] Iseki, M., Matsunaga, S., Murakami, A., Ohno, K., Shiga. K., Yoshida, K., Sugai, M., Takahashi, T., Hori, T. and Watanabe, M. (2002) A blue-light-activated adenylyl cyclase mediates photoavoidance in *Euglena gracilis*, Nature 415, 1047-1051.

[10] Rajagopal, S., Key, J.M., Purcell, E.B., Boerema, D.J. and Moffat, K. (2004) Purification and initial characterization of a putative blue light-regulated phosphodiesterase from *Escherichia coli*, Photochem. Photobiol. 80, 542-547.

[11] Kanazawa, T., Ren, S., Maekawa, M., Hasegawa, K., Arisaka, F., Hyodo, M., Hayakawa, Y., Ohta, H., and Masuda, S. (2010) Biochemical and physiological characterization of a BLUF protein-EAL protein complex involved in blue light-dependent degradation of cyclic diguanylate in the purple bacterium *Rhodopseudomonas palustris*, Biochemistry 49, 10647-10655.

[12] Yuan, H., Anderson, S., Masuda, S., Dragnea, V., Moffat, K. and Bauer, C. (2006) Crystal structures of the *Synechocystis* photoreceptor Slr1694 reveal distinct structural states related to signaling, Biochemistry 45, 12687-12694.

[13] Jung, A., Reinstein, J., Domratcheva, T., Shoeman, R.L. and Schlichting, I. (2006) Crystal structures of the AppA BLUF domain photoreceptor provide insights into blue light-mediated signal transduction, J. Mol. Biol. 362, 717-732.

[14] Kita, A., Okajima, K., Morimoto, Y., Ikeuchi, M. and Miki, K. (2005) Structure of a cyanobacterial BLUF protein, Tll0078, containing a novel FAD-binding blue light sensor domain, J. Mol. Biol. 349, 1-9.

[15] Anderson, S., Dragnea, V., Masuda, S., Ybe, J., Moffat, K. and Bauer, C. (2005) Structure of a novel photoreceptor, the BLUF domain of AppA from *Rhodobacter sphaeroides*, Biochemistry 44, 7998-8005.

[16] Ito, S., Murakami, A., Sato, K., Nishina, Y., Shiga, K., Takahashi, T., Higashi, S., Iseki, M., and Watanabe, M. (2005) Photocycle features of heterologously expressed and assembled eukaryotic flavin-binding BLUF domains of photoactivated adenylyl cyclase (PAC), a blue-light receptor in *Euglena gracilis*, Photochem. Photobiol. Sci. 4, 762-769.

[17] Tschowri, N., Busse, S. and Hengge, R. (2009) The BLUF-EAL protein YcgF acts as a direct anti-repressor in a blue-light response of *Escherichia coli*, Genes Dev. 23, 522-534.

[18] Yoshihara, S. and Ikeuchi, M. (2004) Phototactic motility in the unicellular cyanobacterium *Synechocystis* sp PCC 6803, Photochem. Photobiol. Sci. 3, 512-518.

[19] Yoshihara, S., Geng, X. and Ikeuchi, M. (2002) pilG gene cluster and split pilL genes involved in pilus biogenesis, motility and genetic transformation in the cyanobacterium *Synechocystis* sp PCC 6803, Plant Cell Physiol. 43, 513-521.

[20] Yoshihara, S., Suzuki, F., Fujita, H., Geng, X.X. and Ikeuchi, M. (2000) Novel putative photoreceptor and regulatory genes required for the positive phototactic movement of the unicellular motile cyanobacterium *Synechocystis* sp PCC 6803, Plant Cell Physiol. 41, 1299-1304.

[21] Okajima, K., Yoshihara, S., Fukushima, Y., Geng, X.X., Katayama, M., Higashi, S., Watanabe, M., Sato, S., Tabata, S., Shibata, Y., Itoh, S., and Ikeuchi, M. (2005) Biochemical and functional characterization of BLUF-type flavin-binding proteins of two species of cyanobacteria, J. Biochem. 137, 741-750.

[22] Choi, J.S., Chung, Y.H., Moon, Y.J., Kim, C., Watanabe, M., Song, P.S., Joe, C.O., Bogorad, L., and Park, Y.M. (1999) Photomovement of the gliding cyanobacterium *Synechocystis* sp PCC 6803, Photochem. Photobiol. 70, 95-102.

[23] Ng, W.O., Grossman, A.R. and Bhaya, D. (2003) Multiple light inputs control phototaxis in *Synechocystis* sp strain PCC6803, J Bacteriol. 185, 1599-1607.

[24] Tyystjarvi, T., Tuominen, I., Herranen, M., Aro, E.M. and Tyystjarvi, E. (2002) Action spectrum of psbA gene transcription is similar to that of photoinhibition in Synechocystis sp

PCC 6803, FEBS Lett. 516, 167-171.

[25] Fukushima, Y., Okajima, K., Ikeuchi, M. and Itoh, S. (2007) Two intermediate states I and J trapped at low temperature in the photocycles of two BLUF domain proteins of cyanobacteria Synechocystis sp PCC6803 and *Thermosynechococcus elongatus* BP-1, Photochem. Photobiol. 83, 112-121.

[26] Nagai, H., Fukushima, Y., Okajima, K., Ikeuchi, M. and Mino, H. (2008) Formation of Interacting Spins on Flavosemiquinone and Tyrosine Radical in Photoreaction of a Blue Light Sensor BLUF Protein TePixD, Biochemistry 47, 12574-12582.

[27] Gauden, M., Grinstead, J.S., Laan, W., van Stokkum, H.M., Avila-Perez, M., Toh, K.C., Boelens, R., Kaptein, R., van Grondelle, R., Hellingwerf, K.J., and Kennis, J.T.M. (2007) On the role of aromatic side chains in the photoactivation of BLUF domains, Biochemistry 46, 7405-7415.

[28] 筒井和彦，青色光センサータンパク質 SyPixD の光反応過程の解析 （修士論文，名古屋大学，2010）

[29] Yuan, H. and Bauer, C.E. (2008) PixE promotes dark oligomerization of the BLUF photoreceptor PixD, Proc. Natl. Acad. Sci. U. S. A. 105, 11715-11719.

[30] Masuda, S., Hasegawa, K., Ishii, A. and Ono, T. (2004) Light-induced structural changes in a putative blue-light receptor with a novel FAD binding fold sensor of blue-light using FAD (BLUF); Slr1694 of *Synechocystis* sp PCC6803, Biochemistry 43, 5304-5313.

[31] Masuda, S., Hasegawa, K. and Ono, T. (2005) Light-induced structural changes of apoprotein and chromophore in the sensor of blue light using FAD (BLUF) domain of AppA for a signaling state, Biochemistry 44, 1215-1224.

[32] Tanaka, K., Nakasone, Y., Okajima, K., Ikeuchi, M., Tokutomi, S. and Terazima, M. (2009) Oligomeric-state-dependent conformational change of the BLUF protein TePixD (Tll0078), J Mol. Biol. 386, 1290-1300.

[33] Kobori, Y., Yago, T., Akiyama, K. and Tero-Kubota, S. (2001) Determination of electron-transfer reorganization energy in nanometer-separated radical ion pair by time-resolved EPR spectroscopy, J. Am. Chem. Soc. 123, 9722-9723.

Temperature dependence of relaxation time of a stable radical pair in SyPixD investigated by pulsed EPR

Introduction

Many flavoproteins are known to function in biological redox processes. Recently a new type of photoreceptor using flavin, referred to as the BLUF (Blue-Light Using FAD) domain, was developed [1]. Four groups of the BLUF domain are known at present: PixD (SyPixD in *Synechocystis* sp. PCC6803 or TePixD in *Thermosynechococcus elongatus)*, AppA and BlrB in *Rhodobacter sphaeroides* [1-3], PAC in *Euglena gracilis* [4], and YcgF in *Escherichia coli* [5]. PixD regulates pili-dependent cell motility [6], andAppA controls the expression of the photosynthesis gene [7]. The BLUF domain shows a reversible 10-20 nm red-shift of the flavin absorption bands upon light excitation at room temperature [2,3,6,8-10]. The red-shifted form (denoted as *F*) decays back to the dark-adapted state (denoted as *D*) within 10-30 min. The structures of TePixD, SyPixD, AppA, and BlrB have been determined by X-ray crystallography and nuclear magnetic resonance (NMR) spectroscopy [3,7,11-14]. Figure 1 shows (A) the protein structure of SyPixD around the flavin molecule and (B, C) the molecular structure of flavin and tyrosine.

Fourier transform infrared (FTIR) and Raman spectroscopic studies have shown that the vibration of the C_4=O group in flavin is weakened in the red-shifted form, which suggest stronger hydrogen bonding [8,15-22]. It was proposed that Gln50 also forms a hydrogen bond with N_5 (or additionally O_4) of flavin in the dark and alters it during photoreaction because themutant protein, which has Ala in place of Gln50 (Q50A), doesnot achieve the red-shifted form [14]. The dark-adapted state and the red-shifted state of PixD are denoted as *D* and *F*, respectively. The molecular structure of TePixD suggests that Tyr8 interacts with flavin through a FAD-Gln50-Tyr8 hydrogen-bond network [12], where Tyr8 is a hydrogen-bond donor to Gln50 in both the dark and light states [23]. Replacement of tyrosine with phenylalanine (Y8F in TePixD and SyPixD, Y21F in AppA, and Y472F in PACR-F2) abolished the photo-conversion activity at physiological temperatures [16,24-28]. Therefore, the electron transfer between flavin and tyrosine is proposed as being essential for the light reaction [29].

Recently, we have found an electron paramagnetic resonance (EPR) signal arising from TePixD [30]. The signal was light-induced at 5-150 K and stably trapped at low temperature. The signal occurred after the 2nd photo-excitation of the photo-induced red-shifted states in the photocycle of TePixD. The lineshape of the signal shows typical magnetic dipole-dipole interaction (Pake

doublet). Based on the pulsed ENDOR and site-directed mutation results, it was concluded that the signal was arising from the radical pair between the flavin neutral radical ($FADH^{\bullet}$) and tyrosine ($Y8^{\bullet}$). The distance between the radicals was estimated to be 6.9 Å, assuming point-dipole approximation. In this paper, we have studied the EPR properties of the stable $FADH^{\bullet}$-$Y8^{\bullet}$ radical pair in order to clarify the reactions and the sensor mechanism in detail.

Materials and methods

Sample preparation

SyPixD (*Slr1694*) was purified according to the previously reported method [31]. The protein was dissolved in a medium containing 50 mM Tris/HCl and 1 mM NaCl (pH 8.0). Photosystem II membranes were prepared from spinach according to the previously described method [32] with a slight modification [33]. The membranes were dissolved in a medium containing 400 mM sucrose, 20 mM NaCl and 20mM Mes/NaOH (pH 6.5).

EPR measurements

Continuous wave (CW) EPR measurements were performed using a Bruker ESP-300E EPR spectrometer with a gas flow temperature control system (CF935, Oxford Instruments, Oxford, GB). A standard resonator (ER4102, Bruker) was used. Electron spin echo (ESE) experiments were performed on a pulsed EPR spectrometer (ESP-380, Bruker) using a two-pulse (primary) ESE sequence. The spectrometer was equipped with a cylindrical dielectric cavity (ER4117DHQ-H, Bruker) and a gas flow temperature-control system (CF935, Oxford Instruments). Microwave pulses of 16 and 24 ns duration were used for the $\pi/2$ and π pulse sequence, respectively. Field-swept ESE spectra were measured by the $\pi/2$-τ-π sequence at a time interval τ of 200 ns between the microwave pulses. The spin-lattice relaxation time was measured by inversion recovery for the π-T-$\pi/2$-τ-π pulse sequence at a time interval τ of 200 ns.

Samples were illuminated using light froma 408 nm diode laser (ITC 510, Thorlabs) through a 1 mm diameter glass fiber.

Results and discussion

Figure 2 shows (a) CW and (b) ESE field-swept EPR signals of light-induced radicals in SyPixD. The sample was illuminated at 150 K and subsequently frozen into 50 K under illumination. The EPR lineshape consists of large inner peaks and small outer peaks, which typical for a magnetic dipole-dipole interaction (Pake doublet). The peak separations are 7.5 and 15 mT for the inner and outer peaks, respectively. An identical signal was found for TePixD [30], where the peak separations were 8.5 and 17 mT for the inner and outer peaks, respectively. The slight difference in the peak separations is ascribed to the slight difference in the local structure of SyPixD and TePixD. The dotted line in Fig.2 shows a simulated spectrum based on the crystal structure of SyPixD [7]. Previous reported [30] spin distributions for the flavin and tyrosine molecules were used. Based on the crystal structure, electron-electron dipolar interactions between spin density distributions on both radicals were calculated and summed. The *g*-factors for both molecules were assumed to be *g*=2. The stick spectrum was convoluted usinga Gaussian function with a width of 2.5 mT. The results show the protein structure with a Pake doublet, which is the same as the crystal structure. Nagai et al. reported a structural modification around flavin moleculeof approximately 2.3 Å compared to crystal structure of TePixD [30]. However, there is no structural modification in TePixD after reexamination of EPR simulations based on the crystal structure of TePixD.

Figure 3 shows the H_1-dependence of the ESE-signal amplitude. Traces *a* and *b* were measured at the field position of the lower maximum peak (bold array in Fig. 2) and the central field position of the peak-to-trough of the Pake doublet signal (dotted array in Fig. 2), respectively. Trace *c* was measured in the $Y_D^{\bullet}$ signal of photosystem II as a standard of $\boldsymbol{S}$ = 1/2 with g = 2. The horizontal axis is normalized by H_{1max}, which is the maximum H_1 fed to the resonator. A density matrix formalism [34] for a two-pulse ESE sequence with pulses of the same amplitude and pulse-lengths of t_p and $2t_p$ shows that the ESE signal intensity for resonant spins is proportional to $sin^3(2g\beta H_1 \langle S_x \rangle t_p)$, where $\langle S_x \rangle$ is a matrix element of the transition operator for the case of $H_1 // x$ and $H_0 \perp x$. Traces *d* and *e* represent calculations of the H_1-dependence of the ESE-signal amplitude. The H_1-dependence of spin $\boldsymbol{S}$ = 1/2 with g = 2 (trace *d*) was fitted by trace *c*. Trace *e* shows calculated H_1-dependence of the spin $\boldsymbol{S}$ = 1 with g = 2. The dot-dashed and dotted lines show the maximum amplitude of the $\boldsymbol{S}$ = 1/2 and $\boldsymbol{S}$ = 1, respectively. The concurrence of traces *a* and *e* shows that the Pake doublet signal is characterized by the complete $\boldsymbol{S}$ = 1 spin. Subtle overlapping of the $\boldsymbol{S}$ = 1/2 spin system is observed in trace *b*, which is ascribed to the overlapping of an accumulated $FADH^{\bullet}$ radical during long illumination at g = 2 [30].

The radical pair spin-Hamiltonian for two spins, $\boldsymbol{S_1}$ and $\boldsymbol{S_2}$ of $\boldsymbol{S}$=1/2, was taken in the following form:

$$\aleph = g_1\beta H_0 S_{1z} + g_2\beta H_0 S_{2z} + S_{1z}\sum_j a_{1j}m_{1j} + S_{2z}\sum_k a_{2k}m_{2k} + (-2J + D)S_{1z}S_{2z}$$
$$-\left(J + \frac{D}{4}\right)\left(S_1^+ S_2^- + S_1^- S_2^+\right) \quad , \tag{1}$$

where g_1 and g_2 are the g-factor for each spin and β is the Bohr magneton. The values a_{1j}, a_{2k} and m_{1j}, m_{1k} are the hyperfine constants and the nuclear spin projections on $\boldsymbol{H_0}$, respectively. The exchange interaction J is defined as $\aleph_{ex} = -2\boldsymbol{J}\boldsymbol{S}_1 \cdot \boldsymbol{S}_2$, and dipole interaction D is defined as

$$D = \frac{g_1 g_2 \beta^2}{R^3}\left(1 - 3\cos^2\theta\right) \quad , \tag{2}$$

where θ is the angle between the direction of the external magnetic field $\boldsymbol{H_0}$ and the radius-vector $\boldsymbol{r}$ joining spin 1 and spin 2. The spin properties under the interaction defined by Eq.(1) are characterized by the amplitude of $|\delta|$ and $|J + D/4|$. δ is defined as

$$\delta = \left[(g_1 - g_2)\beta H_1 + \sum_j a_1 m_{1j} - \sum_k a_2 m_{2k}\right]/2 . \tag{3}$$

The results show that the spin system has $\boldsymbol{S} = 1$. Therefore, the Pake doublet signal is concluded to arise from complete $\boldsymbol{S} = 1$ triplet state with the upper limited condition $|\delta| << |J + D/4|$.

Figure 4 shows the temperature dependence of the CW EPR spectrum of the Pake doublet signal forSyPixD. The signal amplitude was measured at the field position of the lower maximum of the Pake doublet signal. The signal amplitude is inverselyproportional to the temperature, and is defined as Curie law behavior. The temperature dependence of the population of the $\boldsymbol{S} = 1$ state [35] is proportional to

$$\frac{1}{k_B T}\frac{3\exp(2J/k_B T)}{1+3\exp(2J/k_B T)} \quad , \tag{4}$$

Ferromagnetic coupling $J > 0$ derives the ground state for $\boldsymbol{S} = 1$ triplet. Antiferromagnetic coupling $J < 0$ derives the excited triplet state for $\boldsymbol{S} = 1$. In the case of ferromagnetic coupling $J > 0$, the temperature dependence of the amplitude is indistinguishable from the Curie law behavior. The obtained temperature dependence supports the Pake doublet signal arising from the ground state for the triplet state in $J > 0$. In the case of antiferromagnetic coupling $J < 0$, J is available only for small J (< -0.5 K) for reproduction of the obtained temperature dependence.

The amplitude of J in the coupled spin system is a function of the spin inter-distance R [Å]. Coffman and Buettner [36] showed the dependence of the distance on J and estimated the upper limit

J [cm^{-1}] as

$$|2J_{\mathrm{lim}}| = 1.35\times10^{7}\exp(-1.80R) \quad . \tag{5}$$

Assuming a point dipole approximation, the inter-distance of the spins in the Pake doublet signal was estimated as R = 7.2 Å, which gives$|2J|$ = 32cm^{-1}. Although this is not valid for a point dipole approximation because the electron spin is delocalized, the value may providea reference as to the upper limit of J.

The spin-lattice relaxation time $T_1$was measured. Figure 5 shows the inversion-recovery traces observed at (*a*) 4, (*b*) 8, (*c*) 20 and (*d*) 80 K, respectively, and the *inset* shows an expansion of trace *d*. Biphasic recovery traces were detected at all temperatures. Two exponential functions are used for fitting the time constants, denoted as T_{1fast} and T_{1slow}. At 4 K, time constants of 197 μs for T_{1fast} and 4.95 ms for T_{1slow} were obtained. By increasing the temperature, both components of T_{1fast} and T_{1slow} became gradually shorter. Although manifold relaxation processes for spin-lattice relaxation are proposed, the Raman and Orbach processes would be possible at low temperature above 2 K [37]. If a low-lying excited spin state exists, then the Orbach process can dominate the relaxation pathway [38,39]. Each relaxation process has a different temperature dependence. The temperature dependence of the relaxation rates for the Orbach and Raman processes was expressed as [37]

$$\frac{1}{T_1} = A_{Orb}\frac{\Delta^3}{\exp(\Delta/k_BT)-1} + A_{Ram}\left(\frac{T}{\theta_D}\right)^9 J_8\left(\frac{\theta_D}{T}\right) \quad , \tag{6}$$

where T is the temperature, A_{Orb} is the coefficient for the contribution from the Orbach process, Δ is the energy gap between the ground state and excited state for the Orbach process, A_{Ram} is the coefficient for the contribution from the Raman process, θ_{D} is the Debye temperature, J_8 is the transport integral as in the following equations:

$$J_8\left(\frac{\theta_D}{T}\right) = \int_0^{\theta_D/T} X^8\frac{e^x}{(e^x-1)^2}\,dx \quad , \tag{7}$$

The Orbach process represents that the inverse of T_1 is in proportion to $exp(-\Delta/k_BT)$. The Raman process is roughly estimated as the inverse of T_1 in proportion to T^x ($3 \le x \le 9$) [40]. Figure 6 shows the natural log of the calculated electron spin-lattice relaxation rate of the Pake doublet signal plotted against (A) the natural log of the temperature and (B) inverse temperature. A difference in the slopes of both these plots is found at around 16-20 K. Panel A explores the possibility that the Raman process provides the dominant relaxation pathway, in which case the rate can be expected to

vary as a high power of the temperature: $1/T_1 \propto T^x$ ($3 \leq x \leq 9$) [40]. Above 20 K, the slope of the graph corresponds to $T^{2.5\pm0.2}$, assuming the slope is linear. Below 16 K, the slope of the graph is gentler. Panel B explores the possibility that the Orbach process provides the dominant relaxation pathway, in which case the ratio can be expected to vary exponentially with inverse temperature: $1/T_1 \propto exp(-\Delta/k_BT)$. The slope of the lineis equal to 11.4 K (7.92 cm^{-1}) below 16 K and 81.5 K (56.6 cm^{-1}) above 20 K, which corresponds to the energy gap (Δ) between the ground and excited states, respectively.

Figure 7 shows the temperature dependence of the slow components of the spin-lattice relaxation. The natural log of the calculated electron spin-lattice relaxation rate of the Pake doublet signal is plotted against (A) the natural log of the temperature and (B) inverse temperature. As in Fig 6, a difference in the slopes of both plots is found at around 16 - 20 K. Panel A explores the possibility of the Raman process. Above 20 K, the slope of the graph corresponds to $T^{2.7}$, assuming that the slope is linear. Panel B explores the possibility of the Orbach process; the slope is equal to 9.0 K (6.3 cm^{-1}) below 16 K and 101 K (70.2 cm^{-1}) above 20 K, which corresponds to Δ between the ground and excited states, respectively.

If we assume that the relaxation below 16 K is caused by the Raman process and estimate the slope of the graph, then the power dependence of the temperature is less than $T^{1.6}$ below 16 K for T_{1fast} and T_{1slow}, which is smaller than that expected from the Raman process. Therefore, the relaxation process below 16 K is reasonably assigned to the Orbach process.

It is noteworthy that the energy gaps obtained from the Orbach plot of the T_{1fast} and T_{1slow} components coincide well, which indicates that both components are influenced by the same relaxation mechanism. Therefore, the energy gap Δ = 9 – 11 K (6 - 8 cm^{-1}) is ascribed to the energy gap between the triplet ground state and the excited singlet state. Above 20 K, both the Orbach and Raman plots are compatible for fitting of T_{1fast} and T_{1slow}. Based on the Orbach plot, the energy gaps were estimated as Δ = 82 K (57 cm^{-1}) for T_{1fast} and Δ = 101 K (70.2 cm^{-1}) for T_{1fast}. These values are too large for exchange coupling, as they are larger than the upper limit for $2J$ estimated by the inter-distance. Therefore, the relaxation processes above 20 K would be ascribed to the Raman process, which is consistent with the Orbach process occurring below 16 K. Measurements at higher temperatures above 100 K are difficult, because signal intensities are small and the lifetime of the Pake doublet signal is shorter. Therefore, there is insufficient data to interpret the temperature dependence of T_1 between 20 and 100 K. Although it is possible that the relaxation process arises from thermal process, we tentatively ascribed the relaxation process to the Raman process. The boldlines in Figs. 6A and 7A are fitted lines based on Eq. (6). The A_{ram} and Debye temperatures θ_D are estimated to be $A_{ram} = 1.1 \times 10^8$ and θ_D = 229 K for T_{1fast}, and $A_{ram} = 7.9 \times 10^6$ and θ_D = 185 K for T_{1slow}.

The inversion-recovery is susceptible to the effects of spectral diffusion. Therefore, the obtained T_1 should be evaluated as the effective T_1. In order to evaluate the effect of spectral diffusion, a picket fence sequence, where five series of π/2 pulses with long intervals are used for initial spin inversion [37], was attempted at several temperatures. According to the T_{1fast} phase, the rates were slightly reduced up to 20%. On the other hand, according to T_{1slow} phase, similar rates were obtained as those in inversion-recovery. This indicates that the spectral diffusion has more influence on T_{1fast}. The difference of Δ estimated by T_{1fast} and T_{1slow} might be caused by spectral diffusion effects. To completely eliminate the effect of spectral diffusion, saturation recovery would be required.

Similar EPR signals are observed in synthesized organic molecules with delocalized spin S=1 [41-43]. The amount of exchange interaction depends on the overlap of the molecular orbital. Okazawa and Ishida reported that the spins with R = 4.5 Å via hydrogen bonding gives $|2J|$ = 23 cm^{-1} [44]. It would be possible that the exchange interaction between $FADH^{\bullet}$ and $Y8^{\bullet}$ is connected with hydrogen-bonding network.

In conclusion, the Pake doublet signal arises from a complete $\boldsymbol{S}$ = 1 triplet state with ferromagnetic coupling, and the energy gap between the singlet and the triplet is estimated as $2J$ = 6 to 8 cm^{-1}. These results support the idea that the $FADH^{\bullet}$-$Y8^{\bullet}$ radical pair is located with proximity and overlap of the molecular orbital.

Figures

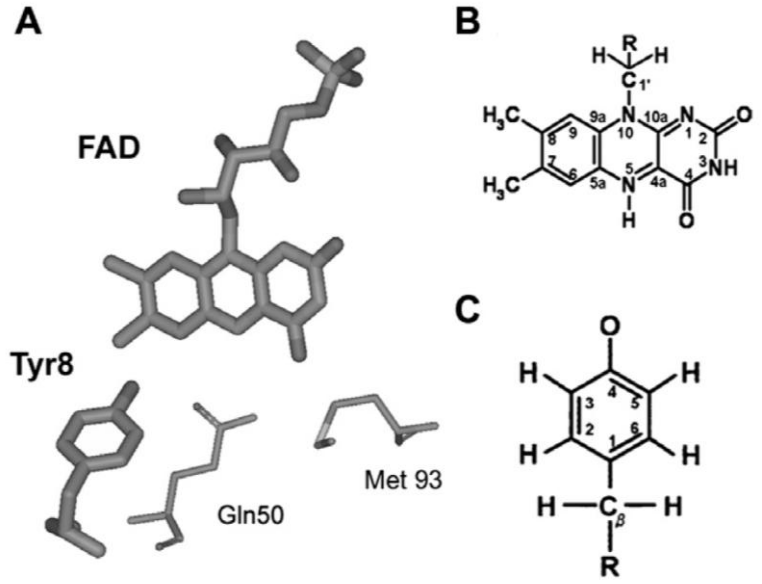

Figure 1: (A) Local structure of FAD and surrounding SyPixD (PDB entry 2HFO, chain A) [7]. Molecular structures of (B) neutral flavinosemiquinone (FADH) and (C) tyrosine.

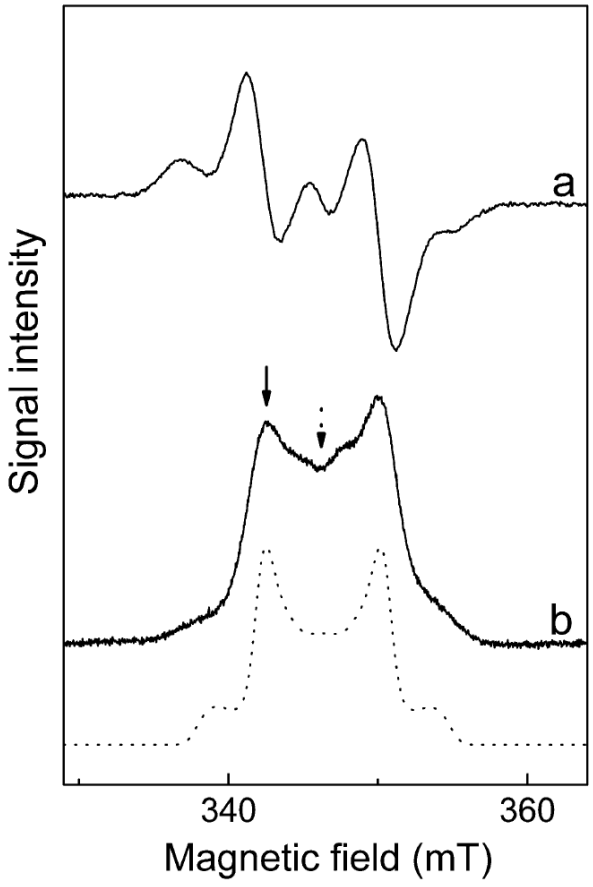

Figure 2: (a) CW and (b) primary ESE field-swept EPR spectra of SyPixD. Sample was illuminated at 150 K and subsequently cooled to 77 K under illumination. The horizontal axis for trace *a* was fitted to trace *b*. The dotted line is the simulated EPR spectrum is based on the crystal structure [7]. Spin distributions of flavin and tyrosine molecules from ref [30] were used. The stick spectrum was convoluted usinga Gaussian function with a width of 2.5 mT. Experimental conditions for CW EPR: microwave power, 1 mW; microwave frequency, 9.53 GHz; modulation amplitude, 0.3 mT; temperature, 150 K. Experimental conditions for pulsed EPR: microwave frequency, 9.66 GHz; duration of the microwave pulses, 16 and 24 ns; repetition rate, 0.1 kHz; temperature, 10 K. The time between the second and third pulse was τ = 400 ns.

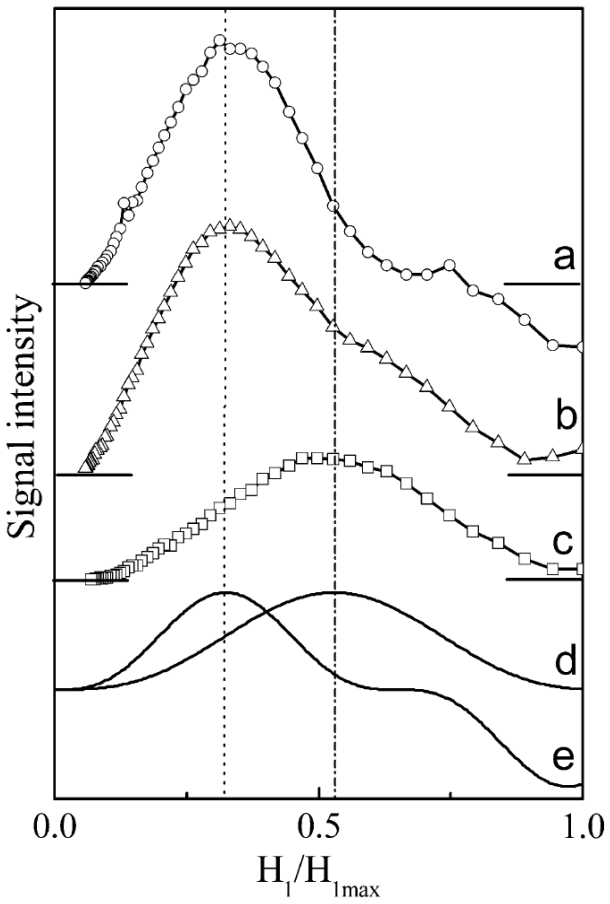

Figure 3: H_1-dependency of the primary ESE signal amplitude in the Pake doublet signal measured at (a) 340.5 mT (the low field maximum of the Pake doublet signal, indicated by the bold arrow in Fig.2) and (b) 344.2 mT (the central field in the peak-to-trough of the Pake doublet signal, indicated by the dotted arrow in Fig.2). (c) H_1-dependency of the primary ESE signal amplitude for the $Y_D^{\bullet}$ signal of photosystem II. (d, e) Calculated H_1-dependency for (d) $\boldsymbol{S}$ = 1/2 and (e) $\boldsymbol{S}$ = 1 (see text). The measurement conditions were the same as those in Fig.2b.

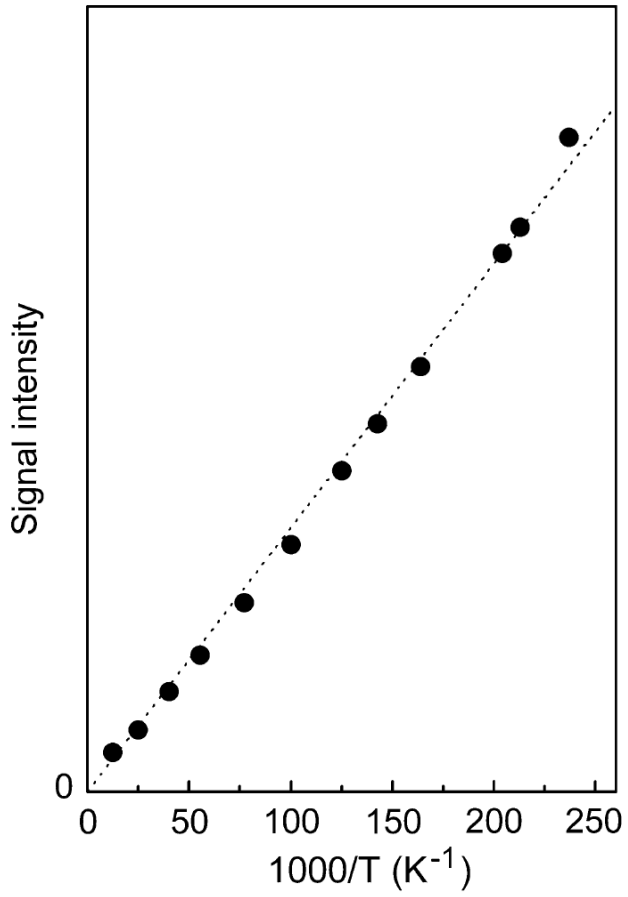

Figure 4: Temperature dependence of the amplitude in the Pake doublet signal. The signals were measured at 334.4 mT (the low field maximum of the CW spectrum in the Pake doublet signal). The dotted line shows the fitting with a linear function. The measurement conditions were the same as those used in Fig.2a except for the temperature and magnetic field.

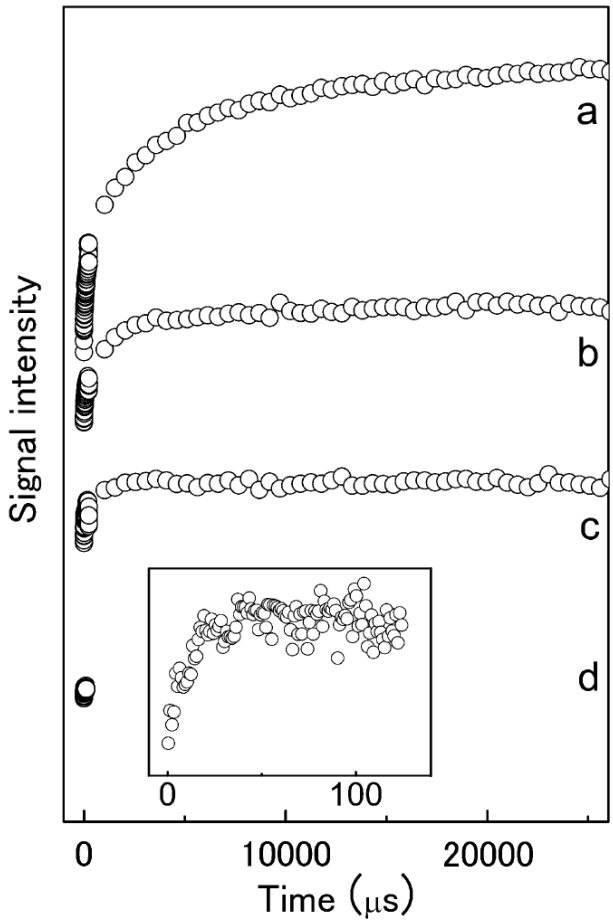

Figure 5: Inversion-recovery traces of the primary ESE signal amplitude in the Pake doublet signal measured at (*a*) 4, (*b*) 8, (*c*) 20 and (*d*) 80 K. The *inset* shows an expansion of trace *d*. The signals were measured at the low field maximum of the Pake doublet signal. Experimental conditions: duration of the microwave pulses, 24, 16 and 24 ns; repetition rate, 0.02 – 0.1 kHz. The time between the second and third pulse was τ = 200 ns. Other conditions are the same as in Fig.2b.

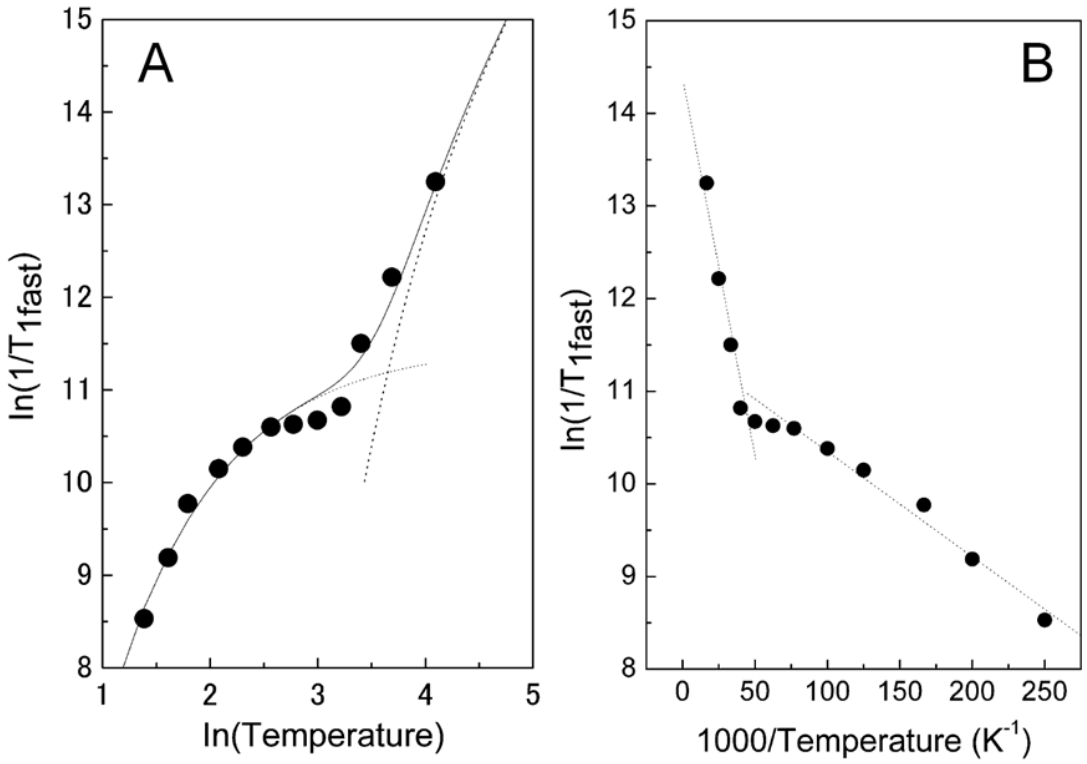

Figure 6: Temperature dependence of the spin-lattice relaxation rate of the fast components in the Pake doublet signal for SyPixD. (A) Natural log of temperature versus the relaxation rate (Raman plot). The bold line shows thefit based on Eq. (6). A_{Ram}= 1.1×10^{8} and the Debye temperature θ_D = 229 K. The dotted lines are components for the Orbach (lower temperature) and Raman processes (higher temperature), respectively. (B) Inverse temperature versus relaxation rate (Orbach plot). The dotted lines show the fitted linear functions, which were separated below 16 K and above 20 K.

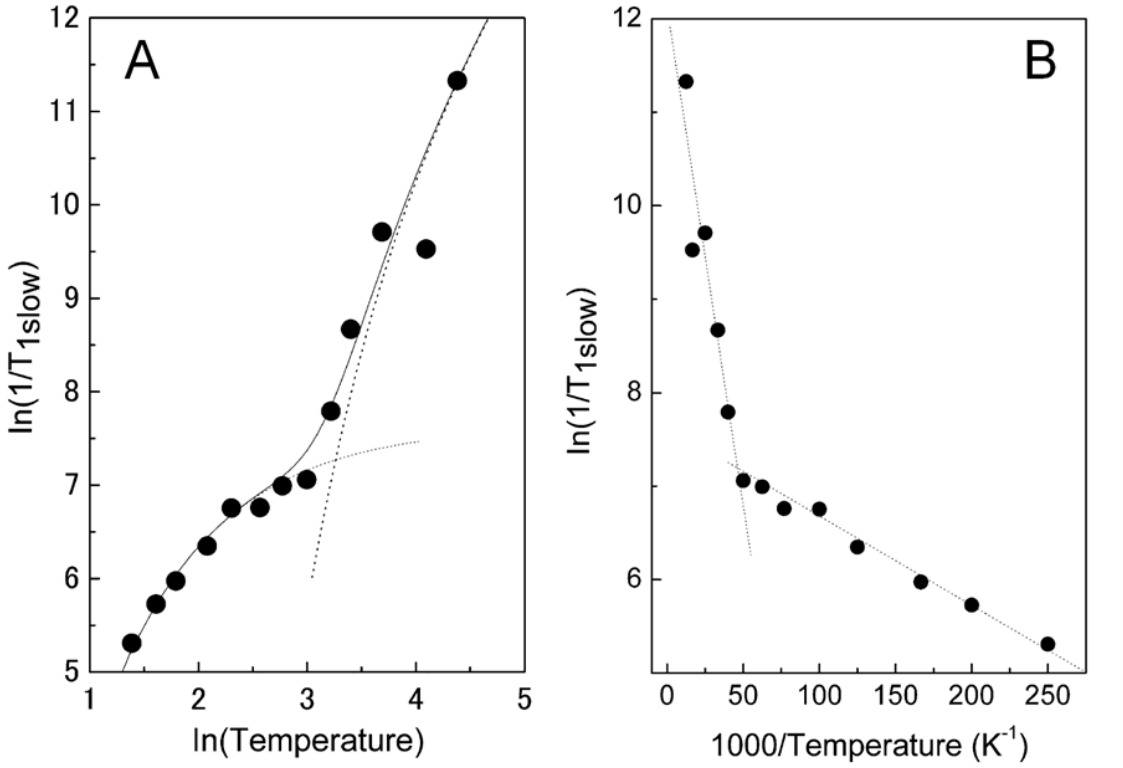

Figure 7: Temperature dependence of the spin-lattice relaxation rate of the slow components in the Pake doublet signal for SyPixD. (A) Natural log of the temperature versus the relaxation rate (Raman plot). The bold line shows the fit based on Eq. (6). A_{Ram}= 7.9×10^6 and the Debye temperature θ_D= 185 K. The dotted lines are components for the Orbach (lower temperature) and Raman processes (higher temperature), respectively. (B) Inverse temperature versus relaxation rate (Orbach plot). The dotted lines show the fitted linear functions, which were separated below 16 K and above 20 K.

References

[1] Gomelsky, M. and Klug, G. (2002) BLUF: a novel FAD-binding domain involved in sensory transduction in microorganisms, Trends Biochem. Sci. 27, 497-500.

[2] Masuda, S. and Bauer, C.E. (2002) AppA is a blue light photoreceptor that antirepresses photosynthesis gene expression in *Rhodobacter sphaeroides*, Cell 110, 613-623.

[3] Jung, A., Domratcheva, T., Tarutina, M., Wu, Q., Ko, W.H., Shoeman, R.L., Gomelsky, M., Gardner, K.H., and Schlichting, I. (2005) Structure of a bacterial BLUF photoreceptor: Insights into blue light-mediated signal transduction, Proc. Natl. Acad. Sci. USA 102, 12350-12355.

[4] Iseki, M., Matsunaga, S., Murakamik, A., Ohno, K., Shiga, K., Yoshida, K., Sugai, M., TakahashiI, T., Hori, T., and Watanabe, M. (2002) A blue-light-activated adenylyl cyclase mediates photoavoidance in *Euglena gracilis*, Nature 415, 1047-1051.

[5] Rajagopal, S., Key, J.M., Purcell, E.B., Boerema, D.J. and Moffat, K. (2004) Purification and initial characterization of a putative blue light-regulated phosphodiesterase from *Escherichia coli*, Photochem. Photobiol. 80, 542-547.

[6] Okajima, K., Yoshihara, S., Fukushima, Y., Geng, X., Katayama, M., Higashi, S., Watanabe, M., Sato, S., Tabata, S., Shibata, Y., Itoh, S., and Ikeuchi, M. (2005) Biochemical and functional characterization of BLUF-type flavin-binding proteins of two species of cyanobacteria, J. Biochem. 137, 741-750.

[7] Yuan, H., Anderson, S., Masuda, S., Dragnea, V., Moffat, K. and Bauer, C. (2006) Crystal structures of the *Synechocystis* photoreceptor Slr1694 reveal distinct structural states related to signaling, Biochemistry 45, 12687-12694.

[8] Laan, W., van der Horst, M.A., van Stokkum, I.H. and Hellingwerf, K.J. (2003) Initial characterization of the primary photochemistry of AppA, a blue-light-using flavin adenine dinucleotide-domain containing transcriptional antirepressor protein from *Rhodobacter sphaeroides*: A key role for reversible intramolecular proton transfer from the flavin adenine dinucleotide chromophore to a conserved tyrosine?, Photochem. Photobiol. 78, 290-297.

[9] Fukushima, Y., Okajima, K., Shibata, Y., Ikeuchi, M. and Itoh, S. (2005) Primary intermediate in the photocycle of a blue-light sensory blue-light FAD-protein, Tll0078, of *Thermosynechococcus elongatus* BP-1, Biochemistry 44, 5149-5158.

[10] Zirak, P., Penzkofer, A., Schiereis, T., Hegemann, P., Jung, A. and Schlichting, I. (2006) Photodynamics of the small BLUF protein BlrB from Rhodobacter sphaeroides, J. Photochem. Photobiol., B 83, 180-194.

[11] Jung, A., Reinstein, J., Domratcheva, T., Shoeman, R.L. and Schlichting, I. (2006) Crystal

structures of the AppA BLUF domain photoreceptor provide insights into blue light-mediated signal transduction, J. Mol. Biol. 362, 717-732.

[12] Kita, A., Okajima, K., Morimoto, Y., Ikeuchi, M. and Miki, K. (2005) Structure of a cyanobacterial BLUF protein, Tll0078, containing a novel FAD-binding blue light sensor domain, J. Mol. Biol. 349, 1-9.

[13] Anderson, S., Dragnea, V., Masuda, S., Ybe, J., Moffat, K. and Bauer, C. (2005) Structure of a novel photoreceptor, the BLUF domain of AppA from Rhodobacter sphaeroides, Biochemistry 44, 7998-8005.

[14] Grinstead, J.S., Hsu, S.T.D., Laan, W., Bonvin, A.M.J.J., Hellingwerf, K.J., Boelens, R. and Kaptein, R. (2006) The solution structure of the AppA BLUF domain: Insight into the mechanism of light-induced signaling, Chembiochem 7, 187-193.

[15] Hasegawa, K., Masuda, S. and Ono, T. (2004) Structural intermediate in the photocycle of a BLUF (sensor of blue light using FAD) protein Slr1694 in a cyanobacterium *Synechocystis* sp PCC6803, Biochemistry 43, 14979-14986.

[16] Hasegawa, K., Masuda, S. and Ono, T. (2005) Spectroscopic analysis of the dark relaxation process of a photocycle in a sensor of blue light using FAD (BLUF) protein Slr1694 of the cyanobacterium *Synechocystis* sp PCC6803, Plant Cell Physiol. 46, 136-146.

[17] Hasegawa, K., Masuda, S. and Ono, T. (2006) Light induced structural changes of a full-length protein and its BLUF domain in YcgF(Blrp), a blue-light sensing protein that uses FAD (BLUF), Biochemistry 45, 3785-3793.

[18] Masuda, S., Hasegawa, K. and Ono, T. (2005) Adenosine diphosphate moiety does not participate in structural changes for the signaling state in the sensor of blue-light using FAD domain of AppA, FEBS Lett. 579, 4329-4332.

[19] Masuda, S., Hasegawa, K. and Ono, T. (2005) Light-induced structural changes of apoprotein and chromophore in the sensor of blue light using FAD (BLUF) domain of AppA for a signaling state, Biochemistry 44, 1215-1224.

[20] Masuda, S., Hasegawa, K. and Ono, T. (2005) Tryptophan at position 104 is involved in transforming light signal into changes of beta-sheet structure for the signaling state in the BLUF domain of AppA, Plant Cell Physiol. 46, 1894-1901.

[21] Unno, M., Masuda, S., Ono, T. and Yamauchi, S. (2006) Orientation of a key glutamine residue in the BLUF domain from AppA revealed by mutagenesis, spectroscopy, and quantum chemical calculations, J. Am. Chem. Soc. 128, 5638-5639.

[22] Unno, M., Sano, R., Masuda, S., Ono, T. and Yamauchi, S. (2005) Light-induced structural changes in the active site of the BLUF domain in AppA by Raman spectroscopy, J. Phys. Chem. B 109, 12620-12626.

[23] Takahashi, R., Okajima, K., Suzuki, H., Nakamura, H., Ikeuchi, M. and Noguchi, T. (2007) FTIR study on the hydrogen bond structure of a key tyrosine residue in the flavin-binding blue light sensor TePixD from *Thermosynechococcus elongatus*, Biochemistry 46, 6459-6467.

[24] Okajima, K., Fukushima, Y., Suzuki, H., Kita, A., Ochiai, Y., Katayama, M., Shibata, Y., Miki, K., Noguchi, T., Itoh, S., and Ikeuchi, M. (2006) Fate determination of the flavin photoreceptions in the cyanobacterial blue light receptor TePixD (T110078), J. Mol. Biol. 363, 10-18.

[25] Ito, S., Murakami, A., Sato, K., Nishina, Y., Shiga, K., Takahashi, T., Higashi, S., Iseki, M., Watanabe, M. (2005) Photocycle features of heterologously expressed and assembled eukaryotic flavin-binding BLUF domains of photoactivated adenylyl cyclase (PAC), a blue-light receptor in Euglena gracilis, Photoch. Photobio. Sci. 4, 762-769.

[26] Dragnia, V., Anderson, S., Masuda, S., Waegelle, M., Balascuta, S., Ybe, J., Dragnea, B., Moffat, K., Bauer, C. (2005) Crystallographic and functional studies of the AppA blue-light receptor BLUF domain from *Rhodobacter sphaeroides*, Abstr. Pap. Am. Chem. Soc. 230, U2809.

[27] Gauden, M., van Stokkum, I. H. M., Key, J. M., Luhrs, D. C., Van Grondelle, R., Hegemann, P., Kennis, J. T. M. (2007) On the role of aromatic side chains in the photoactivation of BLUF domains, Biochemistry 46, 7405-7415.

[28] Kraft, B.J., Masuda, S., Kikuchi, J., Dragnea, V., Tollin, G., Zaleski, J.M. and Bauer, C.E. (2003) Spectroscopic and mutational analysis of the blue-light photoreceptor AppA: A novel photocycle involving flavin stacking with an aromatic amino acid, Biochemistry 42, 6726-6734.

[29] Gauden, M., van Stokkum, I.H.M., Key, J.M., Luhrs, D.C., Van Grondelle, R., Hegemann, P. and Kennis, J.T.M. (2006) Hydrogen-bond switching through a radical pair mechanism in a flavin-binding photoreceptor, Proc. Natl. Acad. Sci. USA 103, 10895-10900.

[30] Nagai, H., Fukushima, Y., Okajima, K., Ikeuchi, M. and Mino, H. (2008) Formation of interacting spins on flavosemiquinone and tyrosine radical in photoreaction of a blue light sensor BLUF protein TePixD, Biochemistry 47, 12574-12582.

[31] Masuda, S., Hasegawa, K., Ishii, A. and Ono, T. (2004) Light-induced structural changes in a putative blue-light receptor with a novel FAD binding fold sensor of blue-light using FAD (BLUF); Slr1694 of Synechocystis sp PCC6803, Biochemistry 43, 5304-5313.

[32] Berthold, D.A., Babcock, G.T. and Yocum, C.F. (1981) A highly resolved, oxygen-evolving photosystem II preparation from spinach thylakoid membranes: EPR and electron-transport properties, FEBS Lett. 134, 231-234.

[33] Ono, T. and Inoue, Y. (1986) Effects of removal and reconstitution of the extrinsic 33, 24 and

16 kDa proteins on flash oxygen yield in photosystem II particles, Biochim. Biophys. Acta 850, 380-389.

[34] Mims, W.B. (1972) Envelope modulation in spin-echo experiments, Phys. Rev. B 5, 2409-2419.

[35] Bleaney, B. and Bowers, K.D. (1952) Anomalous paramagnetism of copper acetate, Proc. R. Soc. Lond. A Math. phys. sci. 214, 451-465.

[36] Coffman, R.E. and Buettner, G.R. (1979) Limit function for long-range ferromagnetic and anti-ferromagnetic superexchange, J. Phys. Chem. 83, 2387-2392.

[37] Eaton, S.S. and Eaton, G.R. (2000) Distance Measurements in Biological Systems by EPR (Berliner, L.J., Eaton, S.S., Eaton, G.R., Eds.), pp. 29-154, Kluwer, New York.

[38] Orbach, R. (1961) Spin-lattice relaxation in rare-earth salts, Proc. R. Soc. Lond. A Math. phys. sci. 264, 458-484.

[39] Orbach, R. (1961) Spin-lattice telaxation in tare-rarth dalts: Field dependence of 2-phonon process, Proc. R. Soc. Lond. A Math. phys. sci. 264, 485-495.

[40] Van Vleck, J.H. (1940) Paramagnetic relaxation times for titanium and chrome alum, Phys. Rev. 57, 426-447.

[41] Shultz, D.A., Boal, A.K. and Farmer, G.T. (1997) The biradical, bis(3,5-di-tert-butyl-4-phenoxyl)methyleneadamantane, exhibits matrix-dependent EPR spectra suggesting rotamer bistability with differential exchange coupling, J. Am. Chem. Soc. 119, 3846-3847.

[42] Wautelet, P., Le Moigne, J., Videva, V. and Turek, P. (2003) Spin exchange interaction through phenylene-ethynylene bridge in diradicals based on iminonitroxide and nitronylnitroxide radical derivatives. 1. Experimental investigation of the through-bond spin exchange coupling, J. Org. Chem. 68, 8025-8036.

[43] Shultz, D.A., Mussari, C.P., Ramanathan, K.K. and Kampf, J.W. (2006) Electron spin-spin exchange coupling mediated by the porphyrin pi system, Inorg. Chem. 45, 5752-5759.

[44] Okazawa, A. and Ishida, T. (2009) Super-superexchange coupling through a hydrogen bond in a linear copper(II) complex, [Cu(LH)(L)]· BF4· $2H_2O$ (LH = N-tert-butyl-N-2-pyridylhydroxy lamine), Chem. Phys. Lett. 480, 198-202.

Pulsed EPR analysis of the photo-induced triplet radical pair in the BLUF protein SyPixD: Determination of the protein-protein distance and orientation in the oligomeric protein

Introduction

Photoreceptor proteins have important roles in the efficient utilization of solar energy because they adapt to environmental light conditions. The photoreceptors absorb specific light energies and induce various physiological responses. The BLUF (a sensor of Blue Light Using Flavin) domain is a newly discovered blue light sensory photoreceptor protein that combines flavin adenine dinucleotide (FAD) chromophore [1]. The five groups of the BLUF domain are physiologically characterized at present as the followings: PixD (SyPixD and TePixD in cyanobacteria *Synechocystis* sp. PCC6803 and *Thermosynechococcus elongatus,* respectively), AppA and BlrB in purple photosynthetic bacterium *Rhodobacter sphaeroides* [1-3], PAC in *Euglena gracilis* [4], YcgF in *Escherichia coli* [5], and PapB in *Rhodopseudomonas palustris* [6]. PixD regulates pili-dependent cell motility [7], AppA controls the expression of the photosynthesis gene [8], PAC regulates the photophobic reaction [4,9], and YcgF and PapB control the biofilm formation [6,10]. A mutant without the gene encoding the PixD protein was characterized by phototaxis of cells with extraordinary movement in response to blue light [7].

The structures of SyPixD were determined by X-ray crystallography and NMR spectroscopy [8]. Figure 1A shows the crystal structure of SyPixD oligomer, which has a decameric structure formed of a pair of pentameric SyPixD rings. Figure 1B shows the protein structure around the flavin molecule within each SyPixD monomer, and Figure 1C shows the molecular structures of flavin and tyrosine. The Gln and Asn residues around the flavin molecule are highly conserved in the BLUF proteins. The flavin molecule is ligated to these adjacent residues through H-bonds.

All BLUF proteins exhibit reversible 10-20 nm photo-induced red-shifts of the flavin absorption bands at room temperature, and the red-shifted form (referred to as the *F*-state) reverts back to the dark-adapted form (the *D*-state) within 10-30 min [2,3,7,11-13]. Fourier transform infrared (FTIR) and Raman spectroscopic studies suggested that an H-bond of the C_4=O group in the flavin isoalloxazine ring is strengthened in the red-shifted form [11,14-21]. Replacement of Gln50 by Ala does not induce the red-shifted form, indicating that the H-bond formed in the *D* state between N5 in flavin and Gln50 changes in the photo-conversion reaction [22]. Another mutant in which Asn31 and Asn32 were replaced by Ala produced the normal red-shifted form, suggesting that the H-bonds with

the Asn residues have no direct influence on photo-conversion [23]. Tyr8 is also assumed to form an H-bond with FAD via Gln50 residue, although it is not directly connected to FAD [23]. An FTIR study proposed that Tyr8 functions as a H-bond donor to Gln50 in both the *D*- and *F*-states [24]. Mutants in which the corresponding tyrosine residues adjacent to flavin were replaced by phenylalanine in the BLUF proteins (Y8F in TePixD and SyPixD, Y21F in AppA, and Y472F in PACα-F2) exhibited no photo-conversion activity at physiological temperatures [9,15,25-28].

Laser excitation induced the red-shifted form within 100 ps at room temperature in BLUF proteins, followed by a decay of the singlet excited state [29-32]. Transient absorption measurements showed that electron transfer from Tyr8 to the photoexcited flavin occurred with time constants of 7, 40 and 180 ps in SyPixD, when a FAD anion radical ($FAD^{\bullet-}$) and a subsequent neutral radical ($FADH^{\bullet}$) were formed [30]. It was suggested that the charge separation and the subsequent charge recombination between Tyr8 and FAD led to the transformation of the H-bond network around flavin [30]. The H-bond transformations of Tyr8 were observed in the photo-conversion process by FTIR measurement [24]. A similar mechanism was proposed for AppA based on mutant analyses with the Tyr21 and Trp104 mutants [27]. The photo-induced $FADH^{\bullet}$-$Y8^{\bullet}$ radical pair seemed to be essential for the photochemistry and the signaling function of the BLUF proteins.

It is unclear how the photo-induced local transformations around FAD lead to the signaling reaction and the subsequent physiological reactions, including the phototactic movement of cells. Yuan and Bauer showed that PixD forms a large oligomeric structure in the presence of another protein denoted as PixE [33]. They revealed that PixE promotes the oligomerization of PixD from dimers into a stable decamer of a $PixD_{10}$-$PixE_5$ complex under dark condition and that the photo excitation of FAD induces disruption of the complex into PixD dimers and PixE monomers. The photo-degradation was proposed to be a result of the photo-induced H-bond alternation between Trp91 and Met93 associated with conformational changes of the PixD dimer-dimer interface [33]. Transient grating (TG) spectroscopy showed that the conformation of the PixD decamer is altered with a time constant of 4 ms [34]. The photoreaction is regarded as a significant process connecting local changes around FAD and signaling reactions.

Recently, an electron paramagnetic resonance (EPR) signal was observed in TePixD [35]. The spectrum shows a typical Pake doublet arising from magnetic dipole interactions. The signal was trapped stably by illumination of the red-shifted state at 5-150 K. The pulsed electron-nuclear double resonance (ENDOR) studies of both the wild-type and the site-directed mutant of TePixD suggested that the Pake doublet signal was due to a radical pair from the flavin neutral radical ($FADH^{\bullet}$) and an adjacent tyrosine ($Y8^{\bullet}$). We observed a similar Pake doublet EPR signal from an $FADH^{\bullet}$-$Y8^{\bullet}$ radical pair in SyPixD [36]. The exchange coupling *J* between $FADH^{\bullet}$ and $Y8^{\bullet}$ radicals was ferromagnetic

($J > 0$) and was estimated to be $2J = 6 \sim 8$ cm^{-1} based on the temperature dependence of the spin-lattice relaxation time [36].

In this study, pulsed electron-electron double resonance (PELDOR) spectroscopy was applied to determine the protein-protein distance and the relative orientation of SyPixD proteins in the oligomer. The Pake doublet signal from the $FADH^{\bullet}$-$Y8^{\bullet}$ radical pair has been characterized by the $\boldsymbol{S} = 1$ spin state [36], and the radical pair was used as a spin probe in the PELDOR measurement. We demonstrate that PELDOR analysis with orientation selection is a powerful tool for the study of the structure of the supercomplex in the photosensing protein SyPixD.

Materials and methods

Sample preparation

SyPixD (Slr1694) was purified according to the previously reported method, in which the oligomer with the molecular mass corresponding to trimer (or tetramer) was obtained by chitin affinity chromatography [37]. The protein was dissolved in a medium containing 50 mM Tris/HCl and 1 mM NaCl (pH 8.0).

EPR measurements

ESE experiments were performed on a Bruker ESP-380E EPR spectrometer using a two-pulse (primary) ESE sequence. The spectrometer was equipped with a cylindrical dielectric cavity (ER4117DHQ-H, Bruker) and a gas flow temperature-control system (CF935, Oxford Instruments). Microwave pulses with 16 and 24 ns duration were employed for the $\pi/2$ and π pulse sequence, respectively. Field-swept ESE spectra were measured by the $\pi/2–\tau–\pi–$echo sequence with a time interval τ of 200 ns between the microwave pulses. Spin-lattice relaxation time was measured by inversion recovery for the $\pi–T–\pi/2–\tau–\pi–$echo pulse sequence with a time interval τ of 200 ns. PELDOR spectra were measured by the $\pi/2–\tau–\pi–$echo pulse sequence with a time interval τ of 1600 ns, with scanning of another pump π pulse between the first and second pulses.

Samples were illuminated using light from a 408 nm diode laser (ITC 510, Thorlabs) through a 1 mm diameter glass fiber.

Results and discussion

Pake doublet in SyPixD

Figure 2 shows the primary ESE field-swept EPR signal at 10 K in SyPixD. The SyPixD was pre-illuminated at 150 K for 30 min and then cooled down to 50 K under illumination. The detected EPR signal exhibits large inner peaks separated by 7.5 mT and small outer peaks separated by 15 mT, which were characterized by a magnetic dipole-dipole interaction, typical for a Pake doublet. A similar Pake doublet signal was observed in the analogous BLUF protein TePixD from *Thermosynechococcus elongatus* in which the inner and outer peaks were separated by 8.5 and 17 mT, respectively [35]. Pulsed ENDOR studies in TePixD and the variant of Tyr8 suggested that the dipole-dipole interaction was caused by a $FADH^{\bullet}$-$Y8^{\bullet}$ radical pair [35]. The dotted line in Fig. 2 shows a simulated spectrum based on the molecular coordinates of FAD and Tyr8 in the crystal structure of SyPixD [8] and spin distributions for these molecules [35]. It was simulated by the summation of electron dipole-dipole interactions between spins on each atom of the FAD and Tyr8 molecules. The exchange coupling J, estimated as J = 3-4 cm^{-1}, is much larger than the dipole-dipole interaction, and therefore was neglected for the simulation [36] The g-values for both molecules were assumed to be g = 2, and the stick spectra using a 2.5 mT Gaussian line width were convoluted. The agreement of the simulated and experimental spectra suggested that the Pake doublet signal was assigned to the $FADH^{\bullet}$-$Y8^{\bullet}$ radical pair with the same arrangements as in the crystal structure of SyPixD. The slightly different peak separation in the Pake doublet signal in TePixD was interpreted as a minor difference in the protein structure [35]. The H_1-dependence of the ESE-signal amplitude of the Pake doublet signal showed that the signal is characterized by a complete $\boldsymbol{S}$ = 1 spin [36].

PELDOR analysis of protein-protein distance and relative orientation in the SyPixD oligomer

The $FADH^{\bullet}$-$Y8^{\bullet}$ radical pair is stabilized at low temperature and forms a complete triplet spin state of $\boldsymbol{S}$ = 1, connecting with two $\boldsymbol{S}$ = 1/2 spins via the strong exchange interaction [36]. As each SyPixD monomer contains one radical pair, the radical pair is useful as a spin probe tightly fixed to the protein. Figure 3 shows PELDOR spectra obtained for the Pake doublet signal in the PixD oligomer after subtracting the background signal. Microwave frequencies of the probe (black triangles, *inset*) and pump (white triangles, *inset*) pulses were adjusted to the maximum peak at a lower magnetic field, as well as at (A) another maximum peak and (B) an outer peak at a lower magnetic field, respectively. Panels A and B show a significantly different oscillation pattern. The PELDOR signal is strictly ruled by orientation selection against the external field $\boldsymbol{H}$ because the Pake doublet signal consists of a magnetic dipole-dipole interaction as an anisotropic interaction.

Therefore, the PELDOR with orientation selection provides insights into not only distance but also relative molecular orientation between radicals.

As the structure of the SyPixD complex in the sample is unknown, we calculated the PELDOR spectra based on the crystal structure of the decameric SyPixD. The size of the monomeric SyPixD is approximately 40 Å. Therefore, we can focus only on the interaction between the Pake doublet in one SyPixD and an adjacent SyPixD because the effective distance for PELDOR detection can be within approximately 50 Å. Figure 4A shows the relative arrangement of $FADH^{\bullet}$-$Y8^{\bullet}$ radical pairs, which were defined as vectors connecting $FADH^{\bullet}$ and $Y8^{\bullet}$ radicals, in four adjacent monomers, labeled by α, β, γ, and χ in a SyPixD decamer, as shown in Fig. 1A. We assumed that the SyPixD oligomer is formed by a combination of pairs of the adjacent monomers (α-β, α–γ, or α–χ pairs).

Figure 4B defines the vectors $\boldsymbol{S_d}$ and $\boldsymbol{S_p}$ for the radical pairs and the vector $\boldsymbol{R}$ connecting $\boldsymbol{S_d}$ and $\boldsymbol{S_p}$. The angles θ_d, θ_p and θ_H are defined as the angles of the vectors $\boldsymbol{S_d}$, $\boldsymbol{S_p}$ and $\boldsymbol{R}$ relative to the external magnetic field $\boldsymbol{H}$, respectively. Each possible pair contains a couple of spin vectors with different arrangements, leading to different magnetic dipole interactions, in which exchange interactions are negligible due to the long distances [38]. The magnetic dipole interaction D_R between radical pairs ($\boldsymbol{S_d}$ and $\boldsymbol{S_p}$) on different proteins is expressed by the following equation:

$$D_R = \frac{3}{2}\frac{g_1 g_2 \beta^2}{R^3}\left(1-3\cos^2\theta_H\right)\sqrt{S(S+1)} \quad , \qquad (1)$$

where g_1 and g_2 are the g-factors for each spin, β is the Bohr magneton, R is the distance between radical pairs ($\boldsymbol{S_d}$ and $\boldsymbol{S_p}$), and $\sqrt{S(S+1)}$ is the spin magnitude. D_R depends on an angle θ_H between $\boldsymbol{H}$ and the vector $\boldsymbol{R}$ connecting $\boldsymbol{S_d}$ and $\boldsymbol{S_p}$ (Fig. 4B). A pump pulse used in the PELDOR measurement induces a flip-flop of one spin in the interacting spin pair and leads to a change of the local magnetic field at the position of its partner spin via the magnetic dipole interaction D_R. As a result, the primary ESE signal observed with the π/2–τ–π–echo pulse sequence is perturbed, and its amplitude oscillates with the pump pulse as it scans between the first and second probe pulses. The oscillation of the echo amplitude $V(\tau,\tau')$ is characterized by the following equation [39,40]:

$$V(\tau,\tau') \propto 1-p\left[1-\cos\left(D_R\tau'\right)\right] \quad , \qquad (2)$$

where p is the excitation probability for the pump pulse and τ' is a time interval between the first π/2 probe and the pump pulses.

The angles θ_d, θ_p were determined by the each microwave frequency at the resonant external field $\boldsymbol{H}$ because of orientation selection in the anisotropic spectrum. Therefore, the angle θ_H between the external field vector $\boldsymbol{H}$ and $\boldsymbol{R}$ is determined as the intersections of the generators in two cones with

defined as the obliquity θ_d, θ_p with different axis. One or two intersections are obtained depending on the conditions. Two intersections exhibit the same angle θ_H, and therefore the angle θ_H is uniquely determined. If there is no intersection, the conditions should be ruled out. Thus we evaluated θ_H based on the experimental angles θ_d and θ_p.

The PELDOR signal in Fig. 3A was observed at the resonance magnetic fields fixed to two maximum peaks of the Pake doublet signal, indicating that both spin vectors $\boldsymbol{S_d}$ and $\boldsymbol{S_p}$ were almost perpendicular to the external field vector $\boldsymbol{H}$ ($\theta_d = \theta_p = 90^o$). In this condition, we obtained the angle sets of (θ_d, θ_p, θ_H) = (90^o, 90^o, 42^o), (90^o, 90^o, 55^o) and (90^o, 90^o, 78^o) and the distance R = 21.9, 42.5, and 46.0 Å for the α–β, α–γ, and α–χ pairs in Fig. 4A, respectively. The pulse width with 24 ns was calculated as the magnetic field width of 1.5 mT in the spectrum. It was represented by a Gaussian function with the angular distribution width of 5-12^o depending on θ_p. Figure 5 shows simulated PELDOR spectra based on the arrangements of spin vectors in the (a) α–β, (b) α–γ, or (c) α–χ pairs, in which the angular distribution was calculated by a Gaussian function with a distribution width of 12^o. Traces *a-c* in Panel A show simulated spectra for the PELDOR signal measured at maximum peak positions of the Pake doublet signal for both the pump and the prove pulses (Fig. 3A). The simulated signal for the α–γ pair coincides with the experimental signal (gray line), while oscillations shown in the signals for the α–β and α–χ pairs exhibit higher frequencies. In the situation, the condition of $\theta_d/\theta_p = 35^o$ could also be included because of the overlapping on the spectrum. However, the condition did not reproduce the experimental result (data not shown).

Fig. 3B was observed with the probe and pump pulses producing resonances at the inner maximum and the outer peak of the Pake doublet signal, respectively. The probe pulse is expected to induce a flip-flop of the spin vector in a direction of about $\theta_d = 90^o$ or 35^o against the external field $\boldsymbol{H}$, while the pump pulse excites the spin vector at around $\theta_p = 0^o$. We estimated valid angles of θ_d and θ_p within the field width defined as the orientation distribution. For α–β and α–γ pairs, the angle sets were estimated to be (θ_d, θ_p, θ_H) = (75^o, 20^o, 120^o) and (41^o, 16^o, 116^o), respectively. For the α–χ pair, no suitable set of angles was obtained. When the angle was assumed to be $\theta_d = 22^o$, an angle set of (θ_d, θ_p, θ_H) = (22^o, 20^o, 150^o) was tentatively estimated. Traces *a-c* (Fig. 5B) show the simulated spectra with the angle sets and the inter-spin distances for pairs of α–β, α–γ, and α–χ, respectively, in which the angular distribution was represented by a Gaussian function with a distribution width of 5^o. Only the α–γ pair reproduces the oscillation in the experimental PELDOR signal (gray line), which is consistent with the results from the simulation in Fig. 5A. The possibility that the rapid oscillation for the α–β pair was undetectable with slightly modified structure was not excluded. At the moment, however, we can indicate the relative arrangement of α–γ pair of SyPixD in the oligomer by the PELDOR measurement.

It is unclear how the conformation of the PixD oligomer changes during the sensoring photoreaction. TG spectroscopy showed photo-induced dynamic conformational changes of PixD [34]. The PixD decamer is made of two pentameric rings (Fig. 1A). Stoichiometric analysis with chromatography and Gibbs free energy calculations suggested that the PixD decamer was photo-degraded into dimers made of the α–β pair [33]. The photo-degradation is expected to lead to the signaling reaction. As shown in this report, the PELDOR measurement is possible to trace the specific pair in the PixD oligomer. By applying the PELDOR method to the PixD decamer before and after light illumination (photo-degradation), the dynamic conformational change of the PixD protein oligomer would be clarified.

Conclusion

The photo-induced radical pair of $FADH^{\bullet}$ and $Y8^{\bullet}$ in a BLUF protein, SyPixD, was studied by pulsed EPR spectroscopy. The $\boldsymbol{S} = 1$ radical pair was utilized as a spin marker to analyze the oligomeric structure of the PixD, in which the large anisotropy of the Pake doublet signal allowed for the orientation-selective excitation of the spin vector of the radical pair. In this study, we demonstrated that the oligomeric structure of PixD is determined by PELDOR spectroscopy. With the orientation-selective excitation of the radical pair, it was possible to estimate not only inter-protein distance but also relative orientation. PELDOR measurement can be useful for analysis of the conformational change of the PixD decamer in the photo-degradation process and for elucidation of the signaling reaction in PixD.

Figures

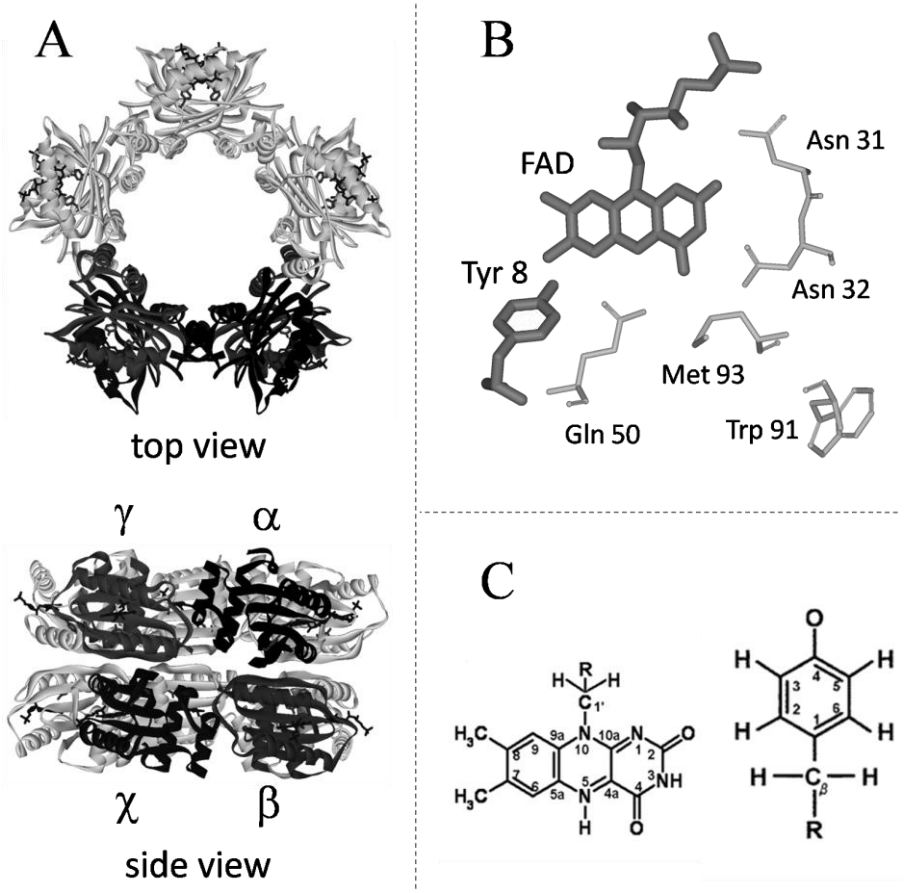

Figure 1: (A). Top view (upper) and side view (lower) of the x-ray crystal structure of the SyPixD decamer (PDB entry 2HFO). The four adjacent monomers in black are labeled by α, β, γ, and χ, respectively. (B). The local structure of FAD and surrounding residues in SyPixD (chain A defined in PDB entry 2HFO). (C). Molecular structures of neutral flavinosemiquinone (FADH) (left) and tyrosine (right).

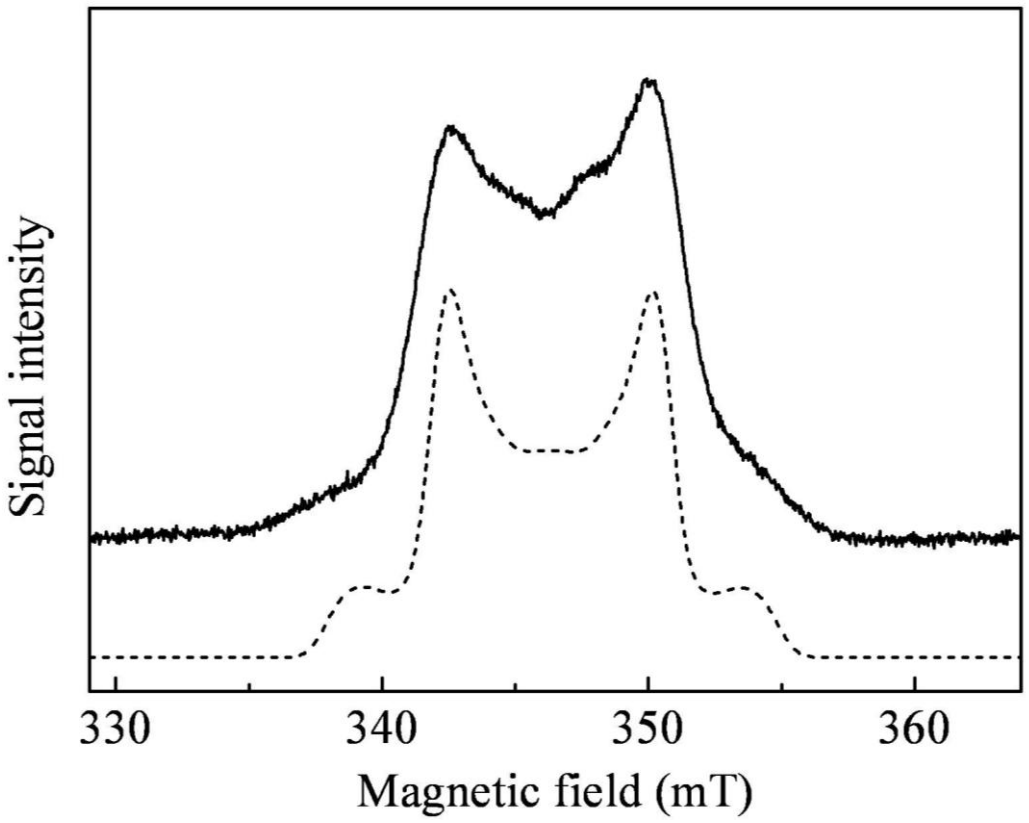

Figure 2: Primary ESE field-swept EPR spectra of SyPixD. The sample was pre-illuminated at 150 K and subsequently cooled down to 50 K during illumination. The dotted line represents a simulated spectrum based on the crystal structure of SyPixD [8] and spin distributions for flavin and tyrosine molecules [35]. Stick spectra using a 2.5 mT Gaussian line width were convoluted to obtain the simulated powder spectrum. Experimental conditions: microwave frequency, 9.66 GHz; duration of the microwave pulses, 16 and 24 ns; repetition rate, 0.1 kHz; temperature, 10 K. The interval time, τ, between the first and second pulse was 400 ns.

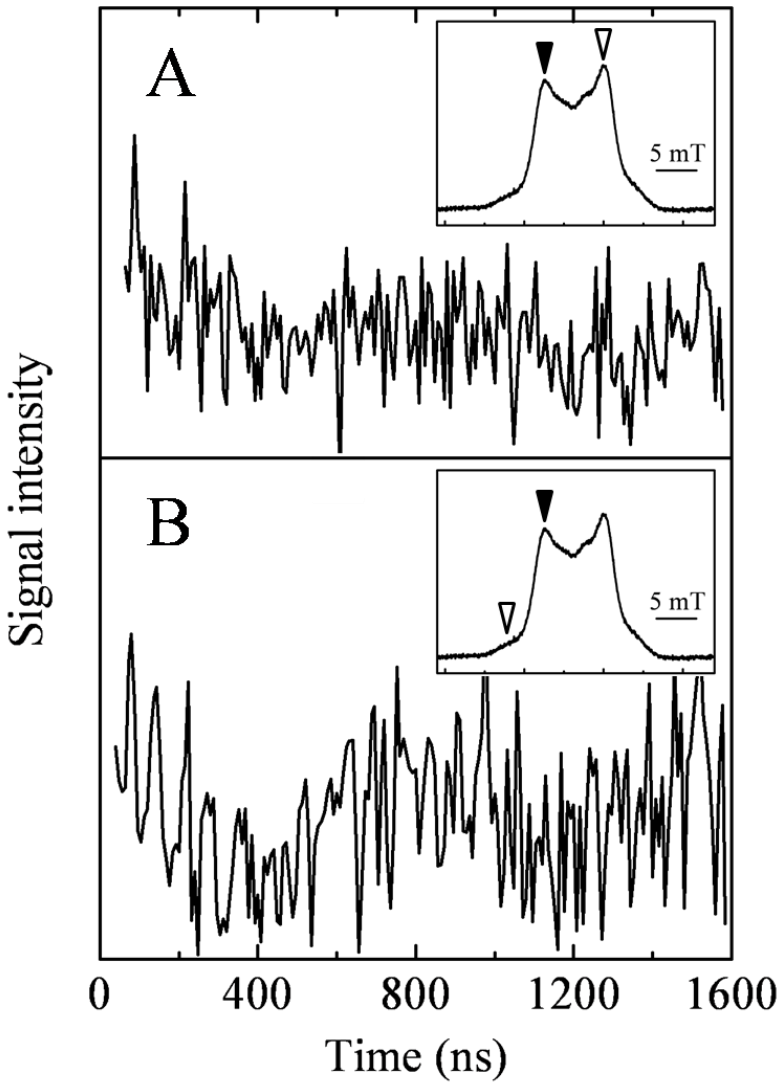

Figure 3: PELDOR spectra in the Pake doublet signal in the SyPixD oligomer. The spectra were recorded at 342.2 mT with a pulse at 9.657 GHz for detection, and at (A) 9.451 and (B) 9.786 GHz for pumping. The *insets* show the resonance frequencies in the Pake doublet signal for the primary ESE and the pump pulse, indicated by black and white triangles, respectively. The detection pulse excites the spin vector $\boldsymbol{S_d}$, connecting FADH$^{\bullet}$ and Tyr8$^{\bullet}$, in a direction of around θ_d = 90^{o} or 35^{o} against the external field $\boldsymbol{H}$. The pump pulse excites the spin vector $\boldsymbol{S_p}$ at around (A) θ_p = 90^{o} or 35^{o} and (B) θ_p = 0^{o} against the external field $\boldsymbol{H}$. Experimental conditions: duration of the microwave pulses, 16, 24, and 24 ns; repetition rate, 0.1 kHz; temperature, 10 K. The interval time, τ, between the first and third pulse was 1600 ns.

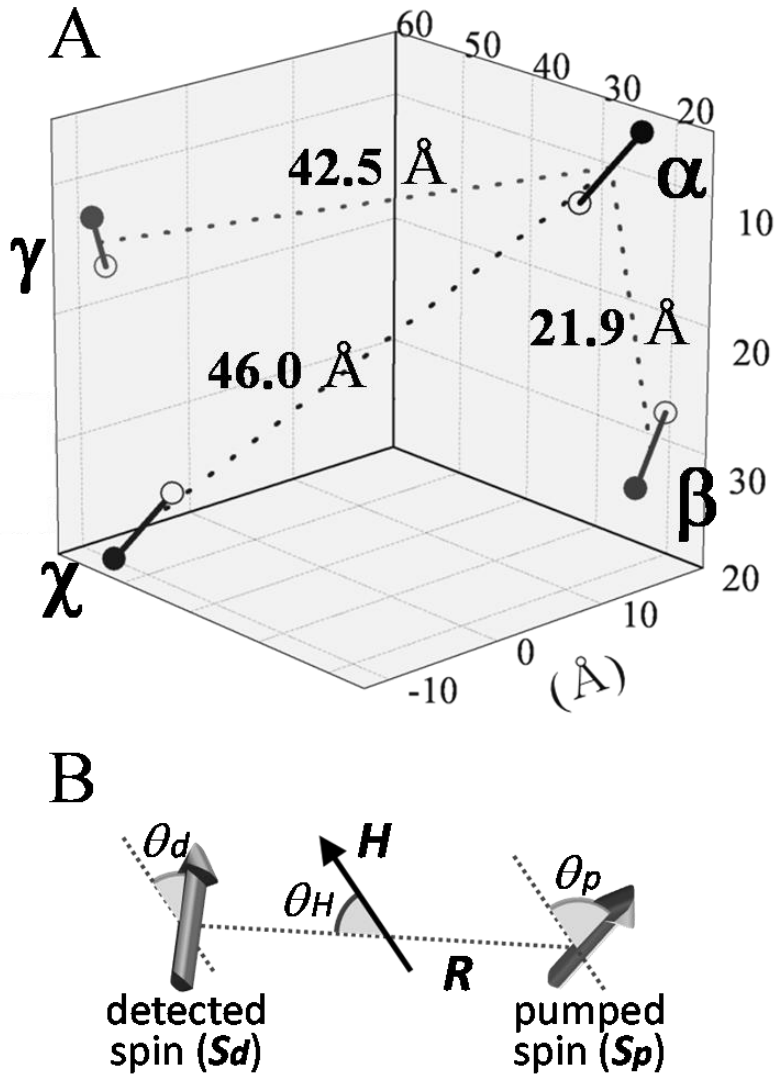

Figure 4: (A). Relative arrangement of adjacent pairs of flavin and tyrosine molecules in a SyPixD decamer, in which each monomer is labeled by α, β, γ, and χ as in Fig. 1A. The black and white circles represent weighted centers of spin distribution of flavin and tyrosine molecules, respectively, estimated based on the spin distribution in ref. [35]. The vector joining the weighted center of flavin to that of tyrosine was interpreted as one spin vector with a spin state of $\boldsymbol{S} = 1$. The relative arrangement and the distance were obtained based on the crystal structure [8] in which the distance was defined as that between the centers of the spin vectors. (B). Definition of angles of the external magnetic field $\boldsymbol{H}$ with respect to the spin vectors (θ_d, θ_p) or the vector $\boldsymbol{R}$ connecting radical pairs (θ_H).

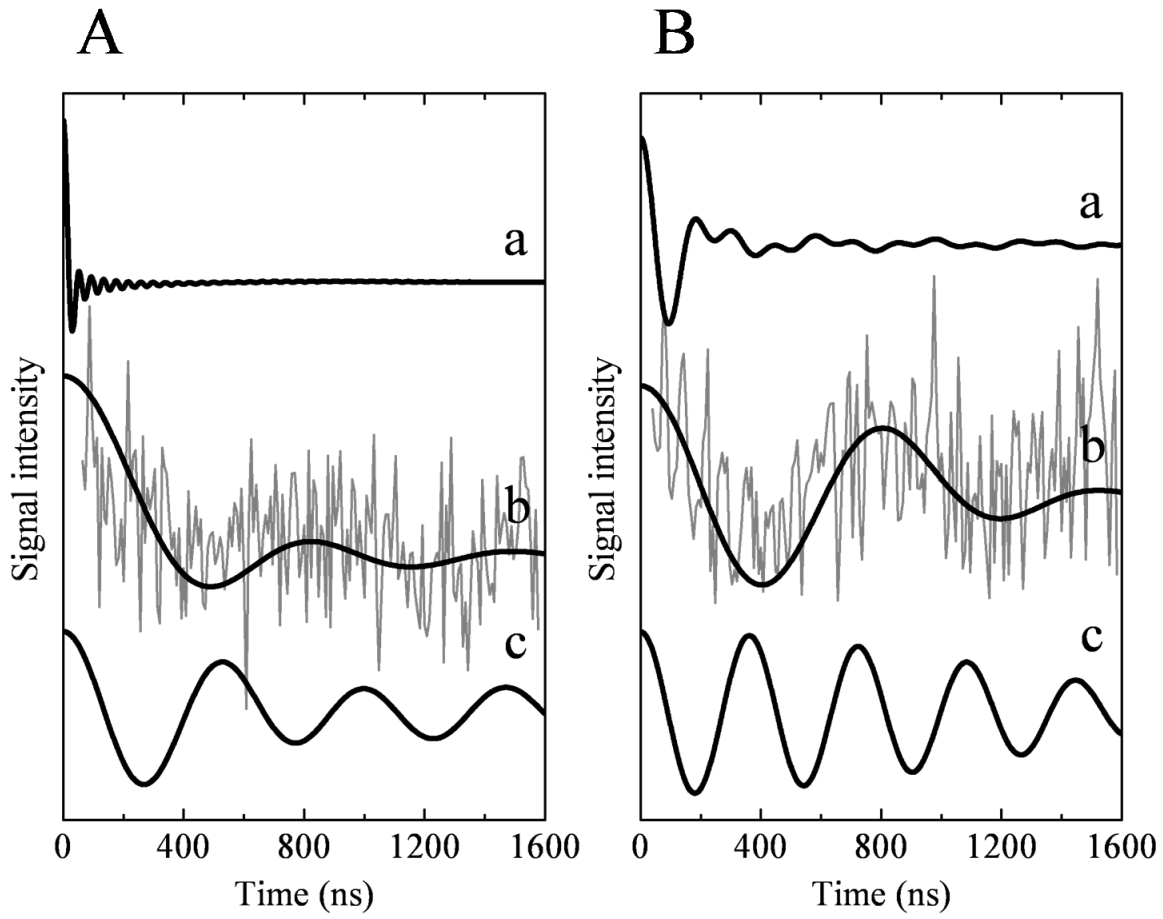

Figure 5: Simulated PELDOR spectra (black lines) with experimental ones (gray lines) in (A) Fig. 3A and (B) Fig. 3B. The spectra were simulated based on the assumption that the SyPixD oligomer was made of a pair of (a) α and β, (b) α and γ, or (c) α and χ monomers. The label for each SyPixD monomer is the same as in Fig. 1A and Fig. 4A. The traces *a*, *b*, and *c* in Panel A were simulated with an angle set of (θ_d, θ_p, θ_H) = (90°, 90°, 42°), (90°, 90°, 55°), and (90°, 90°, 78°), respectively, and the traces *a*, *b*, and *c* in Panel B with (75°, 20°, 120°), (41°, 16°, 116°), and (22°, 20°, 150°), respectively. The angular distribution was represented by the Gaussian function with a distribution width of 12° (A) and 5° (B).

References

[1] Gomelsky, M. and Klug, G. (2002) BLUF: a novel FAD-binding domain involved in sensory transduction in microorganisms, Trends Biochem. Sci. 27, 497-500.

[2] Masuda, S. and Bauer, C.E. (2002) AppA is a blue light photoreceptor that antirepresses photosynthesis gene expression in *Rhodobacter sphaeroides*, Cell 110, 613-623.

[3] Jung, A., Domratcheva, T., Tarutina, M., Wu, Q., Ko, W.H., Shoeman, R.L., Gomelsky, M., Gardner, K.H., and Schlichting, I. (2005) Structure of a bacterial BLUF photoreceptor: Insights into blue light-mediated signal transduction, Proc. Natl. Acad. Sci. USA 102, 12350-12355.

[4] Iseki, M., Matsunaga, S., Murakamik, A., Ohno, K., Shiga, K., Yoshida, K., Sugai, M., TakahashiI, T., Hori, T., and Watanabe, M. (2002) A blue-light-activated adenylyl cyclase mediates photoavoidance in *Euglena gracilis*, Nature 415, 1047-1051.

[5] Rajagopal, S., Key, J.M., Purcell, E.B., Boerema, D.J. and Moffat, K. (2004) Purification and initial characterization of a putative blue light-regulated phosphodiesterase from *Escherichia coli*, Photochem. Photobiol. 80, 542-547.

[6] Kanazawa, T., Ren, S., Maekawa, M., Hasegawa, K., Arisaka, F., Hyodo, M., Hayakawa, Y., Ohta, H., Masuda, S. (2010) Biochemical and physiological characterization of a BLUF protein-EAL protein complex involved in blue light-dependent degradation of cyclic diguanylate in the purple bacterium *Rhodopseudomonas palustris*, Biochemistry 49, 10647-10655.

[7] Okajima, K., Yoshihara, S., Fukushima, Y., Geng, X., Katayama, M., Higashi, S., Watanabe, M., Sato, S., Tabata, S., Shibata, Y., Itoh, S., and Ikeuchi, M. (2005) Biochemical and functional characterization of BLUF-type flavin-binding proteins of two species of cyanobacteria, J. Biochem. 137, 741-750.

[8] Yuan, H., Anderson, S., Masuda, S., Dragnea, V., Moffat, K. and Bauer, C. (2006) Crystal structures of the *Synechocystis* photoreceptor Slr1694 reveal distinct structural states related to signaling, Biochemistry 45, 12687-12694.

[9] Ito, S., Murakami, A., Sato, K., Nishina, Y., Shiga, K., Takahashi, T., Higashi, S., Iseki, M., Watanabe, M. (2005) Photocycle features of heterologously expressed and assembled eukaryotic flavin-binding BLUF domains of photoactivated adenylyl cyclase (PAC), a blue-light receptor in Euglena gracilis, Photoch. Photobio. Sci. 4, 762-769.

[10] Tschowri, N., Busse, S. and Hengge, R. (2009) The BLUF-EAL protein YcgF acts as a direct anti-repressor in a blue-light response of *Escherichia coli*, Genes Dev. 23, 522-534.

[11] Laan, W., van der Horst, M.A., van Stokkum, I.H. and Hellingwerf, K.J. (2003) Initial

characterization of the primary photochemistry of AppA, a blue-light-using flavin adenine dinucleotide-domain containing transcriptional antirepressor protein from *Rhodobacter sphaeroides*: A key role for reversible intramolecular proton transfer from the flavin adenine dinucleotide chromophore to a conserved tyrosine?, Photochem. Photobiol. 78, 290-297.

[12] Fukushima, Y., Okajima, K., Shibata, Y., Ikeuchi, M. and Itoh, S. (2005) Primary intermediate in the photocycle of a blue-light sensory blue-light FAD-protein, Tll0078, of *Thermosynechococcus elongatus* BP-1, Biochemistry 44, 5149-5158.

[13] Zirak, P., Penzkofer, A., Schiereis, T., Hegemann, P., Jung, A. and Schlichting, I. (2006) Photodynamics of the small BLUF protein BlrB from *Rhodobacter sphaeroides*, J. Photochem. Photobiol., B 83, 180-194.

[14] Hasegawa, K., Masuda, S. and Ono, T. (2004) Structural intermediate in the photocycle of a BLUF (sensor of blue light using FAD) protein Slr1694 in a cyanobacterium *Synechocystis* sp PCC6803, Biochemistry 43, 14979-14986.

[15] Hasegawa, K., Masuda, S. and Ono, T.A. (2005) Spectroscopic analysis of the dark relaxation process of a photocycle in a sensor of blue light using FAD (BLUF) protein Slr1694 of the cyanobacterium *Synechocystis* sp PCC6803, Plant Cell Physiol. 46, 136-146.

[16] Hasegawa, K., Masuda, S. and Ono, T. (2006) Light induced structural changes of a full-length protein and its BLUF domain in YcgF(Blrp), a blue-light sensing protein that uses FAD (BLUF), Biochemistry 45, 3785-3793.

[17] Masuda, S., Hasegawa, K. and Ono, T. (2005) Adenosine diphosphate moiety does not participate in structural changes for the signaling state in the sensor of blue-light using FAD domain of AppA, FEBS Lett. 579, 4329-4332.

[18] Masuda, S., Hasegawa, K. and Ono, T. (2005) Light-induced structural changes of apoprotein and chromophore in the sensor of blue light using FAD (BLUF) domain of AppA for a signaling state, Biochemistry 44, 1215-1224.

[19] Masuda, S., Hasegawa, K. and Ono, T. (2005) Tryptophan at position 104 is involved in transforming light signal into changes of beta-sheet structure for the signaling state in the BLUF domain of AppA, Plant Cell Physiol. 46, 1894-1901.

[20] Unno, M., Masuda, S., Ono, T.A. and Yamauchi, S. (2006) Orientation of a key glutamine residue in the BLUF domain from AppA revealed by mutagenesis, spectroscopy, and quantum chemical calculations, J. Am. Chem. Soc. 128, 5638-5639.

[21] Unno, M., Sano, R., Masuda, S., Ono, T.A. and Yamauchi, S. (2005) Light-induced structural changes in the active site of the BLUF domain in AppA by Raman spectroscopy, J. Phys. Chem. B 109, 12620-12626.

[22] Grinstead, J.S., Hsu, S.T.D., Laan, W., Bonvin, A.M.J.J., Hellingwerf, K.J., Boelens, R. and

Kaptein, R. (2006) The solution structure of the AppA BLUF domain: Insight into the mechanism of light-induced signaling, Chembiochem 7, 187-193.

[23] Kita, A., Okajima, K., Morimoto, Y., Ikeuchi, M. and Miki, K. (2005) Structure of a cyanobacterial BLUF protein, Tll0078, containing a novel FAD-binding blue light sensor domain, J. Mol. Biol. 349, 1-9.

[24] Takahashi, R., Okajima, K., Suzuki, H., Nakamura, H., Ikeuchi, M. and Noguchi, T. (2007) FTIR study on the hydrogen bond structure of a key tyrosine residue in the flavin-binding blue light sensor TePixD from *Thermosynechococcus elongatus*, Biochemistry 46, 6459-6467.

[25] Okajima, K., Fukushima, Y., Suzuki, H., Kita, A., Ochiai, Y., Katayama, M., Shibata, Y., Miki, K., Noguchi, T., Itoh, S., and Ikeuchi, M. (2006) Fate determination of the flavin photoreceptions in the cyanobacterial blue light receptor TePixD (T110078), J. Mol. Biol. 363, 10-18.

[26] Dragnia, V., Anderson, S., Masuda, S., Waegelle, M., Balascuta, S., Ybe, J., Dragnea, B., Moffat, K., Bauer, C. (2005) Crystallographic and functional studies of the AppA blue-light receptor BLUF domain from *Rhodobacter sphaeroides*, Abstr. Pap. Am. Chem. Soc. 230, U2809.

[27] Gauden, M., van Stokkum, I. H. M., Key, J. M., Luhrs, D. C., Van Grondelle, R., Hegemann, P., Kennis, J. T. M. (2007) On the role of aromatic side chains in the photoactivation of BLUF domains, Biochemistry 46, 7405-7415.

[28] Kraft, B.J., Masuda, S., Kikuchi, J., Dragnea, V., Tollin, G., Zaleski, J.M. and Bauer, C.E. (2003) Spectroscopic and mutational analysis of the blue-light photoreceptor AppA: A novel photocycle involving flavin stacking with an aromatic amino acid, Biochemistry 42, 6726-6734.

[29] Anderson, S., Dragnea, V., Masuda, S., Ybe, J., Moffat, K. and Bauer, C. (2005) Structure of a novel photoreceptor, the BLUF domain of AppA from Rhodobacter sphaeroides, Biochemistry 44, 7998-8005.

[30] Gauden, M., van Stokkum, I.H.M., Key, J.M., Luhrs, D.C., Van Grondelle, R., Hegemann, P. and Kennis, J.T.M. (2006) Hydrogen-bond switching through a radical pair mechanism in a flavin-binding photoreceptor, Proc. Natl. Acad. Sci. USA 103, 10895-10900.

[31] Gauden, M., Yeremenko, S., Laan, W., van Stokkum, I.H.M., Ihalainen, J.A., van Grondelle, R., Hellingwerf, K.J. and Kennis, J.T.M. (2005) Photocycle of the flavin-binding photoreceptor AppA, a bacterial transcriptional antirepressor of photosynthesis genes, Biochemistry 44, 3653-3662.

[32] Laan, W., Gauden, M., Yeremenko, S., van Grondelle, R., Kennis, J.T.M. and Hellingwerf, K.J. (2005) On the mechanism of activation of the BLUF domain of AppA, Biochemistry 45,

51-60.

[33] Yuan, H. and Bauer, C.E. (2008) PixE promotes dark oligomerization of the BLUF photoreceptor PixD, Proc. Natl. Acad. Sci. USA 105, 11715-11719.

[34] Tanaka, K., Nakasone, Y., Okajima, K., Ikeuchi, M., Tokutomi, S. and Terazima, M. (2009) Oligomeric-state-dependent conformational change of the BLUF protein TePixD (Tll0078), J. Mol. Biol. 386, 1290-300.

[35] Nagai, H., Fukushima, Y., Okajima, K., Ikeuchi, M. and Mino, H. (2008) Formation of interacting spins on flavosemiquinone and tyrosine radical in photoreaction of a blue light sensor BLUF protein TePixD, Biochemistry 47, 12574-12582.

[36] Kondo, T., Masuda, S., Tsutsui, K. and Mino, H. (2011) Temperature dependence of relaxation time of a stable radical pair in SyPixD investigated by pulsed EPR, Chem. Phys. Lett. 501, 528–533.

[37] Masuda, S., Hasegawa, K., Ishii, A. and Ono, T. (2004) Light-induced structural changes in a putative blue-light receptor with a novel FAD binding fold sensor of blue-light using FAD (BLUF); Slr1694 of *Synechocystis* sp PCC6803, Biochemistry 43, 5304-5313.

[38] Coffman, R.E. and Buettner, G.R. (1979) Limit function for long-range ferromagnetic and anti-ferromagnetic superexchange, J. Phys. Chem. 83, 2387-2392.

[39] Milov, A.D., Ponomarev, A.B. and Tsvetkov, Y.D. (1984) Electron electron double-resonance in electron-spin echo: Model biradical systems and the sensitized photolysis of decalin, Chem. Phys. Lett. 110, 67-72.

[40] Milov, A.D., Maryasov, A.G. and Tsvetkov, Y.D. (1998) Pulsed electron double resonance (PELDOR) and its applications in free-radicals research, Appl. Magn. Reson. 15, 107-143.

Chapter II

Enzymatic reaction in dark-operative (light-independent) protochlorophyllide oxidoreductase, DPOR

Chapter introduction

Photosynthetic pigments

In primary reaction of photosynthesis, light energy is captured by photosynthetic pigments, and is carried to reaction center (RC) with exciton transfer process via protein-bound pigments. The excitation energy causes charge separation of a pigment in RC, followed by sequential electron transfer. All the photosynthetic organisms contain various pigments including chlorophyll (Chl) and/or bacteriochlorophyll (BChl) and carotenoid molecules, and some of them also contain phycobilin (Fig.II-1). These photosynthetic pigments, exhibiting high extinction coefficient, are involved in primary reactions in photosynthesis, and chlorophyll is more essential in the light harvesting, and the exciton and electron transfers.

Photosynthetic organisms utilize most of the wavelength in the solar radiation from near UV (~350 nm) to the near-infrared region (~1050 nm). To use such wide range of the wavelength, they have evolved diverse Chls or BChls with various chemical and spectroscopic properties. To date, twelve types of Chls (Chl *a*, *b*, *d*; divinyl-Chl *a* and *b*; 8^1-hydroxy-Chl *a*) and BChls (BChl *a, b, c, d, e*, and *g*) have been identified [1]. The diverse Chl molecules are classified into only two groups according to its structure: chlorin and bacteriochlorin structures (Fig.II-2). All the Chls are synthesized from one precursor, chlorophyllide *a* (Chlide) that possesses chlorin structure, and the Chlide is also synthesized from protochlorophyllide (Pchlide) that possesses porphyrin structure (Fig.II-3). These three base structures (porphyrin, chlorin, and bacteriochlorin) differ in number of double bond within their molecular frame (Fig.II-2). As the double bond in the base structure decreases, the absorption peak of the pigment is drastically red-shifted. Based on the basic chlorine structure of Chlide, a diverse set of enzymes creates characteristic molecular structures that provide chemical and functional diversity to the pigment (Fig.II-3) [1]. On the other hand, all photosynthetic organisms share a set of enzymes for the biosynthesis of Chlide.

Biosynthesis of Chlide via two separate enzymatic reactions

Childe is synthesized from Pchlide, in which a double bond of ring-D in Pchlide is reduced as indicated by blue and red arrows in Fig.II-3. Two different enzymes function separately to catalyze the stereo-specific reduction: One is light-dependent Pchlide oxidoreductase (LPOR) utilizing light energy, and the other is light-independent (dark-operative) Pchlide oxidoreductase (DPOR) irrespective of light [2]. Primitive anoxygenic photosynthetic bacteria contain only DPOR. In contrast, oxygenic photosynthetic organisms including cyanobacteria, algae, and gymnosperms (nonflowering plants) contain both DPOR and LPOR, and angiosperms contain only LPOR. Because of the lack of DPOR, angiosperms are incapable of synthesizing Chls and BChls in the dark condition.

DPOR in the anoxygenic photosynthetic organisms utilizing BChl consists of BchL, BchN and BchB subunits, while that in the oxygenic photosynthetic organisms containing Chl involves similar subunits called ChlL, ChlN and ChlB. It should be noted that there is no sequence similarity between the DPOR and the LPOR which is formed by a single protein. On the other hand, BchL/ChlL, BchN/ChlN and BchB/ChlB subunits of DPOR exhibit structural/functional similarities to NifH, NifD, and NifK subunits in nitrogenase enzyme, respectively (Fig.II-4).

Enzymatic reaction of nitrogenase

Nitrogen atom (N), which is included in many biomolecules and all proteins, is essential to all living organisms. The organisms take in the atom via assimilation of ammonia (NH_3). NH_3 is generated from dinitrogen (N_2), constituting ~80% of air, through the reductive conversion of N_2 into NH_3, known as nitrogen fixation. There are two major processes for the nitrogen fixation. The one is the industrial Haber-Bosch reaction accounting for ~50% of the total nitrogen fixation per year, in which high pressure (200 atm.), high temperatures (450 ^{o}C), and Fe based catalysts are required. The other ~50% is produced via biological nitrogen fixation which occurs mainly in microbes, called diazotrophs, and nitrogen fixing bacteria. The nitrogen fixing organisms possess in common a metalloenzyme nitrogenase catalyzing the reduction of N_2 to NH_3. The enzymatic reaction is driven by two components of Fe- and FeMo-proteins (Fig.II-4). The Fe-protein, which is a homodimer formed by two identical NifH subunits, includes one [4Fe-4S] cluster ligated by four Cys residues and acts as a MgATP-dependent electron courier to the FeMo-protein. The FeMo-protein, which is a heterodimer of NifD and NifK subunits, contains two metallo centers: a [1Mo-7Fe-9S-X-homocitrate] cluster (called FeMo-cofactor) and a [8Fe-7S] cluster (called P-cluster). The former metal cluster functions as an active site for the reduction of N_2, and the latter one is involved as an electron transfer intermediate between the metal cluster and [4Fe-4S] cluster in Fe-protein.

Figure II-5 shows reaction scheme of the nitrogen turnover cycle [3]. Firstly, Fe-protein with a [4Fe-4S] cluster in (1+) oxidation state is combined with MgATP molecules (state a). Secondly, MoFe-protein is associated with the Fe-protein containing MgATP molecules (state e). The binding triggers the hydrolysis of the MgATP molecules to MgADP molecules, followed by the transfer of a single electron from the [4Fe-4S] cluster in Fe-protein to P-cluster in MoFe-protein (state f). The electron is further transferred to the active site metal cluster, FeMo-cofactor, and employed to the reduction of the bound substrate, N_2. Finally, the Fe-protein with the MgADP molecules is dissociated from the MoFe-protein in order to exchange the MgADP with MgATP (state c). In the interval of the exchange, the [4Fe-4S] cluster in Fe-protein is reduced probably by ferredoxin or flavodoxin (state b). This reaction cycle is repeated at least until the NH_3 synthesis is completed. In

the cycle, oxidation states of the metal clusters vary frequently, and each state exhibits characteristic EPR signal [3].

Structural features of DPOR

DPOR consists of two protein components, exhibiting structural and functional similarities to nitrogenase enzyme (Fig.II-4). The protein structures of the two components were solved using the DPOR from purple bacteria (i.e. anoxygenic photosynthetic organism) [4,5]. The one component is a homodimer formed by two identical BchL subunits, called L-protein. It contains one [4Fe-4S] cluster (referred to as L-cluster) and functions as an ATP-dependent electron donor as nitrogenase Fe-protein containing a [4Fe-4S] cluster. Both binding sites for [4Fe-4S] cluster and MgATP molecule are highly conserved between the two homologous proteins. The other component is a heterodimer formed by BchN and BchB subunits, called NB-protein. The crystal structures of the NB-protein were solved both in the Pchlide-bound and Pchlide-unbound states, showing that two NB-proteins form one dimer [5]. The overall structure is similar to that of MoFe-protein of nitrogenase. The NB-protein carries one [4Fe-4S] cluster (referred to as NB-cluster) at the center position between BchN and BchB, corresponding to P-cluster which is also located at the center in the MoFe-protein of nitrogenase. Although other metal cluster corresponding to FeMo-cofactor is absent in NB-protein, there is an active site for binding of substrate Pchlide. The distance between the NB-cluster and the Pchlide binding site is 10.0 Å, which is short enough for direct electron transfer.

Reduction and protonation processes of Pchlide in DPOR

It was clarified that BchB possesses a unique strand structure at the C-terminal region formed by approximately 100 amino acid residues, although the distal structure of the α-helix is still unclear (Fig.II-6). The counterpart is absent in NifK of the MoFe-protein in nitrogenase, while the unique α-helix is well conserved in the known BchB/ChlB proteins. The α-helix from BchB' is located at the boundary surface between the two NB-proteins in proximity to the Pchlide binding cavity between BchN and BchB proteins. The crystal structure of NB-cluster with Pchlide indicates a significant conformational change of the α-helix induced by binding of the substrate (Fig.II-6B). The altered α-helix forms a lid structure closing the substrate binding cavity, which seems to make the binding tighter. Another noteworthy conformation change due to the alteration of α-helix is found in the binding Pchlide, in which the propionate side chain at C17 is distorted.

The DPOR reaction model based on the structural data suggests that the stereo-specific reduction of C17=C18 double bond on the D-ring of Pchlide is accompanied by two proton transfers from the Asp274 provided from BchB' and the propionate of Pchlide to the C17 and C18, respectively (Fig.II-7A) [5]. The propionate is sufficiently close (4.8 Å) to the C18 position because of the unique

distorted configuration in the Pchlide-binding state. The reduction/protonation reactions are triggered by the electron transfer from the L-cluster to the Pchlide via the NB-cluster as that from the [4Fe-4S] cluster to the FeMo-cofactor via the P-cluster in nitrogenase complex. The oxidized L-protein is reduced by ferredoxin and then employed to next turnover.

Iron sulfur clusters in DPOR

Primary process in the DPOR enzymatic reactions is a single electron transfer from L-cluster to NB-cluster. The L-cluster is a conventional [4Fe-4S] cluster ligated by four Cys residues (Fig.II-8). It is located at the center between two BchL proteins forming a homodimeric L-protein, in which each BchL protein provides two Cys lingnds for the L-cluster binding. The NB-cluster is also located at the center between two proteins that are BchN and BchB proteins forming a heterodimeric NB-protein. On the other hand, it exhibits a unique binding motif that the [4Fe-4S] cluster is coordinated by three Cys residues from BchN and one Asp residue from BchB, which are defined as BchN-C26, BchN-C51, BchN-C112, and BchB-D36 in Fig.II-9A, respectively. The BchB-Asp36 is entirely conserved in all known BchB/ChlB subunits, but not in NifK of nitrogenase. Other Cys residue (BchB-C95), which has been assumed to be the fourth ligand, is located close to the NB-cluster, but not connects directly with the NB-cluster.

The site-directed mutants of the three Cys ligands or the BchB-C95 produce monomeric BchN and BchB not the BchN-BchB dimer, indicating that the Cys residues are essential for the formation of the dimeric structure of NB-protein [5]. The Asp36 mutants showed no enzymatic activity, although the BchN-BchB dimer is constructed [5]. Even the mutant that the Asp36 is replaced by a Cys residue results in complete loss of the activity despite forming a 4Cys-ligated [4Fe-4S] cluster as the conventional type cluster (Fig.II-9B). The results suggest a unique role of the Asp residue as a ligand of the cluster in DPOR.

The enzymatic reactions of DPOR are similar to that of nitrogenase. In particular, both the enzymes possess the brilliant function to break chemically inert multibonds. Nitrogenase employs the complicated metal clusters, P-cluster and FeMo-cofactor, to accomplish the reaction. LPOR, which also catalyzes the reduction of the double bond of Pchlide, utilizes light energy. On the other hand, DPOR contains only common [4Fe-4S] cluster and cannot employ light energy for the enzymatic reaction. Therefore, different strategies such as the conformational change of the binding-substrate and/or the unique Asp ligand of NB-cluster seem to be applied. However, properties of the NB-cluster, especially functions of the Asp ligand, are unclear. It is difficult to identify the dark-operating reaction process in DPOR because it is not triggered by the light. The situation is in contrast to that of LPOR, in which light-induced intermediate states are stably trapped at low temperature [6,7].

Outline of this chapter

I studied the NB-cluster by using EPR spectroscopy. In order to trap an intermediate state of the NB-cluster, Chl *c* molecule was used as a substrate analogue, the C17=C18 double bond on the D-ring of which is not reduced/protonated because of an acrylate at the C17 position instead of a propionate in Pchlide (Fig.II-7B). The native NB-cluster exhibited a broad EPR signal that is characterized by the high spin state of $S = 3/2$. Meanwhile, a mutant NB-protein, in which the Asp ligand was replaced by a Cys ligand, exhibited an $S = 1/2$ EPR signal of NB-cluster and lost of the catalytic activity for the reduction of Pchlide. The results suggest that the unique Asp ligand contributes to the electronic structure of the cluster and produces the low redox potential necessary for the Pchlide reduction reaction.

Figures

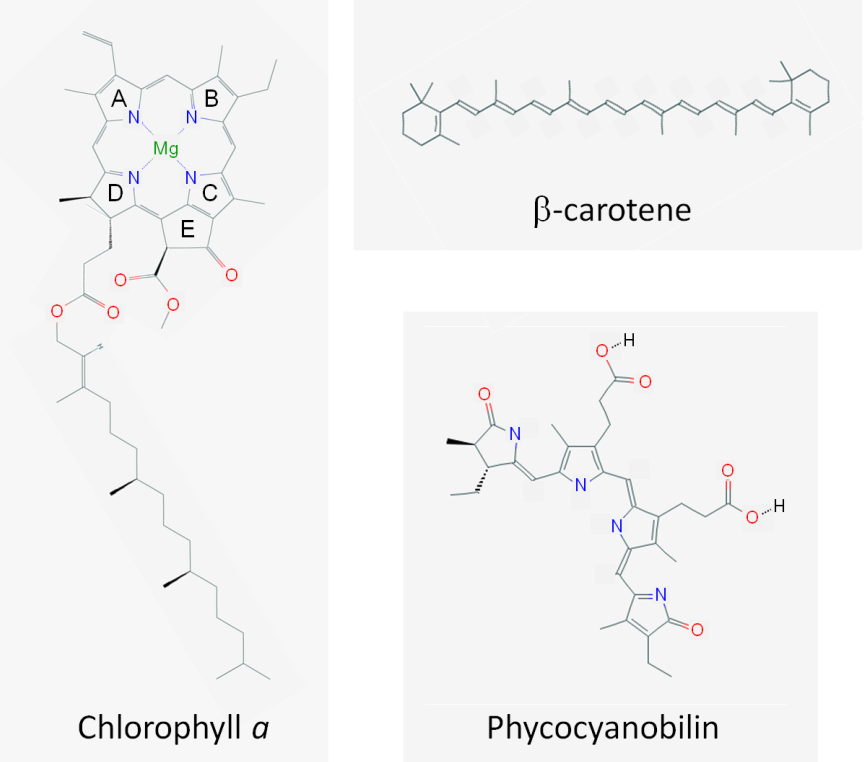

Figure II-1: Molecular structures of typical photosynthetic pigments. Chl is formed of five rings defined as A-E.

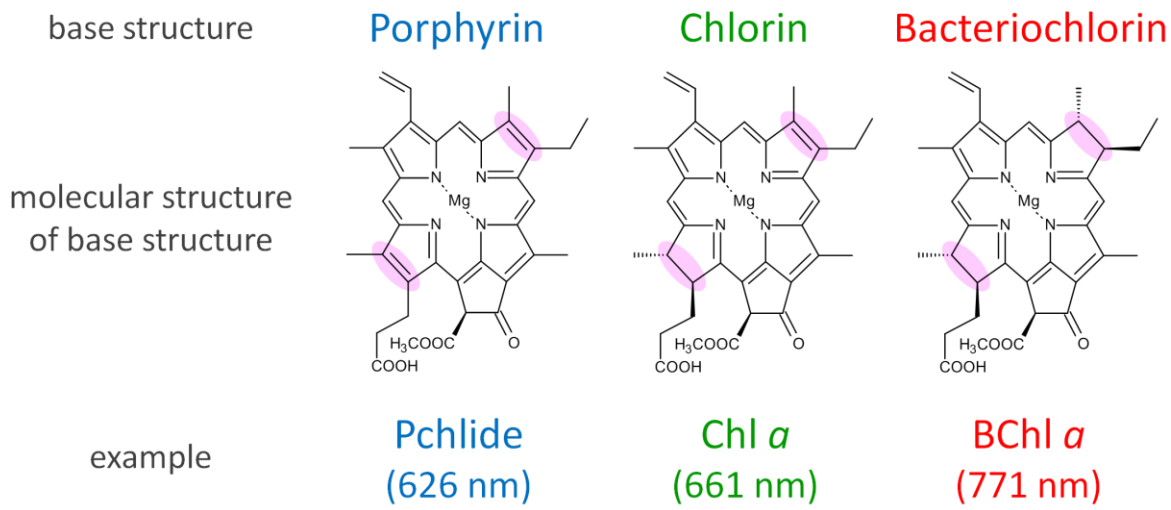

Figure II-2: Three different base structures (porphyrin, chlorin, and bacteriochlorin) of Chl molecule. Specific bonds are highlighted in pink. Pchlide, Chl *a*, and BChl *a* have each different base structure. As the double bond in the base structure decreases, the absorption peak of the pigment is drastically red-shifted.

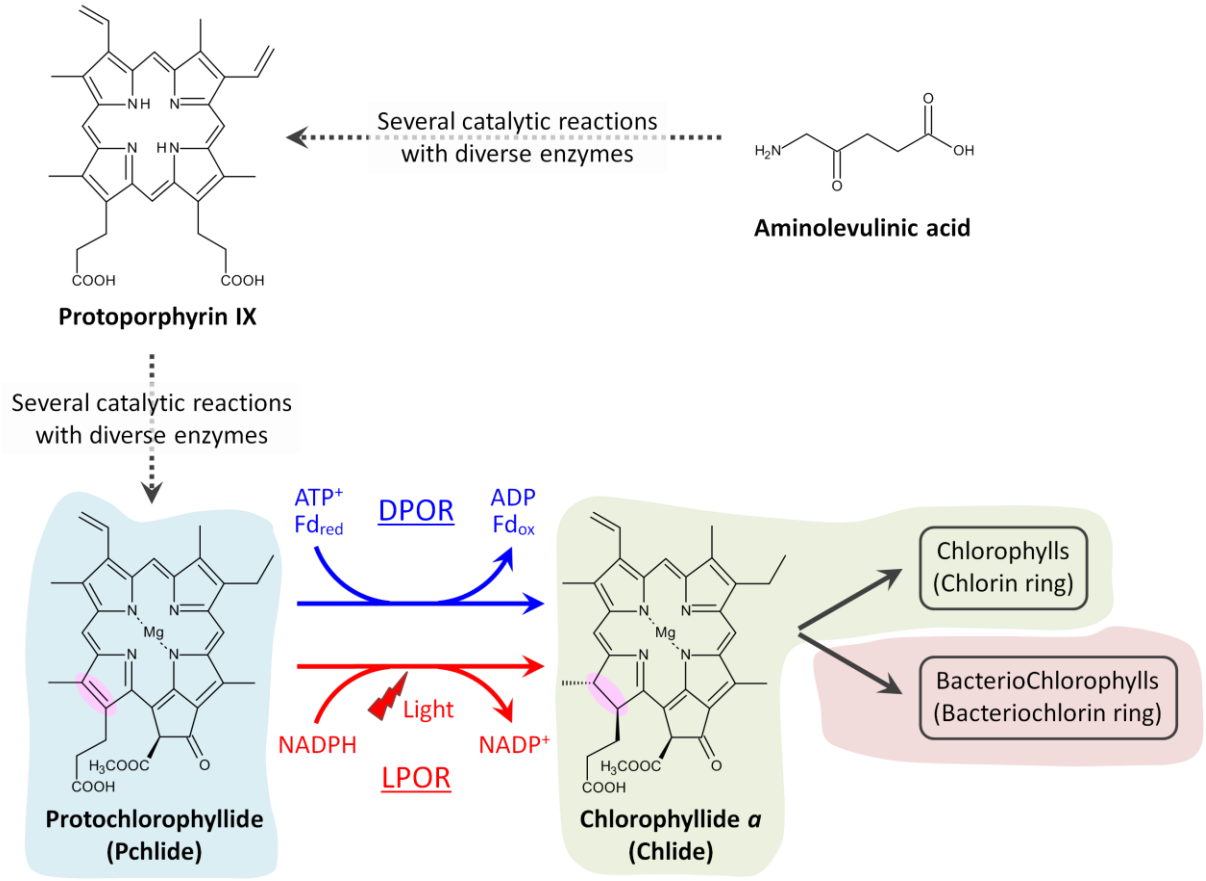

Figure II-3: Chlorophyll biosynthetic pathway. Chls that has porphyrin, chlorin, and bacteriochlorin structures are highlighted in light blue, light green, and light red, respectively. The synthetic processes of Chlide from Pchlide with DPOR and LPOR are represented in blue and red arrows, respectively, and the double bond reduced in the reaction is highlighted in pink.

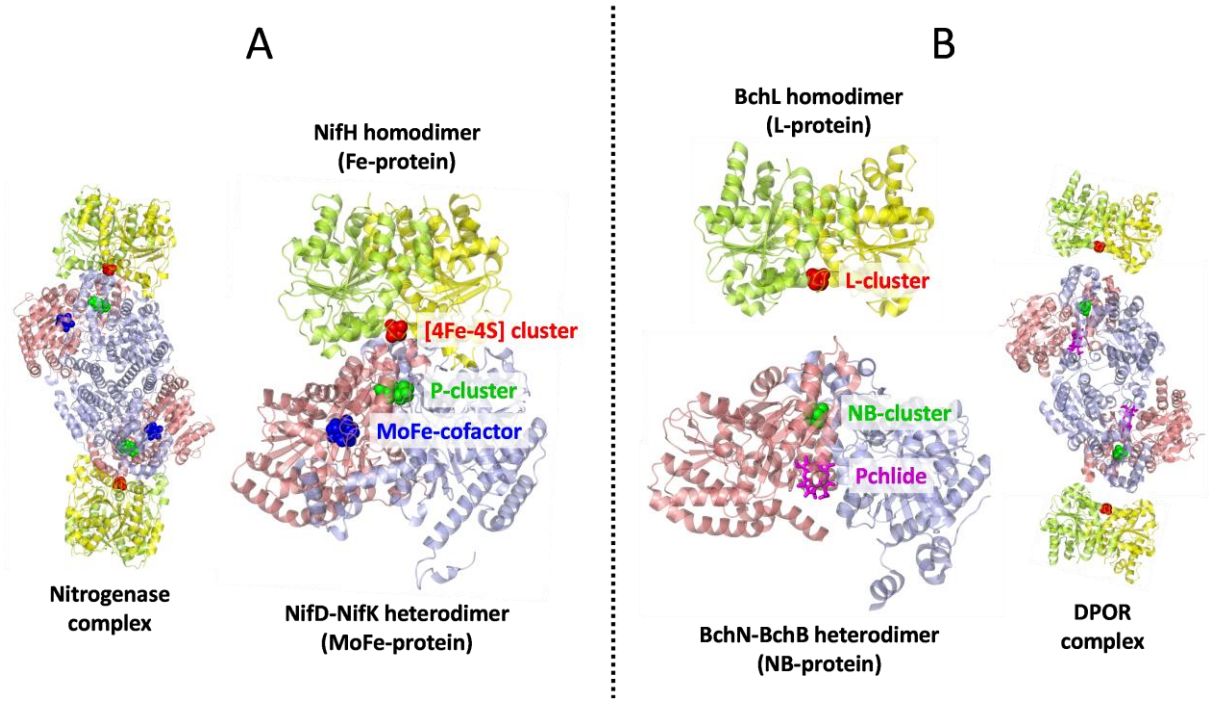

Figure II-4: X-ray crystal structures of (A) nitrogenase and (B) DPOR. (A). nitrogenase complex consisting of Fe- and MoFe-proteins from *Azotobacter vinelandii* (PDB entry 1N2C) [9]. Two NifH in Fe-protein are represented in light yellow and light green, and NifD and NifK in MoFe-protein are represented in light red and light blue, respectively. [4Fe-4S] cluster, P-cluster, and MoFe-cofactor are represented in red, green, and blue, respectively. (B). L-protein from *Rhodobacter sphaeroides* (upper) (PDB entry 3FWY) [4] and NB-protein from *Rhodobacter capsulatus* (lower) (PDB entry 3AEK) [5]. The crystal structure of DPOR complex that L-protein is associated with NB-protein has been identified. Two BchL in L-protein are represented in light yellow and light green, and BchN and BchB in NB-protein are represented in light red and light blue, respectively. L-cluster, NB-cluster, and Pchlide are represented in red, green, and purple, respectively.

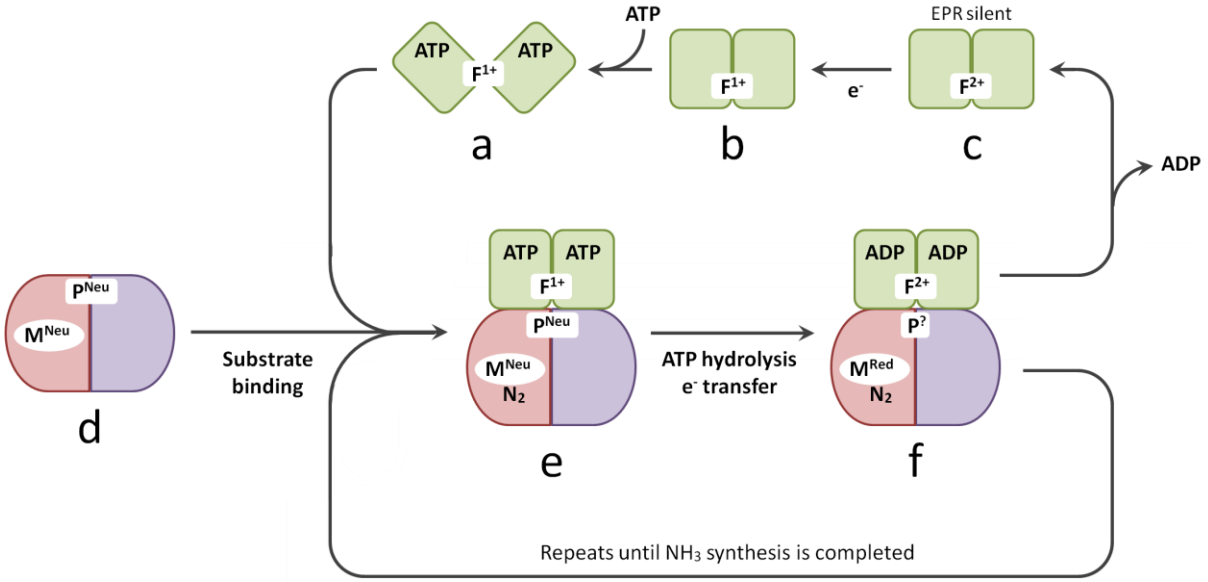

Figure II-5: Reaction scheme of the nitrogenase turnover cycle based on [3]. Fe- and MoFe-proteins are represented as pairs of light green boxes and of light red and purple boxes, respectively. [4Fe-4S] cluster is shown as ”F” within the Fe-protein with the oxidation state noted. P-cluster and FeMo-cofactor are shown as ”P” and “M” within MoFe-protein with the oxidation state noted, respectively.

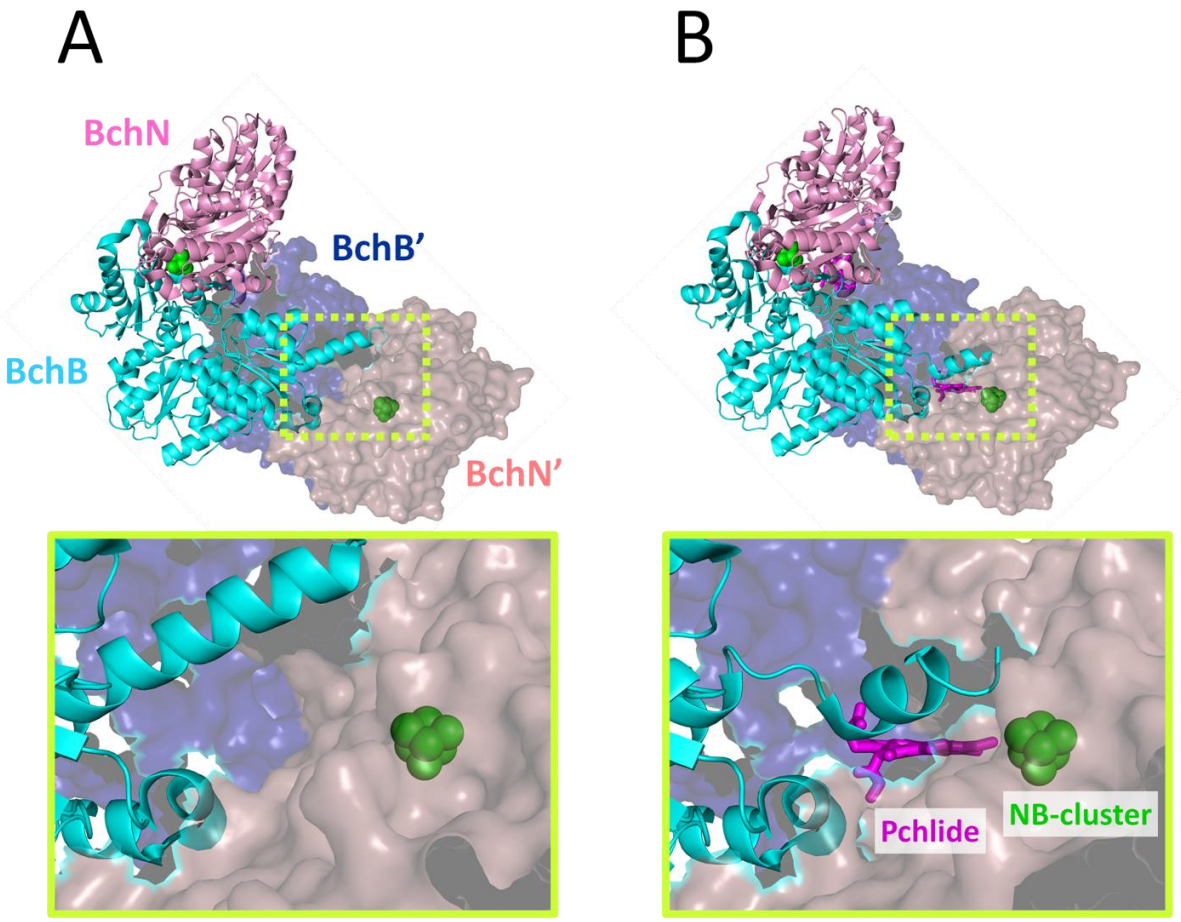

Figure II-6: (A, B). Dimeric structures formed by two NB-proteins in (A) Pchlide-unbinding (PDB entry 3AER) and (B) Pchlide-binding states (PDB entry 3AEK) [5], in which one NB-protein (BchN-BchB protein complex) is shown as molecular surface presentation and the other (BchN'-BchB' protein complex) as ribbon model. Protein structures around the Pchlide binding site located between BchN and BchB proteins (indicated by light green dotted squares in the upper panels) are expanded in the lower panels. The unique strand structures at the C-terminal region, which undergoes the significant conformation change with binding of Pchlide, are found. The BchB' that is other than BchB of the NB-protein with Pchlide provides the α-helix in proximity to the Pchlide binding cavity.

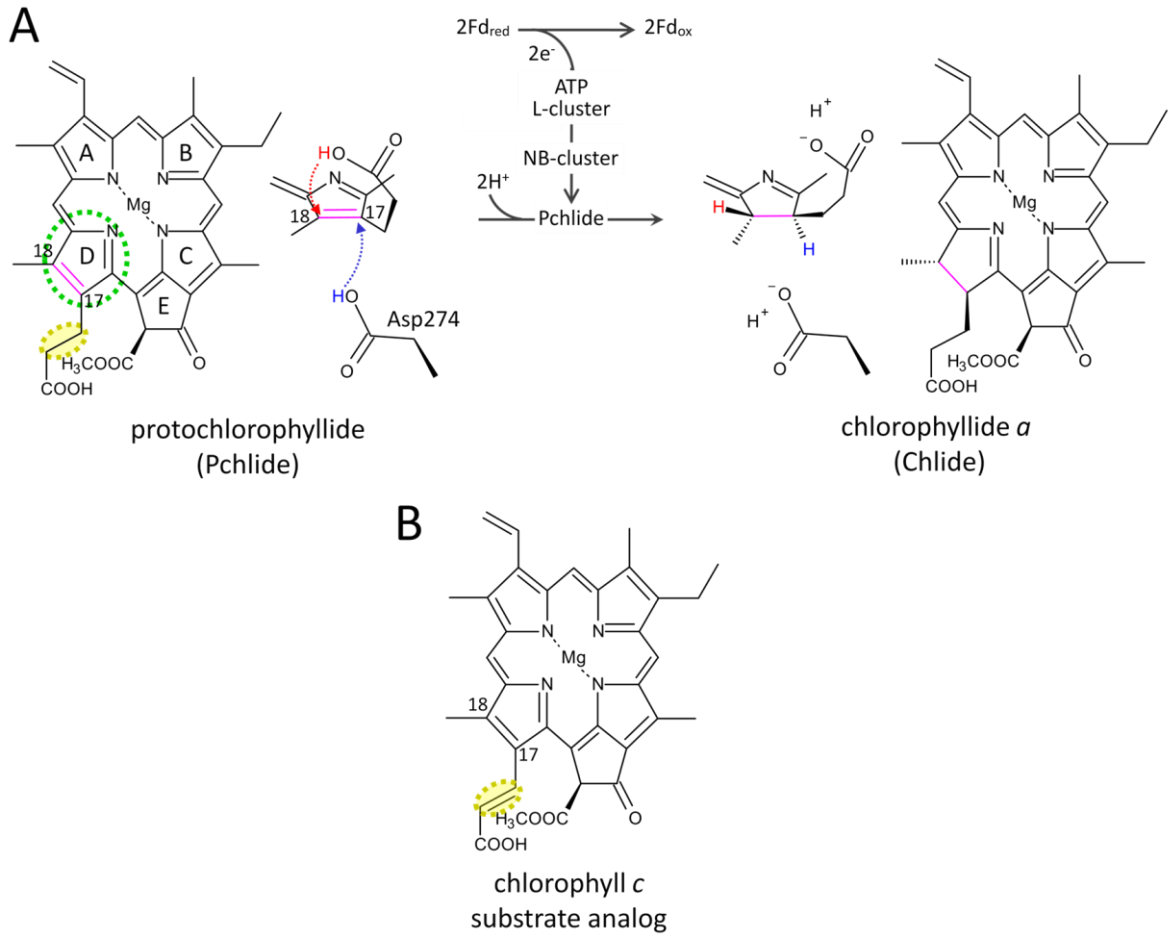

Figure II-7: (A). Schematic model for the reduction/protonation reactions of Pchlide to Chlide catalyzed by DPOR. It was proposed based on the structural data [2,5]. Green dotted circle indicates the D-ring of Pchlide including C17=C18 double bond (in pink), which is reduced in the reaction. (B). Molecular structure of chlorophyll *c* (Chl *c*) that is a substrate analog of Pchlide. The structural difference between Pchlide and Chl *c* is highlighted in yellow.

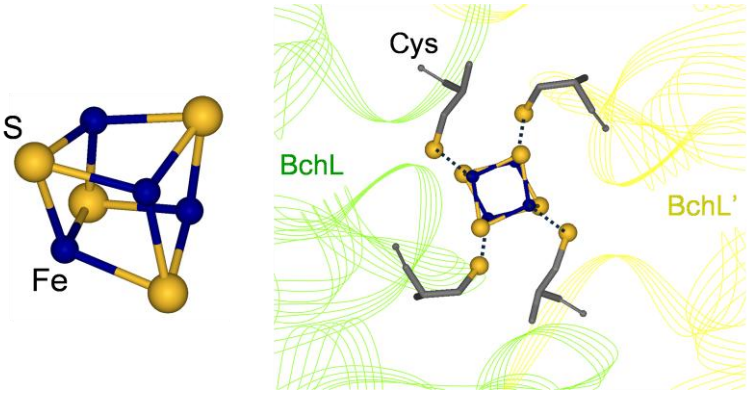

Figure II-8: Crystal structure of the cubane-type [4Fe-4S] L-cluster (left) and the binding motif in L-protein (right) (PDB entry 3FWY) [4]. Large spheres in brownish yellow and small spheres in dark blue represent sulfur (S) and iron (Fe) atoms, respectively. Dotted lines in dark blue indicate interatomic bonds between Fe atom of the cluster and S atom of Cys residues in protein. Green and yellow ribbons represent protein backbones belong to BchL and BchL' subunits in homodimeric L-protein, respectively. Two Cys ligands are provided from each subunit.

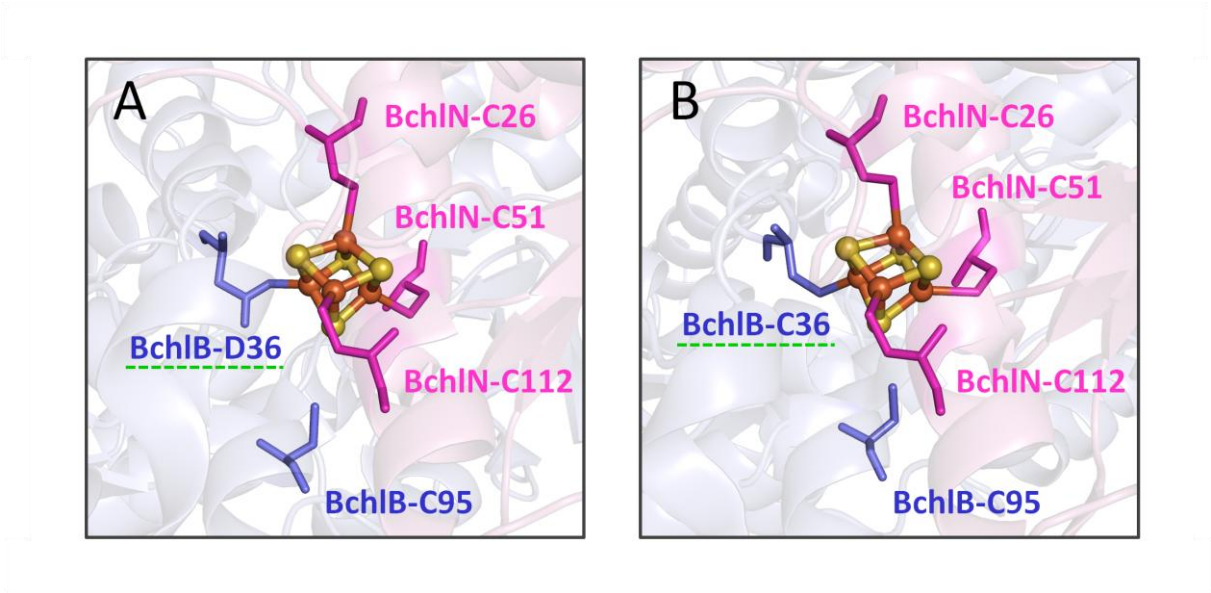

Figure I-9: Binding motifs of the NB-cluster in (A) wild-type NB-protein (PDB entry 3AER) and (B) the D36C mutant (PDB entry 3AET), in which the Asp36 (D36) is replaced by a Cys residue (C36) [5].

References

[1] Maqueo Chew, A.G. and Bryant, D.A. (2007) Chlorophyll biosynthesis in bacteria: The origins of structural and functional diversity, Annu. Rev. Microbiol. 61, 113-129.

[2] Reinbothe, C., El Bakkouri, M., Buhr, F., Muraki, N., Nomata, J., Kurisu, G., Fujita, Y. and Reinbothe, S. (2010) Chlorophyll biosynthesis: spotlight on protochlorophyllide reduction, Trends Plant Sci. 15, 614-624.

[3] Igarashi, R.Y. and Seefeldt, L.C. (2003) Nitrogen fixation: The mechanism of the Mo-dependent nitrogenase, Crit. Rev. Biochem. Mol. 38, 351-384.

[4] Sarma, R., Barney, B.M., Hamilton, T.L., Jones, A., Seefeldt, L.C. and Peters, J.W. (2008) Crystal structure of the L protein of *Rhodobacter Sphaeroides* light-Independent protochlorophyllide reductase with MgADP bound: A homologue of the nitrogenase Fe protein, Biochemistry 47, 13004-13015.

[5] Muraki, N., Nomata, J., Ebata, K., Mizoguchi, T., Shiba, T., Tamiaki, H., Kurisu, G. and Fujita, Y. (2010) X-ray crystal structure of the light-independent protochlorophyllide reductase, Nature 465, 110-U124.

[6] Heyes, D.J., Heathcote, P., Rigby, S.E.J., Palacios, M.A., van Grondelle, R. and Hunter, C.N. (2006) The first catalytic step of the light-driven enzyme protochlorophyllide oxidoreductase proceeds via a charge transfer complex, J. Biol. Chem. 281, 26847-26853.

[7] Heyes, D.J. and Hunter, C.N. (2005) Making light work of enzyme catalysis: protochlorophyllide oxidoreductase, Trends Biochem. Sci. 30, 642-649.

[8] Schindelin, N., Kisker, C., Sehlessman, J.L., Howard, J.B. and Rees, D.C. (1997) Structure of ADP· AlF_4^--stabilized nitrogenase complex and its implications for signal transduction, Nature 387, 370-376.

EPR study of 1Asp–3Cys ligated 4Fe–4S iron–sulfur cluster in NB-protein (BchN–BchB) of a dark-operative protochlorophyllide reductase complex

Introduction

Chlorophylls (Chls) work for the solar energy capture and charge separation in photosynthesis. In the biosynthesis of Chl *a*, dark-operative (light-independent) protochlorophyllide (Pchlide) oxidoreductase (DPOR) catalyzes the stereo-specific reduction of C17=C18 double bond on the D-ring of Pchlide [1,2], as shown in Fig. 1A. The Pchlide reduction is the final step to give the spectroscopic properties of Chl *a*, which plays crucial roles inside the photosynthetic protein complexes of plants and cyanobacteria. DPOR is widely distributed from anoxygenic photosynthetic bacteria to cyanobacteria, algae, plants [2], and its function is replaced by light-dependent protochlorophyllide oxidoreductase (LPOR) in higher plants.

DPOR is consists of two components, the L-protein (a BchL dimer) and the NB-protein (a BchN-BchB heterotetramer) [3], as shown in Fig. 1B. The L-protein functions as an ATP-dependent reductase that is specific for the NB-protein [4]. The L-protein carries a [4Fe-4S] cluster (the L-cluster) between the protomers that is very similar to that of the nitrogenase Fe protein [5]. The NB-protein provides the catalytic site for Pchlide reduction. The NB-protein also carries a [4Fe-4S] cluster (the NB-cluster) that mediates electrons from the L-cluster to the Pchlide molecule [6]. A recent X-ray structural analysis revealed that the NB-cluster is held between the BchB and BchN subunits, ligated by one Asp from BchB and three Cys from BchN [7] (Fig. 1C). All the ligating amino acid residues of the cluster are conserved in all the BchB and BchN proteins [2]. The enzymatic activity to reduce Pchlide was lost in a mutant D36C NB-protein, in which the Asp residue was replaced by a Cys residue, indicating a crucial role of the Asp ligand in the Pchlide reduction [7], although a conventional [4Fe-4S] cluster was formed (Fig. 1D) [7].

Although no inter-subunit [4Fe-4S] clusters such as the NB-cluster have been reported, Asp-ligated intra-molecular [4Fe-4S] clusters have been reported in ferredoxins of hyperthermophilic archaea, *Pyrococcus furiosus* [8] and *Thermococcus profundus* [9]. The electron paramagnetic resonance (EPR) study indicated the unique feature of the [4Fe-4S] cluster of *P. furiosus* [10-12]. The redox potential of the [4Fe-4S] cluster of the archeal ferredoxin was a little deviated from the typical [4Fe-4S] clusters [11,13]. The electronic structure of NB-cluster has not been characterized

well, although preliminary EPR studies of the NB-cluster suggested some anomalous features [6,14]. In this study, we identified an unusually broad EPR signal with a spin state of S = 3/2 of the NB-cluster. The intensity of this signal increased markedly in the presence of the L-protein, ATP, Chl *c*, and dithionite. On the other hand, the signal changed to a rhombic one with S = 1/2 in the NB-cluster of a D36C NB-protein with the loss of enzymatic activity, as reported in this study. We discussed the role of the Asp ligand in the spin state determination and function of the NB-cluster.

Materials and methods

Protein preparations

The NB-protein and the L-protein were prepared as reported [4,6]. A D36C variant of the NB-protein was purified as reported [7]. The protein concentrations were determined using a protein assay (Bio-Rad) with bovine serum albumin as a standard.

EPR measurements

EPR measurements were carried out using a Bruker ESP-300E X-band spectrometer (Bruker Biospin, Germany) with a 100 kHz field modulation equipped with a liquid-helium flow cryostat (CF935, Oxford Instruments, Oxford, UK). The measurement parameters are described in the figure legends.

Results and discussion

EPR signals of the L-cluster and the NB-cluster in DPOR

In previous work, we detected only a weak EPR signal of the NB-cluster under enzyme-turnover conditions, where small amounts of the L-protein, ATP, and dithionite were added to the NB-protein mixtures [6]. In this study, Chl *c* was added to the samples to trap and stabilize the NB-cluster in the reduced state because it is a competitive inhibitor [7] of Pchlide. The DPOR reaction is arrested at the Pchlide-reducing step in the presence of Chl *c*, and the reduced NB-cluster is expected to accumulate.

Figure 2 shows EPR spectra measured at 5 K and 20 K of a mixture of the L-protein and Chl *c* in the presence of ATP and dithionite (traces a and a'). The spectrum indicated a signal in a g = 2 region at both 5 K and 20 K. The intensity became lower at 20 K. A simulated spectrum (gray solid line) calculated with assumed g-values of g_z = 2.021 (with an 8 mT line width of a full width at 1/*e* maximum), g_y = 1.948 (1 mT), and g_x = 1.861 (6 mT) closely matched this spectrum. The signal shapes and g-values were almost the same as those reported for the L-cluster [4]. The result indicated that the L-cluster was easily reduced by dithionite with ATP and Chl *c*.

Figure 2 traces b and b' show an EPR spectrum of a mixture of the NB-protein and Chl *c* without the L-protein. The NB-protein gave a broad signal in a g = 2 region with a negative peak at g = 1.92 at 5 K. Additional narrow signals were detected at g = 5.1, 4.6, and 2.0. At 20 K, the broad signal nearly vanished, while the narrow signals could still be detected. Figure 2 traces c and c' show an EPR spectrum detected in a mixture of the NB-protein and Chl *c* in the presence of the L-protein, ATP, and dithionite. The L-cluster gave a signal in the g = 2 region, and induced the larger broad signal of the NB-protein. The L-cluster signal could be detected even at 20 K (trace c') in contrast to the complete disappearance of the broad signal at 20 K, as seen without the L-protein in trace b'. Figure 3 shows the temperature dependency of the g_z, g_y, or g_x peaks shown in Fig. 2, trace a (upper panel) and the 1-6 peaks in Fig. 2, trace c (lower panel). The g_z, g_y, and g_x peaks of the L-cluster reached their maxima at 9 K. Peaks 3 and 5 (black symbols) also reached their maxima at 9 K, showing the same temperature dependence. A narrow signal at g = 5.1 (cross symbols), which exhibited a similar temperature dependence, was also detected in the absence of the L-protein (Fig. 2, trace b), suggesting that the signal is derived from the NB-protein. The origin of another narrow signal at g = 4.6 (Fig. 2, trace b) is unclear and might be an artifact. The intensities of peaks 2, 4, and 6 (white symbols) declined sharply on warming and became too low to be detected above 15 K. No maxima appeared until 5 K. The common features of the three peaks suggest that these signals originate from one species in the NB-protein. A dashed line in Fig. 2 trace c shows an assumed

spectrum obtained by connecting peaks other than those of the L-cluster. It spreads over the magnetic field at 100 - 450 mT, showing a negative peak at g = 1.92 and a narrow one at g = 5.1.

When Chl *c* was omitted from the mixture of NB- and L-proteins, the broad signal of NB-cluster was no more detected, and only the signal from L-protein remained (data not shown). The binding of the substrate or a substrate analogue is, therefore, necessary to reduce the NB-cluster. The crystal structures of the NB-protein revealed a partial unwinding of the α-helix of BchB upon the binding of Pchlide [7]. The conformational change of the amino acid residues of this unwound motif, which interacts extensively with the Pchlide molecule, might help the electron transfer from the L-protein to the NB-cluster by optimizing the structure for the electron transfer and/or adjusting the redox potential of the cluster. We could detect a broad signal only in the presence of Chl *c*. Although Chl *c* binds to the substrate-binding pocket in the NB-protein in place of Pchlide, the C17=C18 double bond on the D-ring of Chl *c* is not reduced because of an acrylate at the C17 position instead of a propionate, which is presumed to be the proton donor, in Pchlide [7]. The trapping of the reduced state of the NB-cluster, which was realized in the presence of Chl *c*, thus, markedly increased the broad EPR signal.

Spin state of the NB-cluster

An EPR signal assigned to the NB-cluster was very broad and is obviously different from the $S = 1/2$ EPR signals of typical [4Fe-4S] clusters ligated by 4Cys ligands, as reported for ferredoxin I of *R. capsulatus* [15,16], which exhibit anisotropic peaks at around g = 2. The NB-cluster is coordinated by one Asp from a BchB subunit and three Cys from a BchN subunit (Fig. 1C) [7]. Similar [4Fe-4S] clusters with an Asp ligand have been reported in ferredoxins of the hyperthermophilic archaea *P. furiosus* [8] and *T. profundus* [9]. However, the Asp/Cys-ligated cluster formed between the two subunits has not been reported so far except for the NB-cluster.

An EPR spectrum of the Asp-ligated [4Fe-4S] cluster in *P. furiosus* ferredoxin also had a broad signal extending to the g = 5 to 2 region and was attributed to the Kramers doublets with a spin state of $S = 3/2$ [10]. The NB-cluster also exhibits a broad signal in a similar region, showing a spin state of $S = 3/2$. The spin relaxation of the narrow peak at g = 5.1 was slower than that of the other parts in the broad signal (Fig. 3). The slow relaxation seems to occur on a spin sublevel with $S = 1/2$ in the doublets, and the faster one with $S = 3/2$ because the spin relaxation caused by the environmental magnetic perturbation is expected to be faster with the increase of spin multiplicity. A similar behavior was observed in *P. furiosus* ferredoxin [10]. However, the g-values and the spectral shape of the EPR spectrum of the NB-cluster were different from those of *P. furiosus* ferredoxin, indicating different zero-field splitting parameters. A unique binding motif seems to affect the electronic structure of the NB-cluster. Figure 2 traces d and d' show the EPR spectra of the D36C NB-protein

measured at 5 and 20 K without the L-protein. The S = 3/2 broad signal of the NB-cluster was not detected at all. On the other hand, a rhombic EPR signal was detected at the g = 2 region both at 5 and 20 K, suggesting a slower spin relaxation rate compared to that of the wild-type NB-cluster. The simulated spectrum (a gray solid line in Fig. 2 trace d') calculated with g-values of g_z = 2.050 (10 mT), g_y = 1.938 (6 mT), and g_x = 1.885 (27 mT) fully reproduced the experimental signal. The signal in the D36C NB-protein, thus, can be attributed to the [4Fe-4S] cluster with S = 1/2 state ligated by four Cys residues.

The spin quantity estimated for the S = 1/2 signal was assumed to be comparable with that for the S = 3/2 signal in Fig. 2 trace c, based on the rough simulation (not shown) of the latter spectrum with tentative zero-field splitting parameters of *P. furiosus* ferredoxin [12]. Therefore, it is suggested that the D36C NB-cluster can be reduced by dithionite even without the L-protein and that the Asp ligand works to enhance the reducing power of the NB-cluster. Further studies are required to estimate precisely the spin quantity and the redox potential value of the NB-cluster. Similar changes of the spin state and the redox potential (within 60 mV) were reported in the Asp-Cys mutated [4Fe-4S] cluster of *P. furiosus* ferredoxin [11,13]. Although the 3D structures of the NB-clusters in the wild-type and D36C variant appear to be almost the same (Fig. 1C, D), a slight structural distortion seems to change the interaction between the Fe atoms in the NB-cluster to make the low-spin state to be the ground state.

Some 4Cys-ligated [4Fe-4S] clusters have been reported to exhibit high spin signals as follows; a high spin S = 3/2 state signal in 2-hydroxyglutaryl-CoA dehydratase from *Acidaminococcus fermentans* [17]; mixed S = 1/2 and 3/2 signals in nitrogenase Fe-protein from *Azotobacter vinelandii* [18-20]; S = 3/2 and 5/2 signals in ferredoxin from *Thauera aromatica* [21]; S = 1/2, 3/2, and 5/2 signals in glutamine phosphoribosylpyrophosphate amidotransferase from *Bacillus subtilis* [22]. A 4Cys-ligated cluster of a ferredoxin from *A. vinelandii* exhibited the same S = 1/2 spin signal both before and after the Cys/Asp replacement of one ligand [23]. Similar Cys/Asp replacement was applied to cluster F_A in PsaC protein of photosystem I (PS I), in which the spin state of the cluster turned from S = 1/2 to 3/2 as the dissociation of PsaC from PS I [24]. Solvent-dependent spin crossovers between the low and high spin states of [4Fe-4S] cluster are also known [10,18-20]. Therefore, Asp ligand might not be essential to produce a high spin state of a [4Fe-4S] cluster.

The inter-subunit 4Cys-ligated [4Fe-4S] cluster between two identical proteins like that in L-protein is known in nitrogenase Fe-protein, and in F_X clusters in the reaction centers of heliobacteria and green sulfur bacteria. Both S = 1/2 and 3/2 signals were reported (and are still debated) for F_X clusters of heliobacteria [25,26] and green sulfur bacteria [27,28]. The clusters in the homodimers exhibited isotropic S = 1/2 EPR spectra ascribed to a symmetrical structure [18-20,25], although there was an exception for that in green sulfur bacteria [27]. On the other hand, PS I heterodimer reaction

center forms only the low spin 4Cys-ligated F_X cluster that shows an anisotropic $S = 1/2$ EPR spectrum suggesting the asymmetrical electronic structure [29]. The D36C NB-protein, which is a heterodimer, produced the considerably isotropic EPR signal comparable to that in homodimeric L-protein. The electronic structure of the cluster seems to be uniform despite the asymmetric coordination.

Reaction of the NB-cluster

The redox potential of electron transfer cofactors in protein has been known to depend on many factors, such as the ligand amino acid residues, protein or dielectric environment, solvent accessibility, and/or hydrogen bonding around the cluster [30]. In the structure of the D36C NB-protein, the 4Cys-ligated NB-cluster is located in the same position as in the wild type protein, and the environment around the cluster appears to be almost the same. Relative positions of the L-cluster and the NB-cluster of the D36C NB-protein are not significantly different from those of the wild type [7]. However, the Asp/Cys ligand alteration modified the properties of the NB-cluster. The D36C NB-cluster was readily reduced by dithionite even without Chl *c* and L-protein, in contrast to the wild-type NB-cluster, which was only partially reduced by dithionite alone. In addition, the D36C NB-protein lost the enzymatic activity to reduce Pchlide [7]. Therefore, the redox potential of the D36C NB-cluster seemed to have become more positive and the cluster was reduced more readily by dithionite, compared to the wild-type NB-cluster. The positive shift of the redox potential, however, will make the electron transfer to Pchlide more difficult. We, therefore, assume that the Asp ligation contributes to make the redox potential of the NB-cluster to be negative enough to accomplish the two-electron reduction/conversion of the stable porphyrin ring to the chlorin ring. The Cys/Asp replacement of ligand was reported to significantly decrease the redox potential of cluster F_A in PsaC of PS I from -440 to -630 mV [24], while the slight positive shift of the redox potential was induced by Asp ligand in ferredoxins of *P. furiosus* [11] and *A. vinelandii* [23]. Asp ligand seems to tune the redox potential of a [4Fe-4S] cluster to suit for the proper function.

The high reducing power in the NB-cluster, which was enabled by the Asp ligation, would be the key to carry out the Pchlide reduction in a nitrogenase-like structure. However, the DPOR system, as well as the nitrogenase system, has an intrinsic weakness under an oxygenic atmosphere, namely, oxygen sensitivity [4]. The evolution in the ancient cyanobacteria have solved this problem by the incorporation of a different reducing mechanism, LPOR, in which Pchlide is reduced by a hydride from NADPH and a proton from a Tyr residue driven by light within the framework of the short-chain alcohol dehydrogenase/reductase family [31,32]. The LPOR system that requires light has introduced a new regulation step in the chlorophyll biosynthesis pathway in higher plants. The DPOR system, with the strong reducing power of the D36-ligated [4Fe-4S] cluster but dose not require light, is used widely in cyanobacteria, algae, and most of plants still now.

Figures

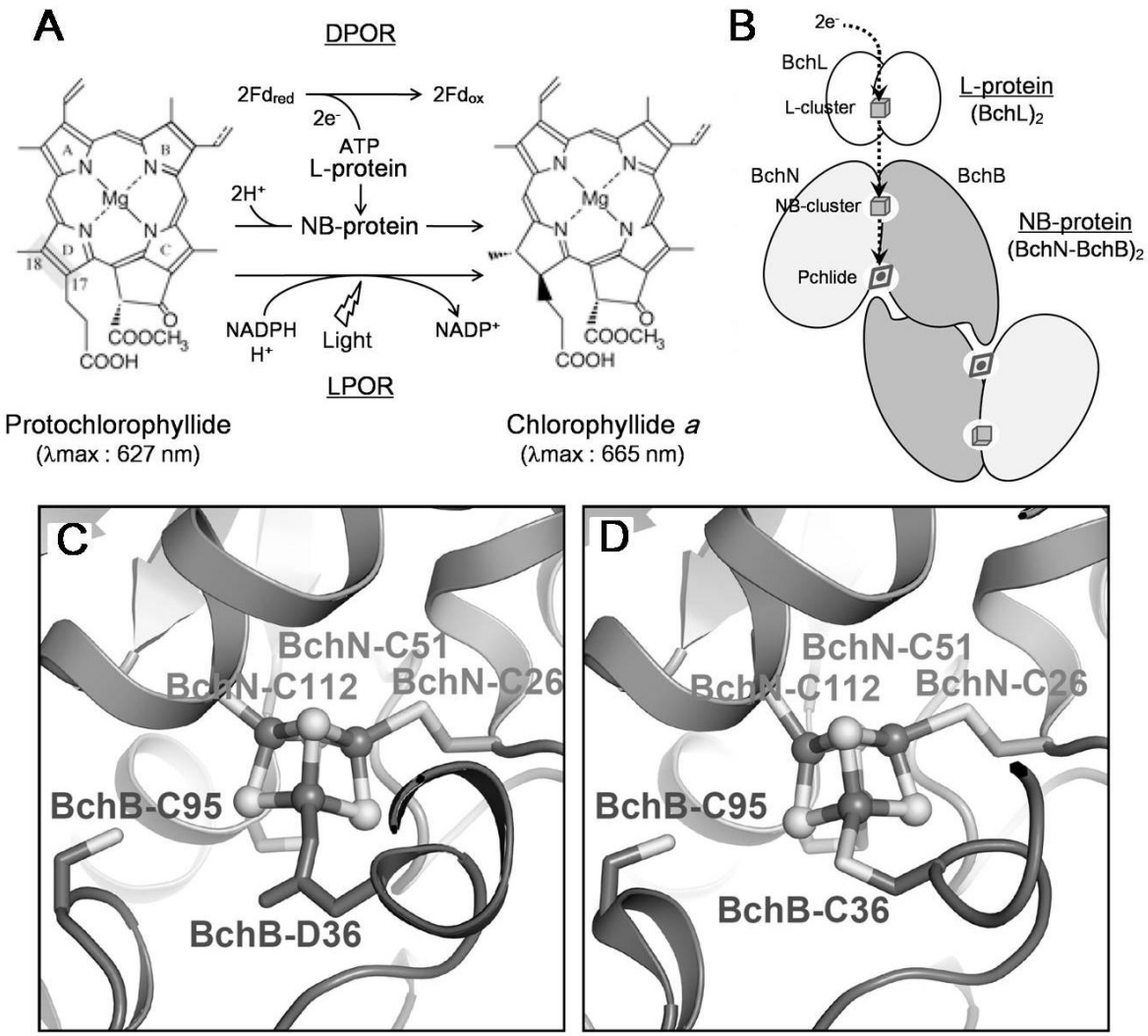

Figure 1: (A) Pchlide reduction by DPOR and LPOR. (B) A conceptual model of structure of DPOR complex. (C). Structures around the [4Fe-4S] cluster in the wild-type and D36C variant NB-protein. The structures were drawn according to [7].

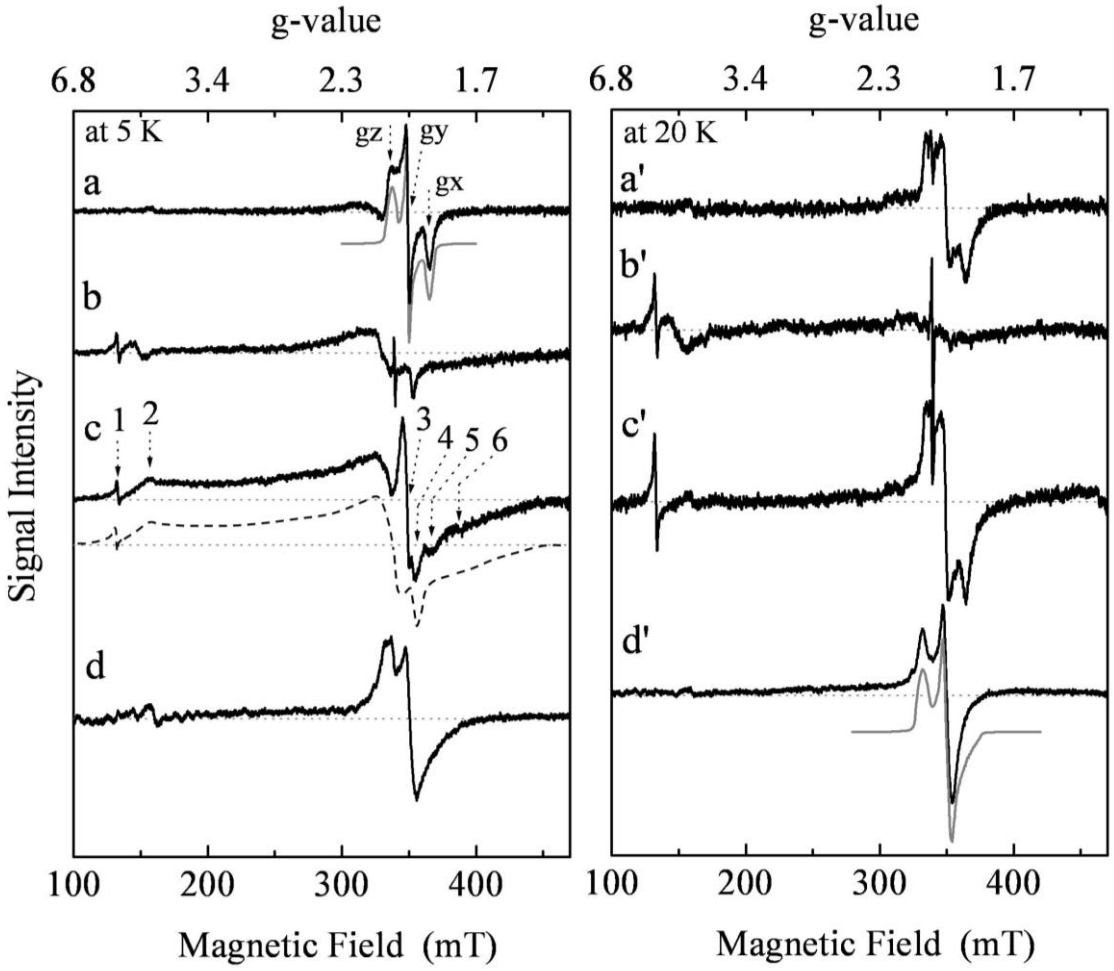

Figure 2: EPR spectra of the L-protein and the NB-protein under different reducing conditions at 5 K (left panel, traces a-d) and 20 K (right panel, traces a'-d'). EPR spectra were measured in the mixtures of (a, a') the L-protein and Chl *c*, (b. b') the NB-protein and Chl *c*, (c, c') the NB-protein, the L-protein, ATP, and Chl *c*, and (d, d') only the D36C variant of the NB-protein. All mixtures contained sodium dithionite (5 mM). The gray solid lines represent simulated spectra. A dashed line in trace c shows an assumed spectrum of the NB-cluster made by omitting the signal peaks due to the L-cluster. The NB-protein was 97 μM, and the L-protein was 6.4 μM in the DPOR assay mixture [3] containing 100 μM Chl *c*. The D36C NB-protein was 100 μM in the HEPES buffer (100 mM HEPES-KOH; pH 8.0, 8 mM DTT, 5 mM sodium dithionite). Experimental conditions for the measurements: microwave power, 20 mW; microwave frequency, 9.521 GHz; modulation amplitude, 2 mT at 100 KHz; time constant, 20 ms.

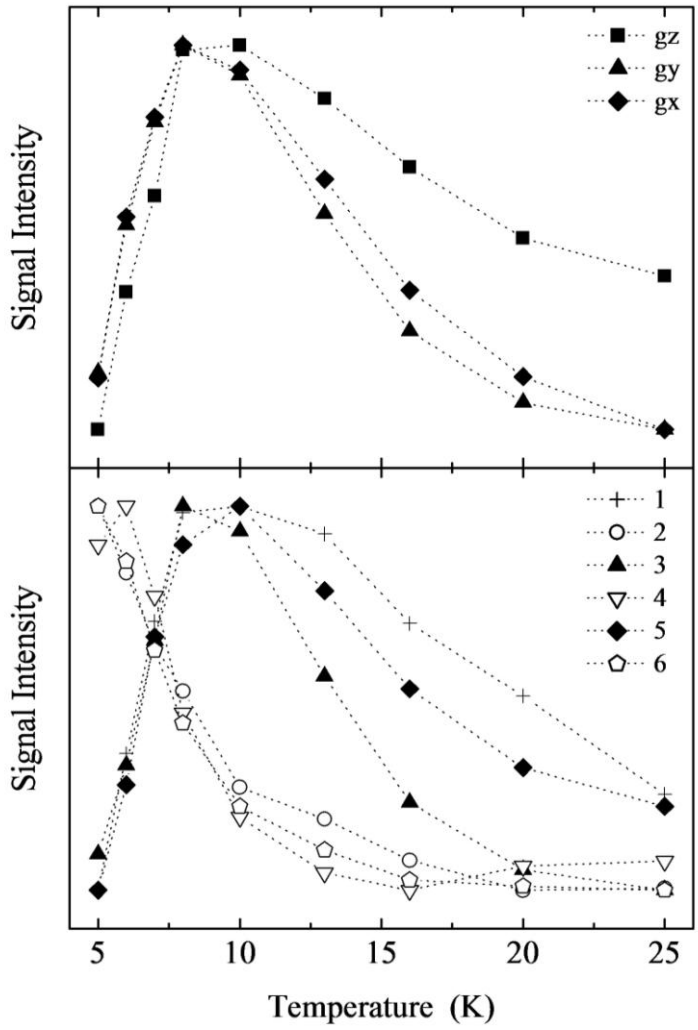

Figure 3: Temperature dependence of the intensity of EPR signals shown in Fig. 2. The intensities of the EPR signals at g_z, g_y, and g_x values in trace a in Fig. 2, are plotted against the temperature in the upper panel. The intensities at peaks 1 to 6 in trace c in Fig. 2 are shown in the lower panel. The intensities at the g_y peak and at peaks 1 and 3 were evaluated on the basis of the second derivative spectra.

References

[1] Fujita, Y., and Bauer, C. (2000). Reconstitution of light-independent protochlorophyllide reductase from purified BchL and BchN-BchB subunits. *In vitro* confirmation of nitrogenase-like features of a bacteriochlorophyll biosynthesis enzyme. J. Biol. Chem. 275, 23583-23588.

[2] Fujita, Y., and Bauer, C.E. (2003). The light-independent protochlorophyllide reductase: A nitrogenase-like enzyme catalyzing a key reaction for greening in the dark. In Chlorophylls and Bilins: Biosynthesis, Synthesis, and Degradation (Kadish, K., Smith, K.M., and Guilard, R., eds), pp. 109-156. Academic Press, Amsterdam.

[3] Nomata, J., Swem, L., Bauer, C., and Fujita, Y. (2005). Overexpression and characterization of dark-operative protochlorophyllide reductase from *Rhodobacter capsulatus*. Biochim. Biophys. Acta 1708, 229-237.

[4] Nomata, J., Kitashima, M., Inoue, K., and Fujita, Y. (2006). Nitrogenase Fe protein-like Fe-S cluster is conserved in L-protein (BchL) of dark-operative protochlorophyllide reductase from *Rhodobacter capsulatus*. FEBS Lett. 580, 6151-6154.

[5] Sarma, R., Barney, B., Hamilton, T., Jones, A., Seefeldt, L., and Peters, J. (2008). Crystal structure of the L protein of *Rhodobacter sphaeroides* light-independent protochlorophyllide reductase with MgADP bound: A homologue of the nitrogenase Fe protein. Biochemistry 47, 13004-13015.

[6] Nomata, J., Ogawa, T., Kitashima, M., Inoue, K., and Fujita, Y. (2008). NB-protein (BchN-BchB) of dark-operative protochlorophyllide reductase is the catalytic component containing oxygen-tolerant Fe-S clusters. FEBS Lett. 582, 1346-1350.

[7] Muraki, N., Nomata, J., Ebata, K., Mizoguchi, T., Shiba, T., Tamiaki, H., Kurisu, G., and Fujita, Y. (2010). X-ray crystal structure of the light-independent protochlorophyllide reductase. Nature 465, 110-114.

[8] Calzolai, L., Gorst, C., Zhao, Z., Teng, Q., Adams, M., and La Mar, G. (1995). ^{1}H NMR investigation of the electronic and molecular structure of the four-iron cluster ferredoxin from the hyperthermophile *Pyrococcus furiosus*. Identification of Asp 14 as a cluster ligand in each of the four redox states. Biochemistry 34, 11373-11384.

[9] Imai, T., Taguchi, K., Ogawara, Y., Ohmori, D., Yamakura, F., Ikezawa, H., and Urushiyama, A. (2001). Characterization and cloning of an extremely thermostable, *Pyrococcus furiosus*-type 4Fe ferredoxin from *Thermococcus profundus*. J. Biochem. 130, 649-655.

[10] Conover, R., Kowal, A., Fu, W., Park, J., Aono, S., Adams, M., and Johnson, M. (1990). Spectroscopic characterization of the novel iron-sulfur cluster in *Pyrococcus furiosus*

ferredoxin. J. Biol. Chem. 265, 8533-8541.

[11] Zhou, Z., and Adams, M. (1997). Site-directed mutations of the 4Fe-ferredoxin from the hyperthermophilic archaeon *Pyrococcus furiosus*: Role of the cluster-coordinating aspartate in physiological electron transfer reactions. Biochemistry 36, 10892-10900.

[12] Duderstadt, R.E., Brereton, P.S., Adams, M.W. and Johnson, M.K. (1999). A pure S = 3/2 $[Fe_4S_4]^+$ cluster in the A33Y variant of *Pyrococcus furiosus* ferredoxin. FEBS Lett 454, 21-6.

[13] Brereton, P., Verhagen, M., Zhou, Z., and Adams, M. (1998). Effect of iron-sulfur cluster environment in modulating the thermodynamic properties and biological function of ferredoxin from *Pyrococcus furiosus*. Biochemistry 37, 7351-7362.

[14] Bröcker, M.J., Wätzlich, D., Uliczka, F., Virus, S., Saggu, M., Lendzian, F., Scheer, H., Rüdiger, W., Moser, J. and Jahn D. (2008). Substrate recognition of nitrogenase-like dark operative protochlorophyllide oxidoreductase from *Prochlorococcus marinus*. J. Biol. Chem. 283, 29873-29881.

[15] Saeki, K., Tokuda, K., Fukuyama, K., Matsubara, H., Nadanami, K., Go, M., and Itoh, S. (1996). Site-specific mutagenesis of *Rhodobacter capsulatus* ferredoxin I, FdxN, that functions in nitrogen fixation. Role of extra residues. J. Biol. Chem. 271, 31399-31406.

[16] Naud, I., Meyer, C., David, L., Breton, J., Gaillard, J., and Jouanneau, Y. (1996). Identification of residues of *Rhodobacter capsulatus* ferredoxin I important for its interaction with nitrogenase. Eur. J. Biochem. 237, 399-405.

[17] Hans, M., Buckel, W. and Bill, E. (2000). The iron-sulfur clusters in 2-hydroxyglutaryl-CoA dehydratase from *Acidaminococcus fermentans*. Biochemical and spectroscopic investigations. Eur J Biochem 267, 7082-93.

[18] Onate, Y.A., Finnegan, M.G., Hales, B.J. and Johnson, M.K. (1993). Variable-temperature magnetic circular-dichroism studies of reduced nitrogenase iron proteins and $[4Fe\text{-}4S]^+$ synthetic analog clusters. Biochim. Biophys. Acta 1164, 113-123.

[19] Hagen, W.R., Eady, R.R., Dunham, W.R. and Haaker, H. (1985). A Novel S = 3/2 EPR Signal associated with native Fe-proteins of nitrogenase. FEBS Lett. 189, 250-254.

[20] Lindahl, P.A., Day, E.P., Kent, T.A., Orme-Johnson, W.H. and Munck, E. (1985). Mössbauer, EPR, and magnetization studies of the *Azotobacter vinelandii* Fe protein. Evidence for a $[4Fe\text{-}4S]^{1+}$ cluster with spin S = 3/2. J Biol Chem 260, 11160-73.

[21] Boll, M., Fuchs, G., Tilley, G., Armstrong, F.A. and Lowe, D.J. (2000). Unusual spectroscopic and electrochemical properties of the 2[4Fe-4S] ferredoxin of *Thauera aromatica*. Biochemistry 39, 4929-38.

[22] Onate, Y.A., Vollmer, S.J., Switzer, R.L. and Johnson, M.K. (1989). Spectroscopic characterization of the iron-sulfur cluster in *Bacillus subtilis* glutamine

phosphoribosylpyrophosphate amidotransferase. J. Biol. Chem. 264, 18386-91.

[23] Jung, Y.S., Bonagura, C.A., Tilley, G.J., Gao-Sheridan, H.S., Armstrong, F.A., Stout, C.D. and Burgess, B.K. (2000). Structure of C42D *Azotobacter vinelandii* FdI. A Cys-X-X-Asp-X-X-Cys motif ligates an air-stable $[4Fe\text{-}4S]^{2+/+}$ cluster. J. Biol. Chem. 275, 36974-83.

[24] Yu, L.A., Vassiliev, I.R., Jung, Y.S., Bryant, D.A. and Golbeck, J.H. (1995). Modified ligands to F_A and F_B in photosystem I. II. Characterization of a mixed-ligand [4Fe-4S] cluster in the C51D mutant of PsaC upon rebinding to P700-F_X cores. J. Biol. Chem. 270, 28118-28125.

[25] Miyamoto, R., Iwaki, M., Mino, H., Harada, J., Itoh, S. and Oh-Oka, H. (2006). ESR signal of the iron-sulfur center F_X and its function in the homodimeric reaction center of *Heliobacterium modesticaldum* Biochemistry 45, 6306-16.

[26] Heinnickel, M., Agalarov, R., Svensen, N., Krebs, C. and Golbeck, J.H. (2006). Identification of F_X in the heliobacterial reaction center as a [4Fe-4S] cluster with an $S = 3/2$ ground spin state. Biochemistry 45, 6756-64.

[27] Vassiliev, I.R., Ronan, M.T., Hauska, G. and Golbeck, J.H. (2000). The bound electron acceptors in green sulfur bacteria: resolution of the g-tensor for the F_X iron-sulfur cluster in *Chlorobium tepidum*. Biophys J 78, 3160-9.

[28] Jagannathan, B. and Golbeck, J.H. (2008). Unifying principles in homodimeric type I photosynthetic reaction centers: properties of PscB and the F_A, F_B and F_X iron-sulfur clusters in green sulfur bacteria. Biochim. Biophys. Acta 1777, 1535-44.

[29] Warden, J.T. and Golbeck, J.H. (1986). Photosystem I charge separation in the absence of centers A and B. II. ESR spectral characterization of center 'X' and correlation with optical signal 'A_2'. Biochim. Biophys. Acta 849, 25-31.

[30] Stephens, P., Jollie, D., and Warshel, A. (1996). Protein control of redox potentials of iron sulfur proteins. Chem. Rev. 96, 2491-2514.

[31] Heyes, D., and Hunter, C. (2005). Making light work of enzyme catalysis: Protochlorophyllide oxidoreductase. Trends Biochem. Sci. 30, 642-649.

[32] Reibothe, C., El Bakkouri, M., Buhr, F., Muraki, N., Nomata, J., Kurisu, G., Fujita, Y., and Reinbothe, S. (2010). Chlorophyll biosynthesis: Spotlight on protochlorophyllide reduction. Trends Plant Sci., 15, 614-624..